

**DEVELOPMENT OF BIODYNAMIC IMAGING FOR PHENOTYPIC
PROFILING OF LIVING TISSUE**

by

Zhen Hua

A Dissertation

Submitted to the Faculty of Purdue University

In Partial Fulfillment of the Requirements for the degree of

Doctor of Philosophy



Department of Physics and Astronomy

West Lafayette, Indiana

December 2022

THE PURDUE UNIVERSITY GRADUATE SCHOOL
STATEMENT OF COMMITTEE APPROVAL

Dr. David Nolte, Chair

Department of Physics and Astronomy

Dr. Kenneth Ritchie

Department of Physics and Astronomy

Dr. Martin Kruczenski

Department of Physics and Astronomy

Dr. Oana Malis

Department of Physics and Astronomy

Approved by:

Dr. Gabor Csathy

Devoted to my family and friends

ACKNOWLEDGMENTS

Many people have assisted directly and indirectly in the completion of this work. I would like to thank my advisor and mentor, Prof. Nolte, for his continual guidance during this research. Our many discussions on topics of physics have been invaluable to me during my graduate education and will continue to have value as I progress to other phases of my life. I also must thank Prof. Turek , Prof. Childress and Prof. Ximenes, who increased my understanding of the biology involved in this work, and without whose continued effort, this research would not have been possible. Thanks go to my graduate committee (Prof. Ritchie, Prof. Kruczenski and Prof. Malis) for their support and patience. Thanks to my collaborators over the years of this research, Drs. Zhe Li, Honggu Choi and Fernanda Cunha. Thanks to my family and friends who have been very supportive and encouraging during my Ph.D. study. Lastly, I must acknowledge the continual support of my eternal partner and friend, Shujin Jiang.

TABLE OF CONTENTS

LIST OF TABLES	8
LIST OF FIGURES	9
ABSTRACT	14
CHAPTER 1. INTRODUCTION TO BIODYNAMIC IMAGING	15
1.1 Theoretical Background on Coherence-domain Digital Holography	15
1.1.1 Free-space propagation.....	15
1.1.2 Phase-Stepping Interferometry	16
1.1.3 Off-axis Holography	17
1.2 Intracellular Dynamics and Living Tissue.....	18
1.3 Fundamentals of Biodynamic Imaging.....	19
1.3.1 Optical Coherence Tomography (OCT)	19
1.3.2 Speckle Phenomenon.....	20
1.3.3 Coherence Gating	20
1.3.4 Dynamic Light Scattering (DLS).....	21
1.3.5 Fourier-domain Digital Holography	22
1.4 Biodynamic Imaging.....	25
1.4.1 Biodynamic Profiling System.....	25
1.4.2 Optical Coherence Imaging	27
1.4.3 Motility Contrast Imaging	28
1.4.4 Tissue Dynamics Spectroscopy	28
1.4.5 Biodynamic Biomarkers	30
1.5 References.....	33
CHAPTER 2. BIODYNAMIC CHEMOSENSITIVITY TESTING IN REVIVED FRESH-FROZEN BIOPSIES.....	38
2.1 Overview of Canine B-Cell Lymphoma project.....	38
2.2 Experimental Set-Up and Procedures	40
2.2.1 Sample Preparation	40
2.2.2 Experiment Set-Up	42
2.3 Fluctuation Spectroscopy and Drug-response Spectrograms	42

2.4	Machine Learning and Data Clustering	45
2.5	Discussion.....	50
2.6	Conclusion	50
2.7	Reference	51
CHAPTER 3. BIODYNAMIC PROFILING OF HUMAN ESOPHAGEAL CANCER HETEROGENEITY		55
3.1	Overview of Human Esophageal Cancer project.....	55
3.2	Methods.....	57
3.2.1	Experiment Set-Up	57
3.2.2	Sample preparation	58
3.2.3	Clinical Trial Patient Enrollment for Esophageal Cancer	58
3.2.4	Spectrogram Heterogeneity	60
3.2.5	Drug-Response Spectrograms	61
3.2.6	Siamese Auto Encoder.....	63
3.3	Results.....	65
3.4	Discussion.....	69
3.5	Reference	70
CHAPTER 4. BIODYNAMIC MONITORING OF BACTERIAL INVASION OF LIVING TISSUE		73
4.1	Introduction.....	73
4.1.1	Introduction to Bacteria	73
4.1.2	Infection Assay of Pathogenic Bacteria within a Cell Line.....	74
4.2	Sample preparation and Experiment Set-Up.....	75
4.2.1	Common-path System	75
4.2.2	Specimen Preparation	78
4.3	BDI Results and Analysis	80
4.3.1	OCI results and data quality control	80
4.3.2	Fingerprints of Processes from Bacterial Invasion of Living Tissue	82
4.3.3	Doppler Spectral Shift (DSS)	85
4.3.4	Doppler Knee Frequency, Mid Frequency Slope Parameter and Nyquist Floor Analysis	87

4.4	Discussion and Conclusion.....	90
4.5	References.....	91
APPENDIX A.	TISSUE DYNAMIC SPECTROSCOPY NORMALIZATION	93
APPENDIX B.	BIODYNAMIC PROFILING OF HUMAN ESOPHAGEAL CANCER HETEROGENEITY USING A DEEP TWIN AUTOENCODER	95
PUBLICATIONS.....		101

LIST OF TABLES

Table 1 List of current using biomarkers	32
Table 2 Explanations of several biomarkers for example.....	33
Table 3 Progression-free survival (PFS) is defined as the length of time during and after the treatment of a disease, such as cancer, that a patient lives with the disease without progression. PFS longer than 180 days is defined as the chemotherapy response sensitive group. From this table, canine patients Kodie, Graciebell, Sinker and Chester are regarded as the drug sensitive group, and canine patients Badger, Scout, Boost are regarded as the drug resistant group.....	41
Table 4 <i>Ex Vivo</i> Treatments.....	59
Table 5 Bacterial strains and corresponding physical characteristics.....	74
Table 6 Patient Treatment [#] and Outcomes*.....	96

LIST OF FIGURES

Figure 1-1 Optical set-up for Fourier-domain digital holography: OP, object plane; FP, Fourier plane; IP, image plane; f, focal length of the lens; ψ_O , object wave at OP; ψ_{OF} , object wave at FP; ψ_R , reference wave.....	17
Figure 1-2 cellular size – speed relation. The speeds of intracellular dynamics ranges across four orders of magnitude from tens of nanometers per second (cell membrane) to tens of microns per second (organelles, vesicles)	19
Figure 1-3 a) time-domain OCT; b) Fourier-domain OCT; c) <i>en face</i> OCT [9]	20
Figure 1-4 Doppler scattering geometry for incident and scattered k-vector, q-vector and particle velocity.[8] Doppler frequency shift is only dependent on the velocity of the moving particle. .	22
Figure 1-5 a) Fourier-domain digital holographic configuration. A beam splitter (BS) splits the light into two coherent beams: the object beam that impinges on the target, and the reference beam that is routed through a series of delay mirrors (M). Light scattered from the target (OP) is projected onto the Fourier plane (FP) by the lens (L) where it is spatially heterodyned with the reference beam, and the CCD records the resulting interference as an intensity hologram. The hologram is numerically Fourier-transformed back into an image (IP) of the target. b) The OCI Fourier frame captures c) a holographic intensity pattern when the optical path length difference between the object and reference beams is within the coherence length of the source. d) The corresponding image and conjugate image are reconstructed from the OCI frame through a fast Fourier transform. e) An image of the target, a tumor spheroid, can be seen	23
Figure 1-6 Fourier-domain Mach-Zehnder configuration for an off-axis digital holography system (BDI setup). The bandwidth of the light source is 50 nm, the wavelength is 840 nm, and the coherence length is 15 μm . With a biopsy plate mounted at the target position, the scattering from the sample serves as the signal while the reflection from the first beam splitter serves as the reference arm. The crossing angle between the reference beam and the signal beam is two degrees and can be changed by tuning the orientation of the final beam splitter or the mirror system. A neutral density (ND) filter is placed on the reference arm to reduce the intensity of the reference. The CCD camera is placed on the focal plane of the third lens.....	26
Figure 1-7 Screenshot of LabView interface in BDI's computer. a) the front panel of a program for 16-sample experiments. b) program for data acquisition.....	26
Figure 1-8 a) A change in MCI of a DLD-1 tumor spheroid after FCCP is added. Baseline (“healthy”) measurements show an overall NSD > 0.8, and this value gradually decreases over time b) Decrease in overall (i.e. sample averaged) NSD of the DLD-1 tumor spheroid after the FCCP drug, compared with control medium. FCCP, a mitochondrial uncoupling drug that disrupts ATP synthesis, slows down the cellular activity in the DLD-1 spheroid [16].	28
Figure 1-9 Spectra and spectrogram for a canine B-cell lymphoma biopsy responding to doxorubicin. a) Spectra of a baseline and drug treated measurement. The knee of the sample has shifted to a higher frequency. b) The spectra over the entire experiment for this biopsy. Drug was	

added between after 4 hours (horizontal line). c) Differential spectrogram of the biopsy, showing strong suppression at low frequency and enhancement at high frequency [8].	30
Figure 1-10 An example of sample baseline and terminal spectra, and the differential spectrogram. a) baseline spectrum and final spectrum after the sample is treated with 10 μM paclitaxel. b) time-lapse differential power spectrogram.....	31
Figure 1-11 The 3x3 masks are the 9 Legendre biomarkers. ALLF0, SDIP0 and CDIP0 are global biomarkers. The rest 6 masks are local biomarkers.....	32
Figure 2-1 Plate layout showing the subset of the 96-well plate used for the 16-plex measurements. Two plates are used per canine patient for a total of 32 wells with a replicate number of 4 or 6 wells per treatment per patient.....	42
Figure 2-2 Negative control (DMSO-based response) spectrograms. DMSO (0.1%) has been applied after 4 hours. (a) spectrograms for fresh biopsy, (b) spectrograms for thawed sample, (c) the difference of spectrogram between thawed samples and fresh biopsies. The replicate numbers of fresh and thawed sample are 55 and 56, respectively.....	43
Figure 2-3 Relative Spectrogram Comparison of Fresh/Thawed and drug-Sensitive/Resistant for the BDI results. Each column stands for a relative spectrogram (negative control subtracted) comparison based on one specific drug response under four different conditions: fresh drug-resistant biopsy, thawed drug-resistant biopsy, fresh drug-sensitive biopsy, thawed drug-sensitive biopsy. X-axis is Frequency, Y-axis is measurement time. Drug was applied after 4 hours. All the drug response spectrograms have already subtracted the corresponding negative control response spectrogram.....	44
Figure 2-4 Relative Spectrograms (negative control subtracted) for drug responses. The relative spectrograms generated by subtracting from the spectrogram of thawed samples subtracting the spectrogram of corresponding fresh biopsies grouped for the same chemotherapy. X-axis is Frequency, Y-axis is measurement time. Drug is applied after 4 hours.....	45
Figure 2-5 Similarity matrix and clustered network for fresh & thawed group. (a), Similarity matrix for fresh group, 1-3 means for fresh resistant dogs, 4 is the averaged fresh resistant group, 5 is the averaged fresh sensitive group, 6-9 means for fresh sensitive dogs. Each color stands for the correlation coefficient of 32 biomarkers between the two corresponding dog samples. The matrix shows a crude block diagonal pattern with two main groups. (b) Similarity network for fresh groups, blue dots are resistant ones, orange dots are sensitive ones. Clique coefficient is defined as the accuracy of matching links. (c) Similarity matrix for thawed group, 1-3 means for thawed resistant dogs, 4 is the averaged thawed resistant group, 5 is the averaged thawed sensitive group, 6-9 means for thawed sensitive dogs. Each color stands for the correlation coefficient across 32 biomarkers between the two corresponding dog samples. The matrix shows a block diagonal pattern with two main groups. (d) Similarity network for thawed groups, blue dots are resistant dogs, and orange dots are sensitive dogs. The clique coefficient is defined as the accuracy of matching links.	47
Figure 2-6 Clustering analysis. (a) Selected biomarkers which are most important features for distinguishing the two different cohorts. (b) Similarity Matrix for all dogs (1-7 represents resistant groups, 8-16 represents the sensitive groups). Each grid stands for the correlation coefficient of 32 biomarkers between the two corresponding dog samples. The matrix shows a weak block diagonal	

pattern with two main groups. (c) Similarity network for all dogs, blue dots are resistant ones, red dots are sensitive ones. Clique coefficient is defined as the accuracy of matching links.....	48
Figure 2-7 Individual spectrograms of DMSO (negative control) response for thawed samples. X-axis is Frequency, Y-axis is measurement time. DMSO has been applied after 4 hours. (a) Difference between spectrogram of dmso response for fresh and thawed resistant group (patient name Badger, Scout, Boost). (b) Difference between spectrogram of dmso response for fresh and thawed sensitive group (patient name Graciebell, Sinker, Kodie, Chester).	49
Figure 2-8 Similarity matrix after freezing trauma compensation. (a) Similarity Matrix for all dogs after compensation (1-7 stands for resistant groups, 8-16 stands for sensitive groups). Each color stands for the correlation coefficient among 32 biomarkers between the two corresponding dog samples. The matrix shows a weak block diagonal pattern with two main groups. (b) Similarity network for all dogs after compensation, blue dots are resistant ones, red dots are sensitive ones. Clique coefficient is defined as the accuracy of match lines.....	49
Figure 3-1 Drug-response spectrograms from a single patient treated with DMSO (0.1%), carboplatin (25 μ M), taxol (10 μ M), 5FU fluorouracil (25 μ M), cisplatin (25 μ M) and the combination therapies of carboplatin and taxol and cisplatin and 5FU. The horizontal axis shows frequencies in the range from 10 mHz to 10 Hz. The vertical axis is the experiment duration. The solid blue line is when the treatments were applied. The axes are the same for all spectrograms. (a) The averaged drug-response spectrograms from Esophageal patient 31. (b) The spectrogram collage from the same patient on a per well basis. The replicate number for each treatment is three or four.....	61
Figure 3-2 Resistant versus sensitive phenotypes. Top rows have average spectrograms of patients with stable disease. Middle rows are for patients with complete response. Bottom rows are the difference of resistant relative to sensitive. a) Spectrogram averages with all well-based phenotypes (1, 2, 3, and 4) included. b) Spectrogram averages with only high-frequency enhanced phenotypes (1 and 4) included.	62
Figure 3-3 The “twin” network for dimensionality reduction consists of a single network that receives two inputs. Data structures are applied in pairs, then the contrastive loss is used to update the parameters. The network in this figure has two layers of fully-connected ReLUs that are fully connected to the output neurons.	64
Figure 3-4 Drug-response biodynamic spectrograms for the esophageal cancer clinical trial. a) Four spectrogram phenotypes from esophageal biopsies. In this nomenclature, phenotype-1 is blue shifted, phenotype-2 is redshifted, phenotype-3 is mid-frequency enhanced, and phenotype-4 is mid-frequency suppressed. b) Similarity matrix of the feature vectors from all wells ordered by phenotype.....	66
Figure 3-5 Classification accuracies for training patients and for all patients as a function of feature combinations used in the Siamese autoencoder. a) All classes. b) Stable disease versus other classes. Latent dimensionality is equal to 3.....	67
Figure 3-6 Neural network low-dimensionality latent space. a) The output states of the Twin neural network. b) Three-dimensional representation of a batch of Patient Charts plot showing strong clustering into 3 classes. c) Network graph generated from the latent-space representation. d)	

One-hold-out patient classification for the 22 training patients plus 6 atypical patients. The four mis-classified patient IDs are shown in red and all were from the atypical patient group.....	68
Figure 4-1 SEM pictures of (a) <i>E. coli</i> [2](b) <i>S. enterica</i> [3]and (c) <i>L. monocytogenes</i> [4]......	74
Figure 4-2 Common-path System. The probe beam illuminates the target at an oblique angle of 34 degrees relative to the backscatter direction. There is a spatial filter with a big aperture and a small aperture in IP2. Digital holograms are captured by the camera in FP2. Direct images are captured in IP and IP2. The reconstruction image is compared with direct images from the image planes.	76
Figure 4-3 (A to D) Growth curves for the three pathogens <i>Salmonella</i> serovar <i>Enteritidis</i> , <i>E. coli</i> O157:H7, and <i>L. monocytogenes</i> (<i>L. mono</i>) mixed at various ratios in SEL: <i>Salmonella</i> CFU/ <i>E. coli</i> CFU/ <i>L. monocytogenes</i> culture ratios, 1:1:1 (A), 10:1,000:1 (B), and 1:10:1,000 (C), and <i>Salmonella</i> monocyto <i>genes</i> culture ratio, 1,000:10 (D) [14].....	79
Figure 4-4 Workflow for specimen preparations. Before applying bacteria, 4 baseline measurements were made over 2 hours. After the baseline measurement, 100 μ l of the diluted bacterial medium was pipetted into the wells. Each well was monitored repeatedly by BDI for more than 22 hours to detect interactions between bacteria and DLD-1 cells. We also grow the treatment culture into a LB agar plate before and after the BDI experiment to confirm the initial and final concentrations of bacteria inside each well. The bacteria inside the culture plate usually become visible after 24 hours (48 hours for <i>L. monocytogenes</i>).....	80
Figure 4-5 OCI experimental collage for bacterial infected DLD-1 cells. These data are collected from well #4 of experiment 22020517 <i>S. enterica</i> infection. There is a significant intensity increase in the late-loop measurements, which indicates the cell infection from bacteria.	81
Figure 4-6 OCI experiment collage for non-bacterial infected DLD-1 cells. These data are collected from well #4 of experiment 22020517 <i>S. enterica</i> infection. There is no significant intensity change detected in the late-loop measurements, which indicates the cell is healthy during the entire monitoring period.....	82
Figure 4-7 BDI fingerprints for <i>E. coli</i> invasion of living tissue. There are seven groups in this series of experiment: negative control group (PBS buffer), <i>E. coli</i> with concentration of 10 CFU/ml, <i>E. coli</i> with concentration of 10^2 CFU/ml, <i>E. coli</i> with concentration of 10^3 CFU/ml, <i>E. coli</i> with concentration of 10^4 CFU/ml, <i>E. coli</i> with concentration of 10^5 CFU/ml, and <i>E. coli</i> with concentration of 10^6 CFU/ml.....	83
Figure 4-8 BDI fingerprints for <i>S. enterica</i> invasion of living tissue. There are four groups in this series of experiment: negative control group (PBS buffer), <i>S. enterica</i> with concentration of 10^3 CFU/ml, <i>S. enterica</i> with concentration of 10^4 CFU/ml, and <i>S. enterica</i> with concentration of 10^5 CFU/ml.	85
Figure 4-9 Doppler Spectral Shift for <i>E. coli</i> (a-c) and <i>S. enterica</i> (d-f) invasion of living tissue at low (0.01Hz), mid (0.1Hz), high frequency(>1Hz).	87
Figure 4-10 Doppler knee frequency shift among a) <i>E. coli</i> invasion, b) <i>S. enterica</i> invasion and c) <i>L. monocytogenes</i> invasion.....	88

Figure 4-11 Doppler midfrequency slope parameter shift among a) *E. coli* invasion, b) *S. enterica* invasion and c) *L. monocytogenes* invasion 89

Figure 4-12 Doppler spectral Nyquist floor shift among a) *E. coli* invasion, b) *S. enterica* invasion and c) *L. monocytogenes* invasion 90

ABSTRACT

Biodynamic imaging (BDI) is a high-content optical imaging technology based on Fourier-domain digital holography and Doppler spectroscopy of intracellular dynamics. There are three main functions of the BDI technique, which are optical coherence imaging (OCI), motility contrast imaging (MCI) and tissue dynamics spectroscopy (TDS). OCI is related to *en face* optical coherence tomography (OCT) using partially coherent speckle generated by broad-area illumination with coherence detection through digital holography. MCI provides noninvasive functional imaging by treating intracellular motility as an endogenous dynamic imaging contrast agent. TDS produces broad-band Doppler fluctuation power spectra that contain the ensemble of all intracellular motions by collecting and extracting depth-resolved quasi-elastic dynamic light scattering from inside multicellular living tissue. This thesis presents the development and applications of BDI systems. Doppler spectral clustering analysis is demonstrated when comparing fresh canine lymphoma biopsies and their corresponding flash-Frozen samples. Doppler spectral phenotyping analysis is used to identify a non-predictive phenotype of TDS that shows a systemic red-shift of frequencies. Doppler spectral shift analysis is used to monitor bacterial infection of living tissue.

CHAPTER 1. INTRODUCTION TO BIODYNAMIC IMAGING

1.1 Theoretical Background on Coherence-domain Digital Holography

Holography is a coherent optical technique that records scattered light and generates holograms. The basic process of holography records the interference fringes between a homogeneous reference wave and a scattered wave from an object [1-7]. The complex pattern of interference fringes is called the hologram. The goal of holography is to record and extract image information, and thus it is primarily an imaging process. Holographic recording can be performed in more than one way: 1) it can be a physical hologram generated by two coherent waves and recorded in a photographic film [8-10], or 2) it can be a digital hologram recorded on a digital CCD or pixel array [6-7,11-15]. To extract quantitative information from a digital hologram, it is necessary to reconstruct an image through numerical algorithms like Fourier Transform or autocorrelation function. The advantage of digital reconstruction is that the three-dimensional information from scattered light can be obtained from a single hologram under appropriate conditions [7,16-18]. The development of CCD chips and digital cameras provided digital recording platforms with low cost and high performance for holographic applications.

1.1.1 Free-space propagation

The electric field $E_s(r)$ at the hologram plane is a function of the field $E_0(r_0)$ of the object after the free-space propagator $H(r, z_d)$,

$$E_s(r) = \int H(r, z_d) E_0(r_0) dr_0 \quad (1.1)$$

The free-space propagator $H(r, z_d)$ can be considered as a Fresnel propagator,

$$H(r) = -i \frac{k}{2\pi z_d} e^{ikz_d} e^{\frac{i-k}{2z_d} r^2} \quad (1.2)$$

or any propagator, such as a lens.

At the hologram plane, the hologram field is the sum of the reference field and the signal field, giving

$$E_H = E_r + E_s \quad (1.3)$$

and the hologram intensity is

$$I_H = |E_r + E_s|^2 = I_r + I_s + E_r E_s^* + E_r^* E_s \quad (1.4)$$

It consists of four terms. The first two terms are the intensity of the reference and the signal. The third and fourth terms are phase conjugate terms. Assuming the reference field is a plane wave or spherical wave, the amplitude and phase of the reference field are considered to be a constant or smoothly varying. Therefore, the conjugate term in equation (1.4) is

$$I_r = E_r^* E_s = E_r^* \int H(r, z_d) E_0(r_0) dr_0 \quad (1.5)$$

The goal of digital holography is executed by extracting of the complex function from the hologram intensity.

1.1.2 Phase-Stepping Interferometry

In phase-stepping interferometry, the constant phase of the reference wave is stepped through discrete values ϕ_n . Therefore, the hologram images can be recorded at each discrete phase value.

The hologram field is

$$E_H = E_r e^{i\phi_n} + E_s \quad (1.6)$$

and the hologram intensity is

$$I_H(\phi_n) = I_r + I_s + E_r E_s^* e^{i\phi_n} + E_r^* E_s e^{-i\phi_n} \quad (1.7)$$

For N discrete phases, the hologram intensity I_{Hs} is extracted as

$$I_{Hs} = \frac{1}{N} \sum e^{i\phi_n} I_H(\phi_n) \quad (1.8)$$

1.1.3 Off-axis Holography

Phase-stepping interferometry requires multiple exposures to extract the hologram intensity I_{Hs} . Off-axis holography is another approach that tilts the axis of the reference wave relative to the optic axis of the signal wave [19,20]. Thus, it creates a spatial phase shift that modulates the reference wave

$$E_H = E_r e^{-ikx \sin \theta} + E_s \quad (1.9)$$

and the hologram intensity is

$$I_H(x, y) = I_r + I_s + E_r E_s^* e^{ikx \sin \theta} + E_r^* E_s e^{-ikx \sin \theta} \quad (1.10)$$

This intensity pattern represents a hologram spatially modulated by a carrier wave.

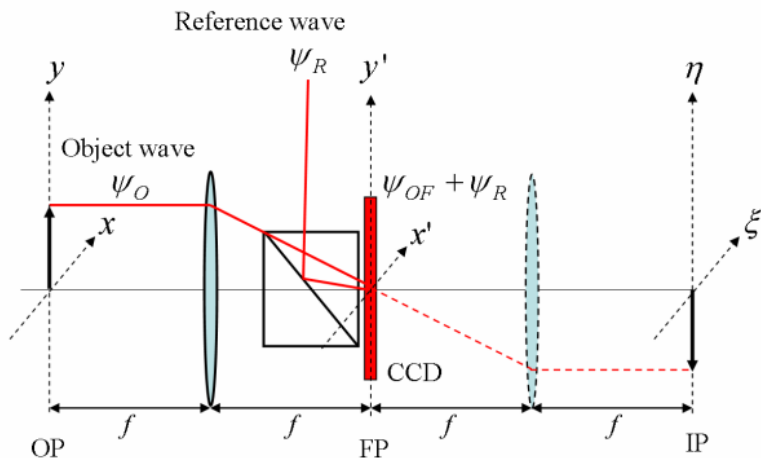


Figure 1-1 Optical set-up for Fourier-domain digital holography: OP, object plane; FP, Fourier plane; IP, image plane; f, focal length of the lens; ψ_O , object wave at OP; ψ_{OF} , object wave at FP; ψ_R , reference wave.

1.2 Intracellular Dynamics and Living Tissue

Imaging of live tissue in a three-dimensional (3D) environment is of critical importance to biophysical science and especially to the study and treatment of cancer. Several 3D tumor models have been developed, including *in vitro* multicellular tumor spheroid models and murine xenografts [43-46]. However, the majority of chemotherapeutic efficacy assays continue to use two-dimensional (2D) culture models. This is because photon diffusion makes direct optical imaging through highly scattering media, such as tumor tissue, difficult and limits the depth resolution of traditional microscopy.

Cells have a typical size of 5-20 μm , which is much larger than the wavelength of near-infrared light. In this regime, ray optics dominates, and cells act as tiny lenses. Stacked into tissue structures, these lenses generate a “showerglass” effect due to optical aberrations that limits resolution as imaging depth increases. Furthermore, the eukaryotic cell is a heterogeneous body containing many different structures with different refractive indices. This causes significant scattering of light as it propagates through tissue.

Eukaryotic cell structure can be separated into different regions. Outside the cell is the extracellular matrix, a region composed of collagen proteins and other molecules used to organize cells into tissue. The cell membrane surrounds the interior of the cell. It is transfixed by different components through which the cell senses changes in the extracellular matrix, communicates with other cells via cell-cell contacts, and takes in nutrients and expels waste. The cytoskeleton, made of microtubules, actin filaments, and stress fibers, is a flexible structure with high tensile strength that gives the cell dynamic rigidity. The cytoplasm fills the interstices of the cytoskeleton and is made up of cellular organelles, the largest of which, the nucleus, exhibits both geometric optic and Mie scattering behaviors [19]. Other organelles important to the study of tissue imaging are mitochondria (typical size: 200 nm to 5 μm), endosomes and exosomes. For these smaller organelles, scattering dominates optical interaction.

Cells and organelles are in constant motion. Mitosis and other processes change cell shape and cause undulations in the cell membrane. The common characteristic frequency of these undulations is in the range of 0.01 Hz to 0.1 Hz [20, 21]. Cytoskeletal components are in dynamic equilibrium, constantly being built and dismantled. Organelles driven by molecular motors travel at speeds in the range of several microns per second [22-25]. The various cellular components

create dynamically shifting scattering interfaces. The rule of thumb is that for wavelength $\lambda = 840$ nm, motion at 1 $\mu\text{m/s}$ corresponds to a Doppler frequency shift of 3 Hz.

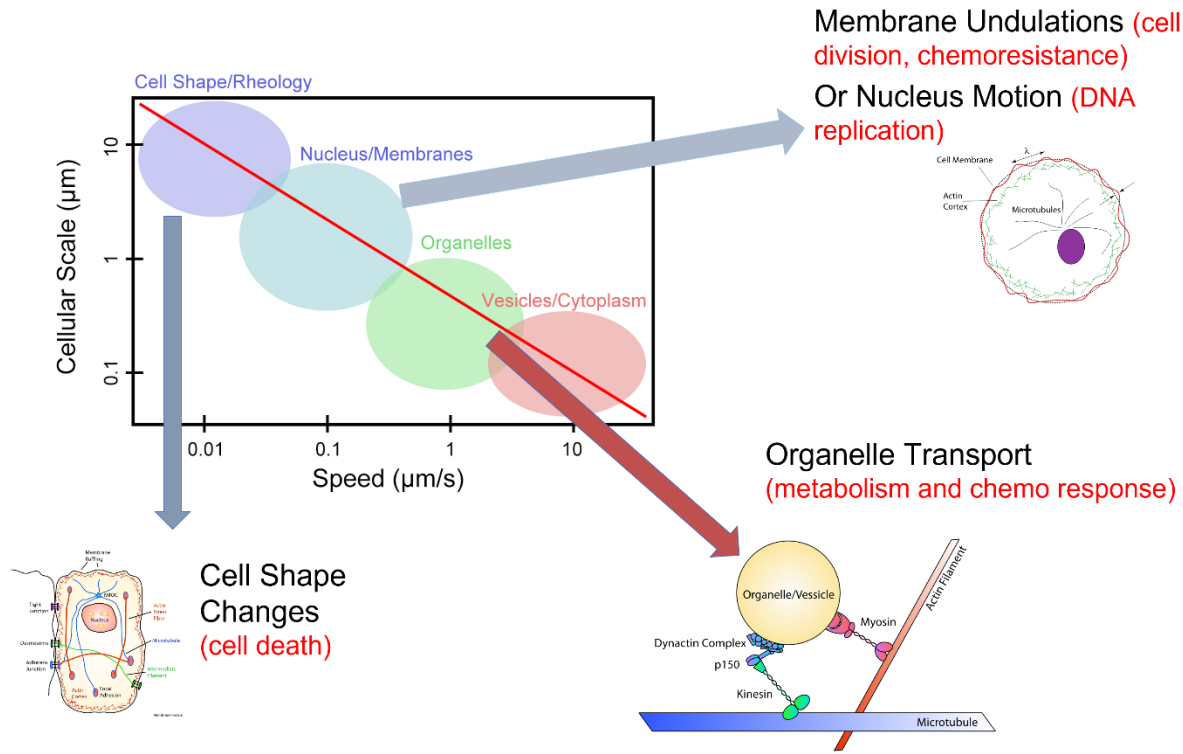


Figure 1-2 cellular size – speed relation. The speeds of intracellular dynamics ranges across four orders of magnitude from tens of nanometers per second (cell membrane) to tens of microns per second (organelles, vesicles).

1.3 Fundamentals of Biodynamic Imaging

1.3.1 Optical Coherence Tomography (OCT)

Tomographic techniques generate slice images of three-dimensional objects. Optical Coherence Tomography uses rapid point-by-point scanning detection for signal demodulation and computed reconstruction. Since the development of OCT in 1990s, it has found wide applications in medicine, including ophthalmology, dermatology and dentistry etc. OCT has the advantage of providing non-invasive diagnostic images, having high depth and transverse resolution. Figure 1-3 describes three common types of OCT: a) time-domain OCT, b) Fourier-domain OCT and c) en face OCT [9]. Our optical coherence imaging technique is related to *en face* optical coherence

tomography using partially coherent speckle generated by broad-area illumination with coherence detection through digital holography.

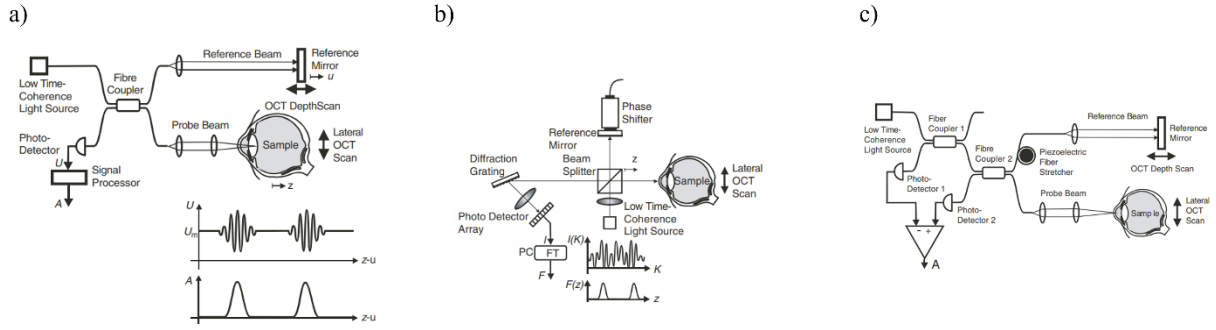


Figure 1-3 a) time-domain OCT; b) Fourier-domain OCT; c) *en face* OCT [9]

1.3.2 Speckle Phenomenon

Speckle is a result of spatial coherence, when waves with random amplitudes and phases are added together to create a randomly varying intensity pattern. The creation of speckle is a random-walk process on the phase plane. Speckle degrades image quality, and various methods have been proposed to reduce speckles [1-3], while in other applications, autocorrelation information can be extracted from speckle and used to reconstruct object information [4, 5]. Speckle size is given by

$$a_{sp} = \frac{\lambda f}{D} \quad (1.11)$$

where λ is the wavelength of the light, f the distance of free space propagation and D is the smaller of either the aperture size of the optics or the object size [6].

1.3.3 Coherence Gating

Diffusing wave spectroscopy and diffuse correlation spectroscopy extend the single-scattering domain to the multiple-scattering domain [46]. Coherence-gating of dynamic light scattering stands between single and multiple scattering [27, 28]. With the help of a low-coherence

light source, a coherence gate can spatially localize the scattered light to select scattering from a specified depth of the optical dense scattering volume [29, 30]. The light source used in coherence gating is required to have good spatial coherence but low temporal coherence.

The coherence length of a Gaussian light source is described by [26]

$$L = \frac{2Ln2}{\pi n} \frac{\lambda^2}{\Delta\lambda} \quad (1.12)$$

where λ is the central wavelength of the source, $\Delta\lambda$ is the FWHM bandwidth of the source, and n is the refractive index of the medium. A desired coherence length can be achieved by selecting proper λ and $\Delta\lambda$ values.

1.3.4 Dynamic Light Scattering (DLS)

Dynamic light scattering (DLS) is caused by motion in the scattering target [21-23]. The motions in the target produce time-varying changes in the phase of the scattered wave. There might be various motions in the target, such as drift, random walk or flights, and each component gives a phase shift causing the time-varying interferences that lead to intensity fluctuations. The light-scattering configuration for dynamic light scattering from a moving particle is shown in Figure 1-1 [8]. The incident light has an initial k-vector k_1 , that is scattered by a small particle into a final k-vector k_2 . The momentum transfer in the scattering process is $q = k_2 - k_1$, and the doppler frequency shift is given by q times v . Doppler frequency shift is

$$\Delta f_{Doppler} = \vec{q} \cdot \vec{v} = \frac{4\pi n}{\lambda} v \sin\left(\frac{\theta}{2}\right) \quad (1.13)$$

where θ is the scattering angle, n is the refractive index of the dynamic medium. for forward scattering, θ is 0, doppler frequency shift is identically 0. For backward scattering, the momentum transfer will reach to its maximum value. And our Doppler frequency shift depends only on the particle velocity.

Doppler Scattering Geometry

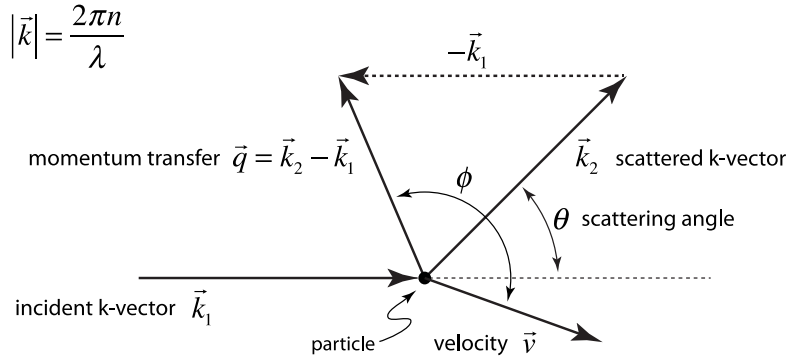


Figure 1-4 Doppler scattering geometry for incident and scattered k-vector, q-vector and particle velocity.[8]
Doppler frequency shift is only dependent on the velocity of the moving particle.

1.3.5 Fourier-domain Digital Holography

At the core of OCI is Fourier-domain digital holography. The theory is explained in greater detail in [7, 54]. In brief, consider the Mach-Zehnder interferometer shown in Figure 1-5 a).

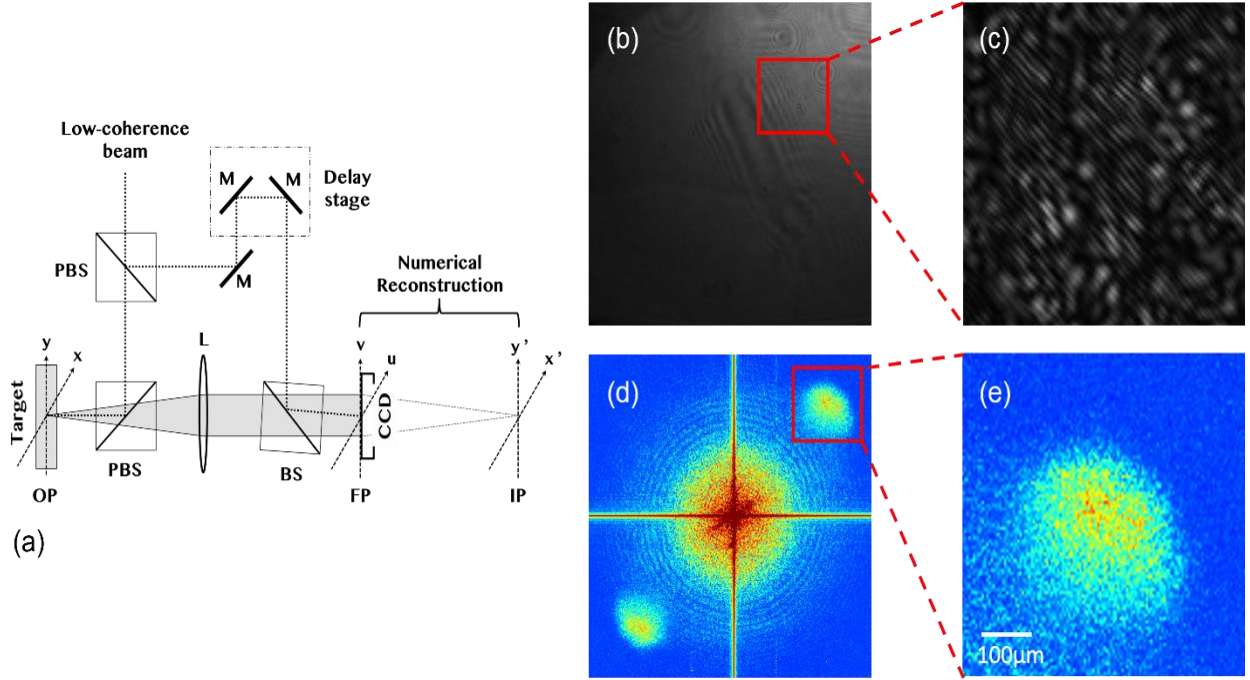


Figure 1-5 a) Fourier-domain digital holographic configuration. A beam splitter (BS) splits the light into two coherent beams: the object beam that impinges on the target, and the reference beam that is routed through a series of delay mirrors (M). Light scattered from the target (OP) is projected onto the Fourier plane (FP) by the lens (L) where it is spatially heterodyned with the reference beam, and the CCD records the resulting interference as an intensity hologram. The hologram is numerically Fourier-transformed back into an image (IP) of the target. b) The OCI Fourier frame captures c) a holographic intensity pattern when the optical path length difference between the object and reference beams is within the coherence length of the source. d) The corresponding image and conjugate image are reconstructed from the OCI frame through a fast Fourier transform. e) An image of the target, a tumor spheroid, can be seen

A beam splitter splits the coherent light source into two waves: a reference plane wave and an object wave. The object wave $E_o(x, y)$ scatters off a target and is Fourier-transformed by an ideal lens of focal length f onto the plane of the CCD camera. The object wave at the plane of the detector is given by

$$E_{od}(u, v) = \frac{i}{\lambda f} \exp\left(-\frac{i4\pi f}{\lambda}\right) \int_{-\infty}^{\infty} \int_{-\infty}^{\infty} E_o(x, y) \exp\left(\frac{i2\pi}{\lambda f} (xu + yv)\right) dx dy \quad 1.14$$

where λ is the wavelength of the source. The reference wave travels through the delay path and is directed onto the detector. The reference plane-wave is given by

$$E_{rd} = E_r \exp(i2\pi(v_x x + v_y y)) \quad 1.15$$

where ν_x and ν_y are the spatial wavenumbers. The reference wave in OCI replaces the need for a phase modulator in conventional OCT, and an off-axis configuration provides a spatially modulated carrier wave, which allows for full-frame imaging of the hologram. The wave at the detector is a coherent sum of the object and reference waves. The intensity pattern recorded by the detector is

$$I_d(u, v) = |(E_{od} + E_{rd})(E_{od}^* + E_{rd}^*)| = |E_{od}|^2 + |E_{rd}|^2 + E_{rd}^*E_{od} + E_{rd}E_{od}^* \quad 1.16$$

The first two terms of Eq. (1.16) are the respective intensities of the object and reference beams at the detector. The last two terms are Fourier- and conjugate Fourier-transforms of the image. After capturing the intensity pattern using a digital camera, a computer performs numerical reconstruction of the images using a fast Fourier transform (FFT). The third and fourth terms can be calculated using Eq. (1.14) and Eq. (1.15), and are given by

$$FT(E_{rd}^*E_{od}) = i\lambda f E_r \exp\left(-\frac{i4\pi f}{\lambda}\right) E_o(-\lambda f \nu_u + \lambda f \nu_x, -\lambda f \nu_v + \lambda f \nu_y) \quad 1.17$$

and

$$FT(E_{rd}E_{od}^*) = -i\lambda f E_r \exp\left(\frac{i4\pi f}{\lambda}\right) E_o^*(\lambda f \nu_u + \lambda f \nu_x, \lambda f \nu_v + \lambda f \nu_y). \quad 1.18$$

The image is located at $(\lambda f \nu_x, \lambda f \nu_y)$ and the conjugate image is located at $(-\lambda f \nu_x, -\lambda f \nu_y)$, and these are separated from the zero-order image at $(0,0)$. Figure 1-5 b-e) shows an example of recorded Fourier-domain hologram and the resulting reconstructed image.

For a CCD camera with pixel size $\Delta u (= \Delta v)$ and a chip size of N by N pixels, the resulting reconstructed image has N by N pixels of size

$$\Delta x' = \Delta y' = \frac{\lambda f}{L} \quad 1.19$$

where $L (= N\Delta u)$ is the width of the CCD chip. Fourier detection is less sensitive to debris in the light path than image detection, and digital processing improves image contrast and noise

reduction capabilities. Holographic image capture also provides depth resolution when a low-coherence illumination source is used.

1.4 Biodynamic Imaging

1.4.1 Biodynamic Profiling System

A schematic of the biodynamic imaging system is shown in Figure 1-6 in a Mach-Zehnder configuration for an off-axis digital holography system. The bandwidth of the light source is 50 nm, the wavelength is 840 nm, and the coherence length is 15 μm . With a biopsy plate mounted at the target position, the scattering from the sample serves as the signal while the reflection from the first beam splitter serves as the reference arm. The crossing angle between the reference beam and the signal beam is two degrees and can be changed by tuning the orientation of the final beam splitter or the mirror system. A neutral density (ND) filter is placed on the reference arm to reduce the intensity of the reference. The CCD camera is placed on the focal plane of the third lens.

Figure 1-6 shows a diagram of the current OCI system. A neutral density filter (ND) attenuates the light from the super-luminescent diode (SLD). The waveplate ($\lambda/2$) adjusts the polarization of the beam before it is split by a polarizing beam splitter (PBS) into object and reference beams to maximize the intensity of the object beam. The object beam is focused by lens L1 onto the target, and the scattered light is collected and projected onto an image plane (IP) by lenses L2 ($f = 15 \text{ cm}$) and L3 ($f = 15 \text{ cm}$). The projected image plane is Fourier-transformed by lens L4 ($f = 5 \text{ cm}$) onto the second Fourier-plane (FP2) at the camera (CCD) with a 1/3 magnification. The reference beam passes through the delay stage (dotted box) and is attenuated by another ND to match the intensity of the object beam at the CCD. The reference beam is directed onto the CCD by means of mirrors (M). Lenses L5 and L6 are used to shape the reference beam to match the beam profile of the scattered object beam at the CCD. Interference patterns are recorded and digitally Fourier-transformed back to the image plane to generate OCI images of the target. The optical delay stage can be adjusted to probe different depths within the target.

Short coherence light at 847.2 nm wavelength with 50 nm FWHM bandwidth is supplied by a 20.5 mW Superlum Broadlighters Fiber Lightsource (model: S-840-B-I-20 SM). This gives a depth resolution of 6.3 μm (single-scattering). The CCD camera is a Basler camera (Basler acA1920-155um) with a bit depth of 14 bits. Recorded images are 800 by 800 pixels with a square

pixel of size of $8 \mu\text{m}$. This results in a minimum practical fringe spacing of $24 \mu\text{m}$ and a minimum speckle size of $72 \mu\text{m}$. Capture is triggered externally through a function generator controlled by a custom-developed LabVIEW VI (National Instruments) that also controls the motion of the 2-axis translation stage and the reference beam delay stage. Camera frames are recorded using the Basler. Camera coordinates and the zero-path matched position of the reference beam delay stage are recorded for each tumor [61].

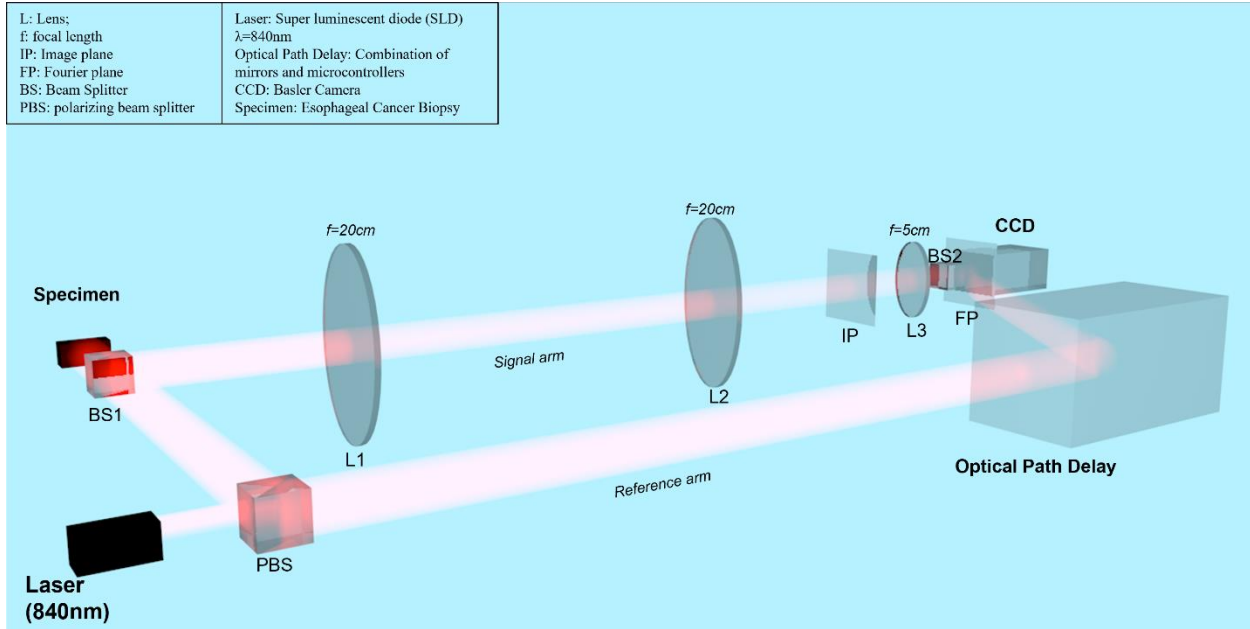


Figure 1-6 Fourier-domain Mach-Zehnder configuration for an off-axis digital holography system (BDI setup). The bandwidth of the light source is 50 nm, the wavelength is 840 nm, and the coherence length is 15 μm . With a biopsy plate mounted at the target position, the scattering from the sample serves as the signal while the reflection from the first beam splitter serves as the reference arm. The crossing angle between the reference beam and the signal beam is two degrees and can be changed by tuning the orientation of the final beam splitter or the mirror system. A neutral density (ND) filter is placed on the reference arm to reduce the intensity of the reference. The CCD camera is placed on the focal plane of the third lens.

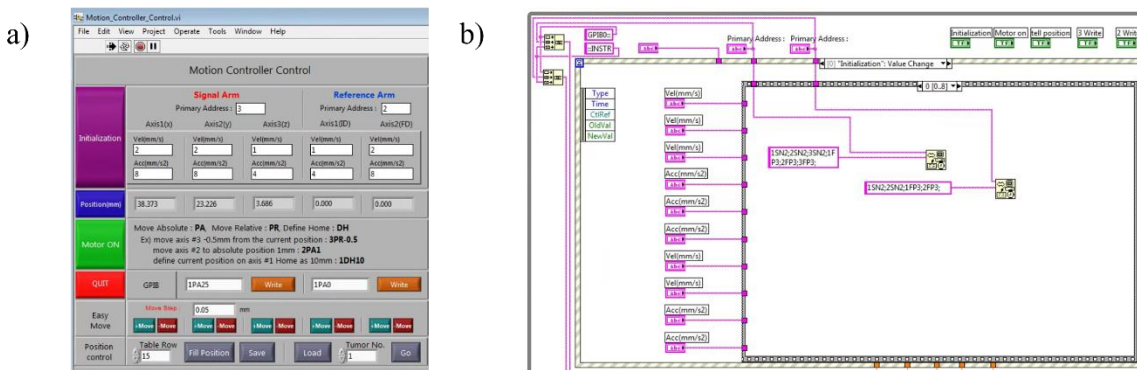


Figure 1-7 Screenshot of LabView interface in BDI's computer. a) the front panel of a program for 16-sample experiments. b) program for data acquisition.

1.4.2 Optical Coherence Imaging

Tomographic techniques have successfully imaged through deep tissue and have found wide clinical and experimental applications. Ultrasound [32], X-ray computed tomography (CT) [33], and magnetic resonance imaging (MRI) [34] are standard imaging modalities found in hospitals all over the world. In more recent years, confocal microscopy [35-37], photoacoustic tomography (PAT) [38-43], and optical coherence tomography (OCT) [8, 10, 11] have achieved smaller resolutions and are growing in clinical use [44-47].

OCT is based on low-coherence reflectometry [48], an optical ranging technique that measures reflectance as a function of depth. OCT uses heterodyne detection to obtain a one-dimensional A-scan of the reflectance. When combined with a second, transverse OCT scan, a two-dimensional B-scan image is generated. The joint system rasters across the target to construct the full 3D image. Depth resolution is limited by the coherence-length of the source independent of the numerical aperture of the imaging system, which allows OCT systems to use very small optics, such as those in an endoscope. OCT has gained wide acceptance since it was first reported in 1991 [8]. It has a penetration depth of about 1 mm in turbid media and a spatial resolution near the diffraction limit for shallow depths in translucent media.

In 1996, Dr. David Nolte's group, in collaboration with Dr. Paul French of Imperial College, London, invented holographic optical coherence imaging (OCI) [49] as a full-frame imaging version of optical coherence tomography (OCT) for probing tissue up to a millimeter in depth. In OCI, positioning the reference off-axis relative to the optical axis of the scattered photons creates a spatially modulated intensity profile. The off-axis orientation allows OCI to record the full image frame in a single capture. OCI was first performed using photorefractive quantum well (PRQW) devices to image live rat osteogenic tumor spheroids [50, 51]. Dr. Kwan Jeong updated the OCI system by moving the PRQW device from image plane to Fourier plane and, later, by replacing the PRQW device with a digital CCD camera [52-54]. Current OCI uses low-coherence [55-58] digital holography [59] to reduce background and improve sensitivity. It achieves high frame rates (25 frames per second) while maintaining resolution and has proven to be a useful tool for studying tissue-level biophysics.

1.4.3 Motility Contrast Imaging

Motility contrast imaging creates a map of the normalized standard deviation (NSD) for each pixel.

NSD is defined as $\frac{\Delta I}{\langle I \rangle}$ for each pixel, where ΔI is the standard deviation and $\langle I \rangle$ is the averaged intensity over time. Motility contrast imaging (MCI) uses speckle intensity fluctuations as a form of label-free image contrast to create a false-color image of the sample motility. Sample motility is influenced by all intracellular motions and is an indication of cell health and cellular action [16-17].

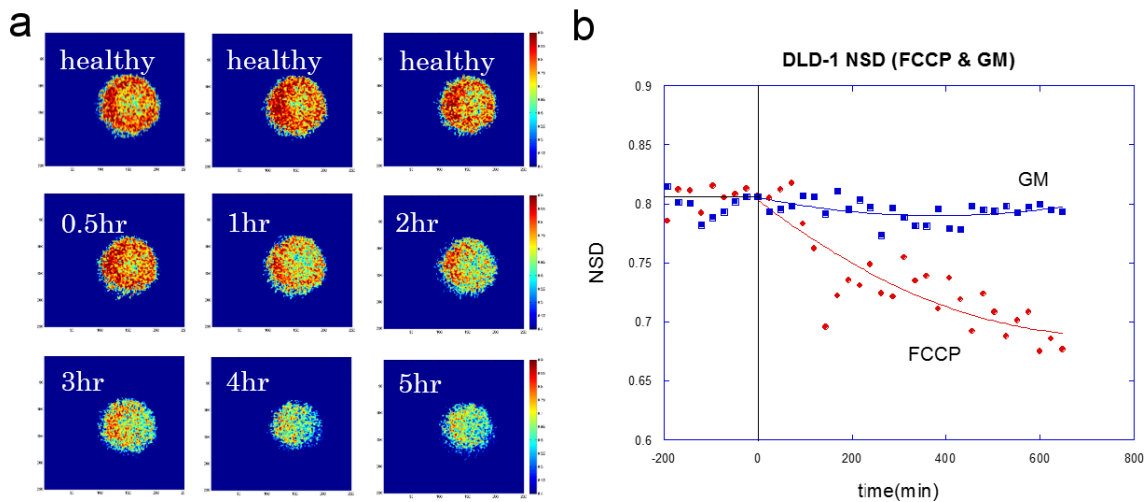


Figure 1-8 a) A change in MCI of a DLD-1 tumor spheroid after FCCP is added. Baseline (“healthy”) measurements show an overall NSD > 0.8, and this value gradually decreases over time b) Decrease in overall (i.e. sample averaged) NSD of the DLD-1 tumor spheroid after the FCCP drug, compared with control medium. FCCP, a mitochondrial uncoupling drug that disrupts ATP synthesis, slows down the cellular activity in the DLD-1 spheroid [16].

1.4.4 Tissue Dynamics Spectroscopy

A sequence of OCI frames is captured, representing one observational run of the living target. By capturing successive sequences over minutes to hours, changes in the time-dependent behavior of the target are detected. For a single OCI sequence, the temporal normalized standard deviation (NSD) of the intensity I is defined at each pixel (x, y) as

$$NSD(x, y) = \frac{\sigma_I(x, y)}{\langle I(x, y) \rangle} = \frac{\sqrt{[\langle I^2 \rangle - \langle I \rangle^2]}}{\langle I \rangle} \quad (1.20)$$

Different biological processes happen at different characteristic speeds. All these processes result in local fluctuations in the index of refraction and cause dynamic changes in the scattered speckle. The autocorrelation of the intensity I of a pixel is given by

$$A_I(\tau) = \langle I(0) I(\tau) \rangle = \langle I \rangle^2 + [\langle I^2 \rangle - \langle I \rangle^2] \exp\left\{-\frac{\tau}{\tau_c}\right\} \quad (1.21)$$

where τ_c is the correlation time of the process. For diffusion and backscatter,

$$1/\tau_c = q^2 D \quad (1.22)$$

where D is the diffusion coefficient. The autocorrelation can be written as

$$A_I(\tau) = 1 + (NSD)^2 \exp\left\{-\frac{\tau}{\tau_c}\right\} \quad (1.23)$$

The Fourier transform is a Lorentzian

$$S(\omega) = \frac{(NSD)^2 \tau_c}{(\omega \tau_c)^2 + 1} \quad (1.24)$$

In log-log, $S(\omega)$ has a distinct shape and exhibits a knee frequency at

$$\omega_c = \frac{1}{\tau_c} = q^2 D \quad (1.25)$$

while the observed process may not be strictly diffusive, the power spectrum can be approximated as

$$S(\omega) = \frac{(NSD)^2 / \omega_c}{(\omega / \omega_c)^s + 1} \quad (1.26)$$

where s is a slope parameter. The central data format of biodynamic profiling of intracellular dynamics inside living tissue is the drug-response spectrogram. It is defined as

$$D(\omega, t; r) = \log S(\omega, t; r) - \log S_0(\omega, t_0; r) \quad (1.27)$$

where $S(\omega, t; r)$ is the spectral power density at time t across the frequency range ω for the voxel located at $r(x, y, z)$. The spectrogram is referenced to the baseline at time t_0 prior to the application of the drug. Therefore, the drug-response spectrogram is a relative time-frequency representation of the changes in internal dynamics, captured through Doppler light scattering. Spectrograms are typically taken from a fixed depth z (usually near the midsection of the biopsy) and averaged over (x, y) to yield an average spectrogram for the sample.

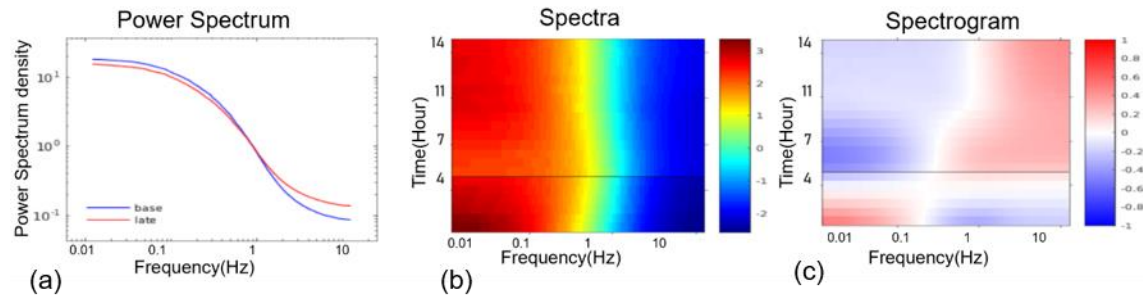


Figure 1-9 Spectra and spectrogram for a canine B-cell lymphoma biopsy responding to doxorubicin. a) Spectra of a baseline and drug treated measurement. The knee of the sample has shifted to a higher frequency. b) The spectra over the entire experiment for this biopsy. Drug was added between after 4 hours (horizontal line). c) Differential spectrogram of the biopsy, showing strong suppression at low frequency and enhancement at high frequency [8].

1.4.5 Biodynamic Biomarkers

To convert OCI, MCI and TDS data of a biological sample generated from a biodynamic imaging experiment to a condensed data format that gives characteristic features of sample condition or responses, several types of biomarkers are used. The current format contains 40 biomarkers, 4 are from OCI, 2 are from MCI, 33 are related to TDS, and the last one is data quality, which is an empirical evaluation of sample and data quality based on the previous 3 groups of biomarkers. The biomarkers can also be categorized into 4 groups:

- Preconditions, i.e. biomarkers that characterize “basic sample status” in the baseline measurement, including backscatter brightness (BB), overall NSD and knee frequency and Nyquist floor of the spectrum
- Change of precondition biomarkers
- Legendre polynomials extracted from spectroscopic response (Figure 1-11)
- Data quality

Precondition biomarkers indicate the sample condition before any perturbation is applied. Such biomarkers include intensity biomarker backscatter brightness (“BSB”), general motility biomarker normalized standard deviation (“NSD”), image pixel count (“NCNT”), and spectroscopy biomarkers like knee frequency (“KNEE”), dynamic range (“DR”), Nyquist floor (“NY”), mid-frequency slope (“S”) and half-width at half maximum (“HW”). On a pixel basis, BSB is the average intensity over 500 frames, and NSD is defined as $\Delta I / \langle I \rangle$, i.e., the standard deviation for the pixel divided by the average intensity or BSB. These biomarkers are usually averaged over an entire sample to denote the general brightness and motility of the sample. The changes in these precondition values form another set of biomarkers, and they are related to variation in Doppler frequency shift and persistence time caused by drug effects.

A Doppler fluctuation spectrum is shown in Figure 1-10. Spectrum-related precondition biomarkers like knee frequency, mid-frequency slope and dynamic range are from curve fitting of a Lorentzian function.

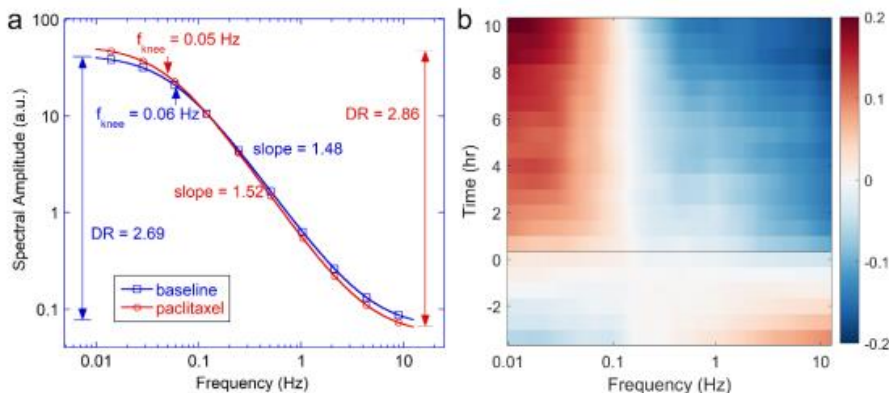


Figure 1-10 An example of sample baseline and terminal spectra, and the differential spectrogram. a) baseline spectrum and final spectrum after the sample is treated with $10 \mu\text{M}$ paclitaxel. b) time-lapse differential power spectrogram.

A vector of 40 numerical biomarker (Table 1) values allows a comprehensive overview of sample conditions and responses and is easy and convenient to use when studying sample heterogeneity and drug profiling. For example, SDIP is a red or blue shift, CDIP is a central frequency enhancement or suppression, etc. Table 2 gives a detailed description of several key biomarkers.

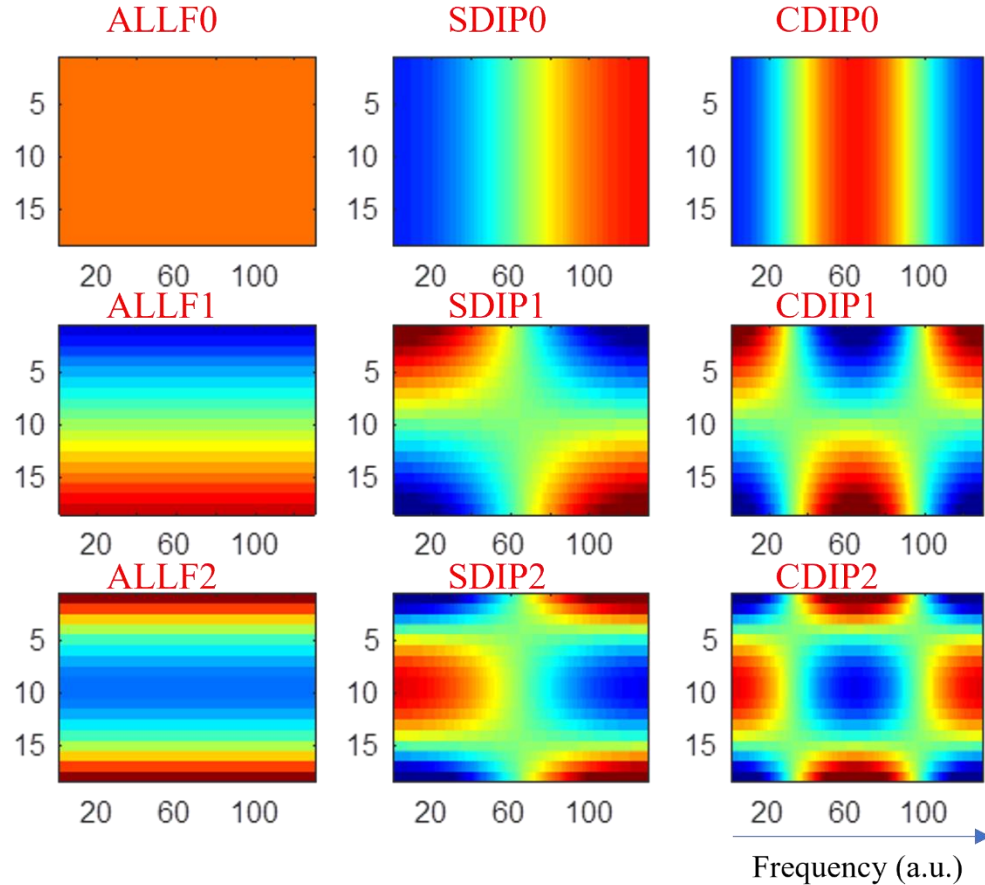


Figure 1-11 The 3x3 masks are the 9 Legendre biomarkers. ALLF0, SDIP0 and CDIP0 are global biomarkers. The rest 6 masks are local biomarkers.

Table 1 List of current using biomarkers

BIOMARKERS						
ALLF0	SDIP0	CDIP0	NSD	BSB	NCNT	DR
ALLF1	SDIP1	CDIP1	DNSD	DBSB	DNCNT	DDR
ALLF2	SDIP2	CDIP2	NY	KNEE	HW	S
LOF0	MID0	HI0	DNY	DKNEE	DHW	DS
LOF1	MID1	HI1	SF	BS0	BS2	
LOF2	MID2	HI2	DSF	BS1	DQ	

Table 2 Explanations of several biomarkers for example.

Biomarker	Type	description
BB	BDI	Backscatter brightness
Floor		Nyquist Floor
NSD		Normalized standard deviation
Δ NSD		Change in NSD
Δ lowF		Change in low frequencies
Δ midF		Change in mid frequencies
Δ allF		Overall change in frequencies

1.5 References

- [1] Y. Zhao, K. K. Chu, W. J. Eldridge, E. T. Jelly, M. Crose, and A. Wax, "Real-time speckle reduction in optical coherence tomography using the dual window method," *Biomedical Optics Express*, vol. 9, p. 616, 2018.
- [2] M. Szkulmowski, I. Gorczynska, D. Szlag, M. Sylwestrzak, A. Kowalczyk, and M. Wojtkowski, "Efficient reduction of speckle noise in Optical Coherence Tomography," *Optics Express*, vol. 20, pp. 1337-1359, 2012/01/16 2012.
- [3] E. Götzinger, M. Pircher, B. Baumann, T. Schmoll, H. Sattmann, R. A. Leitgeb, *et al.*, "Speckle noise reduction in high speed polarization sensitive spectral domain optical coherence tomography," *Optics Express*, vol. 19, pp. 14568-14584, 2011/07/18 2011.
- [4] A. S. Somkuwar, B. Das, R. V. Vinu, Y. Park, and R. K. Singh, "Holographic imaging through a scattering layer using speckle interferometry," *J Opt Soc Am A Opt Image Sci Vis*, vol. 34, pp. 1392-1399, Aug 1 2017.
- [5] O. Katz, P. Heidmann, M. Fink, and S. Gigan, "Non-invasive single-shot imaging through scattering layers and around corners via speckle correlations," *Nature Photonics*, vol. 8, pp. 784-790, 2014.
- [6] J. W. Goodman, *Speckle Phenomena in Optics*, 2006.

- [7] A. Koyama et al. "Spectroscopic analysis in molecular simulations with discretized Wiener-Khinchin theorem for Fourier-Laplace transformation", *Physical Review E*(2020).
- [8] Z.Li et al. "Doppler fluctuation spectroscopy of intracellular dynamics in living tissue", *JOSA A*, 2019.
- [9] A. F. Fercher, W. Drexler, C. K. Hitzenberger, and T. Lasser, "Optical coherence tomography - principles and applications," *Reports on Progress in Physics*, vol. 66, p. 239, 2003.
- [10] J. W. Goodman, *Introduction to Fourier Optics*, 2 ed. New York: MaGraw-Hill, 1996.
- [11] D. Merrill, R. An, H. Sun, B. Yakubov, D. Matei, J. Turek, *et al.*, "Intracellular Doppler Signatures of Platinum Sensitivity Captured by Biodynamic Profiling in Ovarian Xenografts," *Sci Rep*, vol. 6, p. 18821, 2016.
- [12] D. D. Nolte, R. An, J. Turek, and K. Jeong, "Holographic tissue dynamics spectroscopy," *Journal of Biomedical Optics*, vol. 16, pp. 087004-13, Aug 2011.
- [13] K. Jeong, J. J. Turek, and D. D. Nolte, "Speckle fluctuation spectroscopy of intracellular motion in living tissue using coherence-domain digital holography," *Journal of Biomedical Optics*, vol. 15, p. 030514, May-Jun 2010.
- [14] K. Jeong, J. J. Turek, and D. D. Nolte, "Imaging Motility Contrast in Digital Holography of Tissue Response to Cytoskeletal Anti-cancer Drugs," *Optics Express*, vol. **15**, pp. 14057-14064, 2007.
- [15] K. Jeong, "Holographic Optical Coherence Imaging of Living Tissue," Doctor of Philosophy, Purdue University, West Lafayette, IN, USA, 2007.
- [16] S. Hao, "Dynamic Holography in Semiconductors and Biomedical Optics," Doctor of Philosophy, Purdue University, West Lafayette, IN, USA, 2016.
- [17] D. D. Nolte, R. An, J. Turek, and K. Jeong, "Tissue dynamics spectroscopy for phenotypic profiling of drug effects in three-dimensional culture," *Biomedical Optics Express*, vol. 3, pp. 2825-2841, Nov 2012.

- [18] Gabor, Dennis (1949). "Microscopy by reconstructed wavefronts". *Proceedings of the Royal Society. London.* **197** (1051): 454–487.
- [19] Upatniek J & Leonard C., (1969), "Diffraction efficiency of bleached photographically recorded interference patterns", *Applied Optics*, 8, p85-89
- [20] Graube A, (1974), "Advances in bleaching methods for photographically recorded holograms", *Applied Optics*, 13, p2942-6
- [21] N. J. Phillips and D. Porter, (1976), "An advance in the processing of holograms," *Journal of Physics E: Scientific Instruments* p. 631
- [22] Gabor, Dennis (1948). "A new microscopic principle". *Nature*. **161**: 777–8.
- [23] K. Jeong, J. J. Turek and D. D. Nolte, Speckle fluctuation spectroscopy of intracellular motion in living tissue using coherence-domain digital holography, *J. Biomed. Opt.* **15**, 030514 (2010)
- [24] K. Jeong, J. J. Turek and D. D. Nolte, Fourier-Domain Digital Holographic Optical Coherence Imaging of Living Tissue, *Appl. Opt.* **46** , 4999-5008 (2007)
- [25] Benton S.A, (1977), "White light transmission/reflection holography" in *Applications of Holography and Optical Data Processing*, ed. E. Marom et al., ps 401-9, Pergamon Press, Oxford
- [26] Jeong, T. H. 1970, "Holograms," in *Physics Demonstration Experiments*, ed. H. F. Meiners (New York: Ronald Press), vol. 2, chapter 37.
- [27] Beesley, M. J., 1971. Lasers and their Applications, (London: Taylor and Francis), chapter 12.
- [28] Leith, E. N.; Upatnieks, J. (1962). "Reconstructed wavefronts and communication theory". *JOSA*. **52** (10): 1123–1128
- [29] Yamaguchi, I.; Zhang, T. "Phase-shifting digital holography". *Opt. Lett.* **22**: 1268–1270
- [30] Atlan, M.; Gross, M.; Forget, B.; Vitalis, T.; Rancillac, A.; Dunn, A. "Frequency-domain wide-field laser Doppler in vivo imaging". *Opt. Lett.* **31**: 2762–2764

- [31] Paturzo, M.; Memmolo, P.; Tulino, A.; Finizio, A.; Ferraro, P. (2009). "Investigation of angular multiplexing and de-multiplexing of digital holograms recorded in microscope configuration". *Opt. Express.* **17** (11): 8709–8718
- [32] P. Yu, M. Mustata, L. Peng, J. J. Turek, M. R. Melloch, P. M. W. French and D. D. Nolte, Holographic Optical Coherence Imaging of Rat Osteogenic Sarcoma Tumor Spheroids, *Applied Optics*, v 43, n 25, p 4862-4873 (2004)
- [33] P.W.M. Tsang; K. Cheung; T. Kim; Y. Kim; T. Poon (2011). "Fast reconstruction of sectional images in digital holography". *Optics Letters* (36): 2650–2652.
- [34] E. Lam; X. Zhang; H. Vo; T.-C. Poon; G. Indebetouw (2009). "Three-dimensional microscopy and sectional image reconstruction using optical scanning holography". *Applied Optics*. 48 (34): H113–H119
- [35] X. Zhang; E. Lam; T.-C. Poon (2008). "Reconstruction of sectional images in holography using inverse imaging". *Optics Express*. 16 (22): 17215–17226.
- [36] N. Verrier and M. Atlan, "Off-axis digital hologram reconstruction: some practical considerations", *Applied Optics* 50, 34 (2011) H136
- [37] G. Ade, "Digital techniques in electron off-axis holography", *Adv. Electron. Electr. Phys.*, 89 (1994), pp. 1–51
- [38] Berne, B.J.; Pecora, R. *Dynamic Light Scattering*. Courier Dover Publications (2000) ISBN 0-486-41155-9
- [39] (1 January 1970). "Laser Light Scattering". *Annual Review of Physical Chemistry*. 21(1): 145–174
- [40] Pecora., R. (1964). "Doppler Shifts in Light Scattering from Pure Liquids and Polymer Solutions". *The Journal of Chemical Physics*. 40: 1604
- [41] DD Nolte, R An, J Turek, K Jeong, "Holographic tissue dynamics spectroscopy", *Journal of biomedical optics* 16 (8), 087004-087004-13

- [42] DD Nolte, R An, K Jeong, J Turek, Holographic Motility Contrast Imaging of Live Tissues, Chap. in Biomedical Optical Phase Microscopy and Nanoscopy, NT Shaked, Z. Zalevskey, and L. Satterwhite, Eds., ed: Elsevier
- [43] Sutherland RM. Cell and environment interactions in tumor microregions - The multicell spheroid model. *Science*. 1988;240(4849):177-84. doi: 10.1126/science.2451290. PubMed PMID: WOS:A1988M822900027.
- [44] Kunz-Schughart LA, Freyer JP, Hofstaedter F, Ebner R. The use of 3-D cultures for high-throughput screening: The multicellular spheroid model. *Journal Of Biomolecular Screening*. 2004;9(4):273-85. PubMed PMID: ISI:000221980300001.
- [45] Hirschhaeuser F, Menne H, Dittfeld C, West J, Mueller-Klieser W, Kunz-Schughart LA. Multicellular tumor spheroids: An underestimated tool is catching up again. *Journal of Biotechnology*. 2010;148(1):3-15. PubMed PMID: ISI:000280028900002.
- [46] Charoen KM, Fallica B, Colson YL, Zaman MH, Grinstaff MW. Embedded multicellular spheroids as a biomimetic 3D cancer model for evaluating drug and drug-device combinations. *Biomaterials*. 2014;35(7):2264-71. Epub 2013/12/24. doi: 10.1016/j.biomaterials.2013.11.038. PubMed PMID: 24360576.

CHAPTER 2. BIODYNAMIC CHEMOSENSITIVITY TESTING IN REVIVED FRESH-FROZEN BIOPSIES

Acquiring Doppler spectrograms of fresh tumor tissues responding to anticancer agents can be slow and inefficient because of the slow accrual of patients in preclinical or clinical trials. However, if flash-frozen biopsies from tissue banks can be thawed to produce living tissue with relevant biodynamic profiles, then a large reservoir of tissue-banked samples could become available for phenotypic library building. Here, we report biodynamic profiles acquired from revived flash-frozen canine B-cell lymphoma biopsies. In the canine study, we compared the thawed-tissue drug-response spectrograms to spectrograms from fresh tissues from the same dogs. By compensating for tissue trauma in the freezing of the sample, and by compensating for negative-control phenotype, patient clustering of both the fresh and frozen samples were found to have reasonable agreement with clinical outcomes. This chapter demonstrates that previously frozen tumor specimens are a viable proxy for fresh specimens in the context of chemosensitivity testing, and that frozen samples from tissue banks contain enough viable cells to evaluate phenotypic drug response.

2.1 Overview of Canine B-Cell Lymphoma project

Intracellular dynamics in living tissue are dominated by active transport driven by bioenergetic processes far from thermal equilibrium [1]. Cells are highly dynamic systems that continuously undergo internal reconfiguration through random and/or coordinated molecular and mechanical responses. Intracellular dynamics are fundamental processes that support a broad range of functions such as cell migration and division [2]. These intracellular processes are derived from, and often influence, physiological conditions of the cells. Quantitative measurement of intracellular processes would thus aid in building a better understanding of the underlying mechanisms of cellular states and functions.

Biodynamic profiling is an optical imaging technology related to *en face* OCT [3] using partially coherent speckle generated by broad-area illumination with coherence detection through digital holography [4]. Biodynamic profiling penetrates up to 1 mm into living tissue and returns

high-content information in the form of dynamic light scattering across a broad spectral range. The fluctuation frequencies relate to Doppler frequency shifts caused by light scattering from subcellular constituents that are in motion [5]. The speeds of intracellular dynamics range across nearly four orders of magnitude from nanometers per second (cell membrane motion) to tens of microns per second (organelles and vesicles). For a near-infrared backscattering geometry these speeds correspond to Doppler frequencies from 0.01 Hz to 10 Hz. Dynamic light scattering in living tissues has been used to identify intracellular transport signatures of diffusive relative to directed motion [6], for the detection of apoptosis [7], and extracellular restructuring [8]

Dynamic light scattering combined with coherence-gated optical sectioning has led to the development of biodynamic imaging (BDI) [9] and related techniques such as tissue dynamics spectroscopy (TDS) [10]. Biodynamic profiling techniques are sensitive probes of the response of living tissue to applied drugs and therapeutics [9, 11], which has been extended to profiling how living biopsy samples respond to standard-of-care anticancer treatments. Biodynamic studies of chemosensitivity in patients obtain living biopsy samples through the conventional diagnostic process. However, canine B-cell lymphoma and human ovarian cancer trials required several years to enroll approximately 20 in each study [12, 13]. This slow rate of enrollment limits the numbers of samples that can be obtained. To identify biodynamic signatures of drug sensitivity or resistance in the midst of sample-to-sample and patient-to-patient heterogeneity requires phenotypic profiles of at least 50 independent samples depending on the variability of the biodynamic spectral fingerprints.

However, if flash-frozen biopsies could be revived and measured, then a large reservoir of tissue-banked samples could become available for phenotypic library building. In this study, we demonstrate that fresh-frozen biopsy samples can be thawed, and their health stabilized sufficiently to measure biodynamic spectral signatures of their responses to applied therapeutics. The tissue type studied here is canine B-cell lymphoma, for which we have both fresh and frozen tissues as well as the patient clinical outcomes. Biodynamic intracellular processes occur in the thawed tissues that do not match fresh tissue, but these effects can be partially compensated to allow a comparison between fresh and thawed tissues in the case of the canine lymphoma.

2.2 Experimental Set-Up and Procedures

2.2.1 Sample Preparation

Original data on fresh samples were collected from canine B-cell lymphoma patients [7]. All canine patients used in this study were client-owned pet animals with untreated, naturally occurring multicentric lymphoma. The treatment offered for the dogs in this study is a conventional treatment with established efficacy for dogs with multicentric lymphoma. Prior to enrollment of the dogs, the written informed consents were obtained from all owners. The protocol has been approved by the Purdue University Animal Care and Use Committee (PACUC) prior to the enrollments. Once the owner accepted the enrollment, dogs were enrolled based upon presumptive diagnosis of multicentric lymphoma as determined by physical examination and fine needle aspirate cytology of an affected lymph node. Histopathologic confirmation of lymphoma, with subtyping and immunophenotyping performed according to WHO criteria [27], was accomplished in all dogs.

The common treatment in the clinic is to apply CHOP regimen therapy, which is a combination of four cancer drugs (doxorubicin, cyclophosphamide, prednisolone, vincristine). Progression-free survival (PFS) defines the chemotherapy response sensitivity (Table 3). Progression-free survival time is defined as the length of time during and after the treatment that a patient lives with the disease without progression. A PFS longer than 180 days is considered to be a sensitive chemotherapy response for the canine patients.

Table 3 Progression-free survival (PFS) is defined as the length of time during and after the treatment of a disease, such as cancer, that a patient lives with the disease without progression. PFS longer than 180 days is defined as the chemotherapy response sensitive group. From this table, canine patients Kodie, Graciebell, Sinker and Chester are regarded as the drug sensitive group, and canine patients Badger, Scout, Boost are regarded as the drug resistant group.

Patient Profile											
Dog #	Dog name	Date of biopsy	Date of thawed assay	T or B	Histologic diagnosis	Best overall response	PFS	OS	Chemotherapy response		
1	Kodie (Dakota)	2015/4/15	2017/10/24	B	DLBCL	CR	223	244	Sensitive		
2	Graciebell	2015/5/14	2017/9/13	B	DLBCL	CR	384	384	Sensitive		
3	Badger	2015/6/4	2017/12/4	B	DLBCL	PR	64	138	Resistant		
4	Mr. Sinker ¹	2015/6/11	2017/9/29	B	DLBCL	CR	460	460	Sensitive		
5	Scout	2016/3/23	2018/4/4	B	DLBCL	PR	43	58	Resistant		
6	Chester	2016/5/6	2018/4/9	B	DLBCL	CP	244	337	Sensitive		
7	Boost	2016/6/16	2018/4/6	B	DLBCL	CP	98	156	Resistant		

DLBCL = Diffuse large B-cell lymphoma
 CR = Complete remission
 PR = Partial remission
 PFS = Progression-free survival
 OS = Overall survival
¹ Only completed 1/2 of CHOP protocol.

The frozen tissues were snap-frozen in liquid nitrogen within 10-15 minutes of collection from the animal. All of the tissue samples were kept frozen in liquid nitrogen in a large tank in the biorepository until the time of thaw/use. Upon retrieval, the samples were rapidly thawed by agitation in a 37°C water bath and suspended in 37°C RPMI medium containing 10% fetal bovine serum and 100U penicillin/mL-100µg/mL streptomycin. Small 1 mm³ pieces were then assayed using the biodynamic imaging system.

Sixteen canine B-cell lymphoma samples from a single canine patient biopsy were placed in a 96-well plate for each experiment. For each experiment sixteen canine B-cell lymphoma spheroids are placed in a 96-well plate in which there are four negative-control wells treated with 0.1% DMSO carrier and twelve wells treated with the drugs with duplicates (CHOP, prednisolone, vincristine) and triplicates (doxorubicin, cyclophosphamide). The well layout for a single 96-well plate is shown in Figure 2-1.

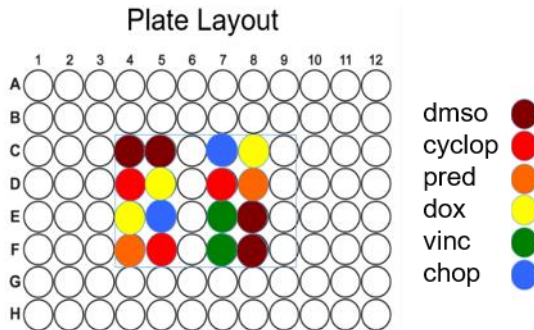


Figure 2-1 Plate layout showing the subset of the 96-well plate used for the 16-plex measurements. Two plates are used per canine patient for a total of 32 wells with a replicate number of 4 or 6 wells per treatment per patient.

2.2.2 Experiment Set-Up

The optical system for canine project is so the called alpha-prime system, which is shown in Figure 1-6 (Section 1.4.1 Biodynamic Profiling System). The low-coherence light source is a superluminescent diode (SLD) with a 20-mW output power and 50 nm bandwidth. The light is split by a polarizing beam splitter in a Mach Zehnder configuration into a signal arm that illuminates the sample and a reference arm that incorporates a delay stage. The light scattered from the sample is collected by a large-diameter (10 cm) lens with a long focal length (15 cm) and relayed to a Fourier plane where it can be apertured. The Fourier plane is then imaged with a demagnification of 1:3 onto the digital camera, where the signal arm intersects the off-axis reference. The hologram is recorded on a Fourier plane so that image reconstruction takes a simple two-dimensional FFT to generate two sidebands that are phase conjugate images that represent an optical section of the sample with a section thickness related to the coherence length of the light source. Scanning the delay stage shifts the coherence gate through the sample up to 1 mm deep.

2.3 Fluctuation Spectroscopy and Drug-response Spectrograms

The patient profiles in this study are given in Table 3. Biodynamic time–frequency spectrograms $D(\omega, t)$ were acquired for the seven enrolled fresh dogs under four treatments (doxorubicin, prednisolone, vincristine and cyclophosphamide) including wells dosed only with the DMSO carrier as negative controls. Each treatment was measured using three-to-five replicates in randomized well locations. The averaged spectrograms of the negative control (DMSO) are shown in Figure 2-2 for fresh samples, thawed samples and their difference, respectively. The spectrogram of the fresh samples shows a progressing inhibition of activity for low and mid

frequencies. The decrease in activity with time is often associated with naturally decreasing sample health after surgery. The spectrogram for the thawed samples shows a strong inhibition across the full bandwidth. This stronger suppression is likely caused by the tissue damage associated with the freeze-thaw process. The difference of the thawed DMSO spectrogram relative to the fresh shows strongest suppression in high and low frequencies.

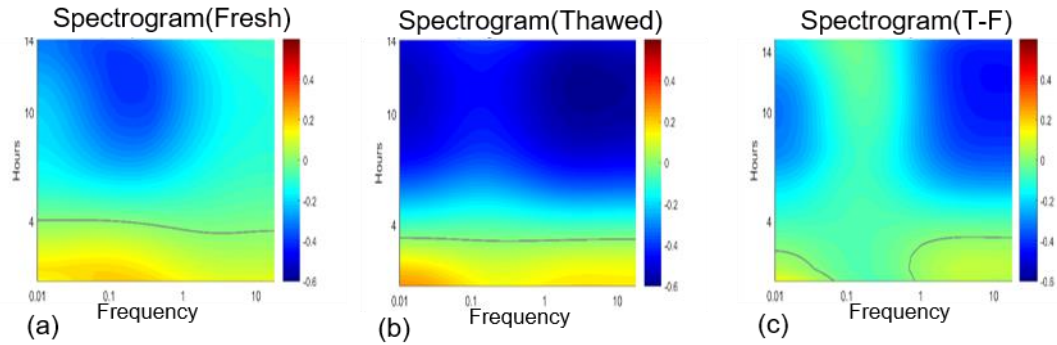
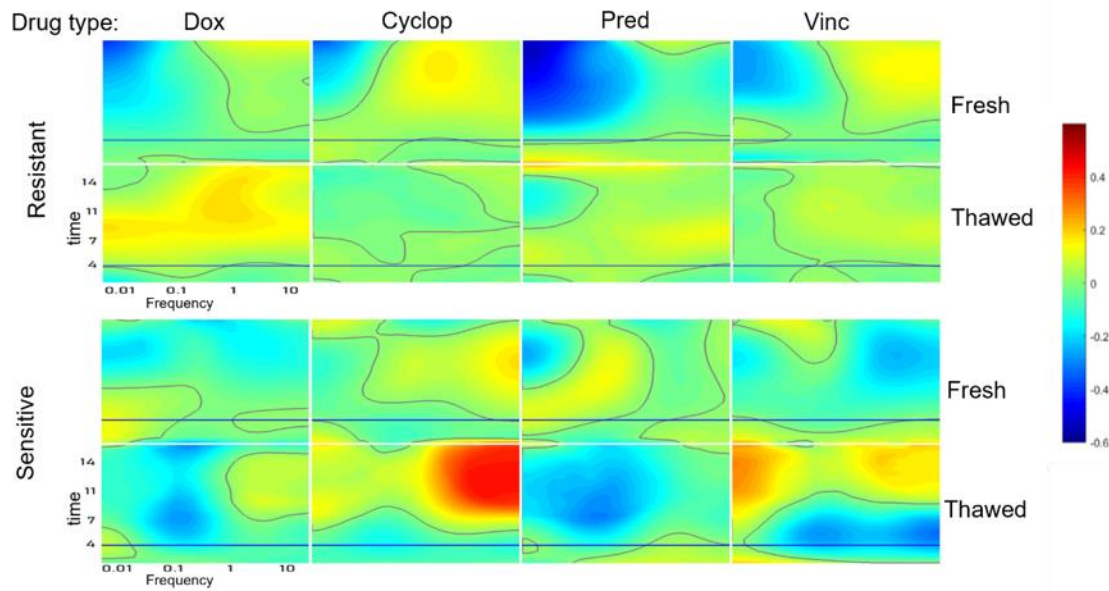


Figure 2-2 Negative control (DMSO-based response) spectrograms. DMSO (0.1%) has been applied after 4 hours. (a) spectrograms for fresh biopsy, (b) spectrograms for thawed sample, (c) the difference of spectrogram between thawed samples and fresh biopsies. The replicate numbers of fresh and thawed sample are 55 and 56, respectively.

The averaged spectrograms are arranged in Figure 2-3 in four groups according to clinical outcomes: 1) fresh drug-resistant group, 2) thawed drug-resistant group, 3) fresh drug-sensitive group, 4) thawed drug-sensitive group for the four drug treatments. When comparing the trend for overall spectral response between the fresh and thawed cohorts with respect to the chemotherapy response phenotype, there is only a moderate correlation between drug response of fresh and thawed samples.

Drug Response of Frozen Samples versus Fresh Samples *

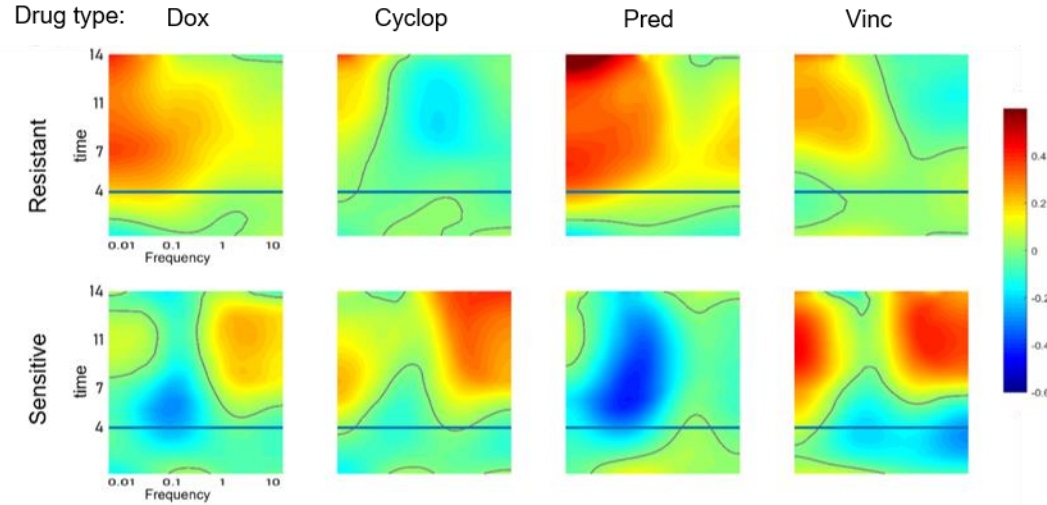


* All the drug response results have already subtracted their corresponding dmso response

Figure 2-3 Relative Spectrogram Comparison of Fresh/Thawed and drug-Sensitive/Resistant for the BDI results. Each column stands for a relative spectrogram (negative control subtracted) comparison based on one specific drug response under four different conditions: fresh drug-resistant biopsy, thawed drug-resistant biopsy, fresh drug-sensitive biopsy, thawed drug-sensitive biopsy. X-axis is Frequency, Y-axis is measurement time. Drug was applied after 4 hours. All the drug response spectrograms have already subtracted the corresponding negative control response spectrogram.

The differences of average spectrograms of the thawed relative to the fresh cohort are shown in Figure 2-4. These figures show a similar response within the same phenotype. For instance, all the drug-resistant spectrograms show a strong enhancement in low frequency, while all the drug-sensitive spectrograms show a strong enhancement in high frequency. These data show a consistent trend for overall enhanced spectral responses in short-PFS phenotypes relative to long-PFS phenotypes when under treatment. These spectrograms indicate that the trauma effect of the freeze/thaw can be compensated.

Power Spectrogram of Extra Drug response based on freezing trauma*



- I.e. power spectrogram of thawed drug relative to dmso response subtract that of fresh drug relative to dmso response

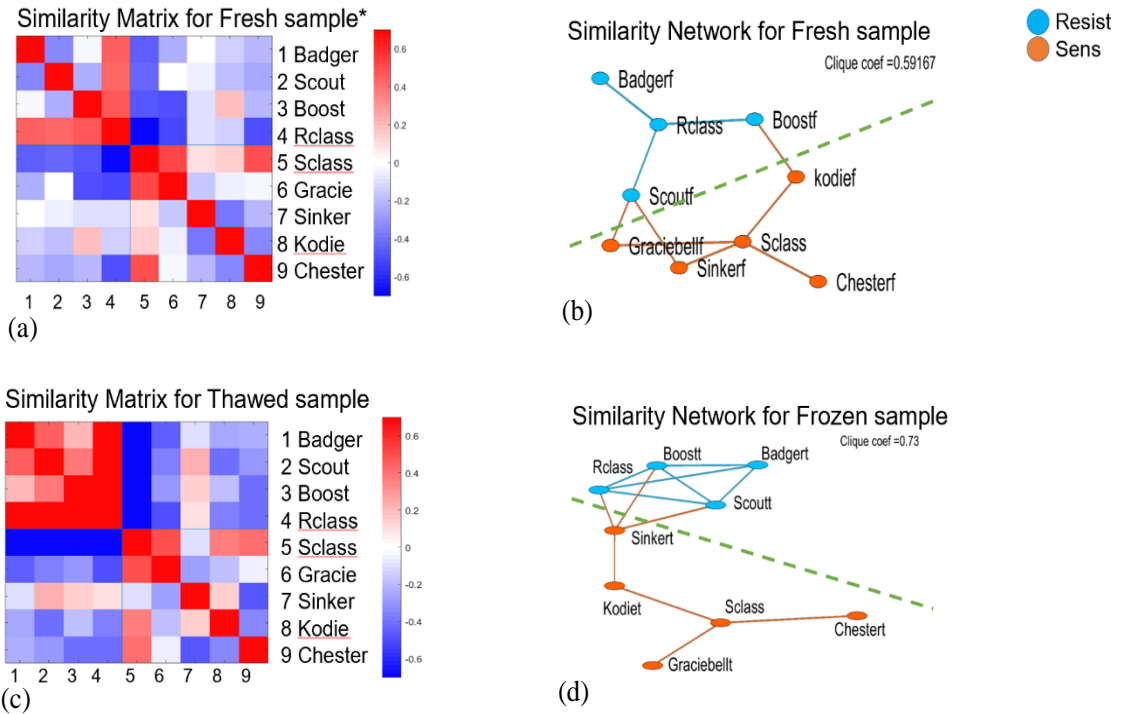
Figure 2-4 Relative Spectrograms (negative control subtracted) for drug responses. The relative spectrograms generated by subtracting from the spectrogram of thawed samples subtracting the spectrogram of corresponding fresh biopsies grouped for the same chemotherapy. X-axis is Frequency, Y-axis is measurement time. Drug is applied after 4 hours.

2.4 Machine Learning and Data Clustering

A key goal of this preclinical study is to construct a chemoresistance classifier that takes a set of treatment spectrograms for a single patient and predicts whether the patient will have a sensitive response to a selected treatment regimen. To accomplish this, the drug-response spectrograms for each patient are deconstructed into a set of mathematical features, each capturing either local or global patterns. Examples include overall enhancement/suppression across all frequencies; localized low, mid, and high frequencies; red shifts or blue shifts; and different time dependences in response to the applied therapeutic, among others. There are 40 such biodynamic feature vectors that are defined, descriptions of which can be found in previous chapters and publications on biodynamic profiling [9, 14, 15]. The construction of the classification algorithm is based on separability in a feature space. The time-frequency drug-response spectrograms for each patient are deconstructed into a set of features, each capturing either local or global spectrogram patterns. Examples include overall enhancement/suppression over all frequencies

(ALLF, ALLFT); localized low, mid and high (HI) frequencies; red shifts or blue shifts (SDIP); and different time dependences in response to the applied treatment (SDIP vs. SDIP2 and ALLF vs. ALLFT).

In Figure 2-5, a) is the similarity matrix. Each grid stands for a correlation coefficient of 32 biomarkers between the two corresponding patients. The similarity network is generated by the similarity matrix, which can be seen in b). The similarity-based network represents the clustering result. The clique coefficient, which is defined as the accuracy of matched links, is near to 60 percent. The resistant cohort and the sensitive cohort are clearly separated by the clustering of the correlation coefficients between every two samples. c) and d) are the similarity matrix and similarity network of the thawed groups. The clique coefficient of the thawed groups analysis result is even higher than the fresh groups, which comes to 73 percent accuracy. It proves further that thawed groups can be used to do the biodynamic profiling measurements. These results indicate that the two types of chemotherapy response groups can be distinguished by comparing fresh cohorts or thawed cohorts.



*Each grid stands for the correlation coefficient of 32 biomarkers between the two corresponding samples

Figure 2-5 Similarity matrix and clustered network for fresh & thawed group. (a), Similarity matrix for fresh group, 1-3 means for fresh resistant dogs, 4 is the averaged fresh resistant group, 5 is the averaged fresh sensitive group, 6-9 means for fresh sensitive dogs. Each color stands for the correlation coefficient of 32 biomarkers between the two corresponding dog samples. The matrix shows a crude block diagonal pattern with two main groups. (b) Similarity network for fresh groups, blue dots are resistant ones, orange dots are sensitive ones. Clique coefficient is defined as the accuracy of matching links. (c) Similarity matrix for thawed group, 1-3 means for thawed resistant dogs, 4 is the averaged thawed resistant group, 5 is the averaged thawed sensitive group, 6-9 means for thawed sensitive dogs. Each color stands for the correlation coefficient across 32 biomarkers between the two corresponding dog samples. The matrix shows a block diagonal pattern with two main groups. (d) Similarity network for thawed groups, blue dots are resistant dogs, and orange dots are sensitive dogs. The clique coefficient is defined as the accuracy of matching links.

A combination result of all fresh and thawed samples is shown in Figure 2-6. The clique coefficient is much smaller after combining the fresh and thawed groups. Many of the patients are clustered into the wrong group. For example, drug-sensitive patients fresh Kodie, thawed Sinker, fresh Sinker are misclassified as drug-resistant group; Drug-resistant patient fresh Badger is misclassified as drug-sensitive group. This result shows relatively low classification as expected because of the trauma effect mentioned before.

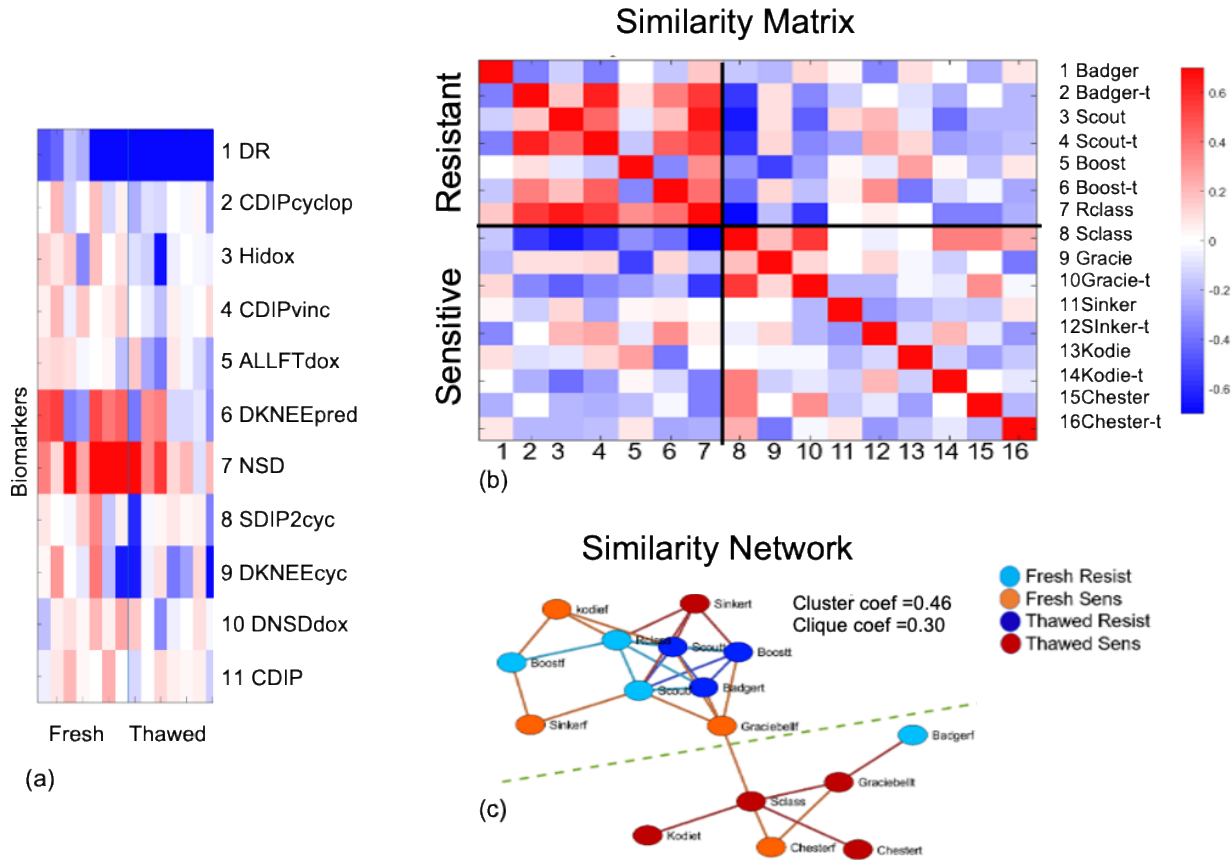
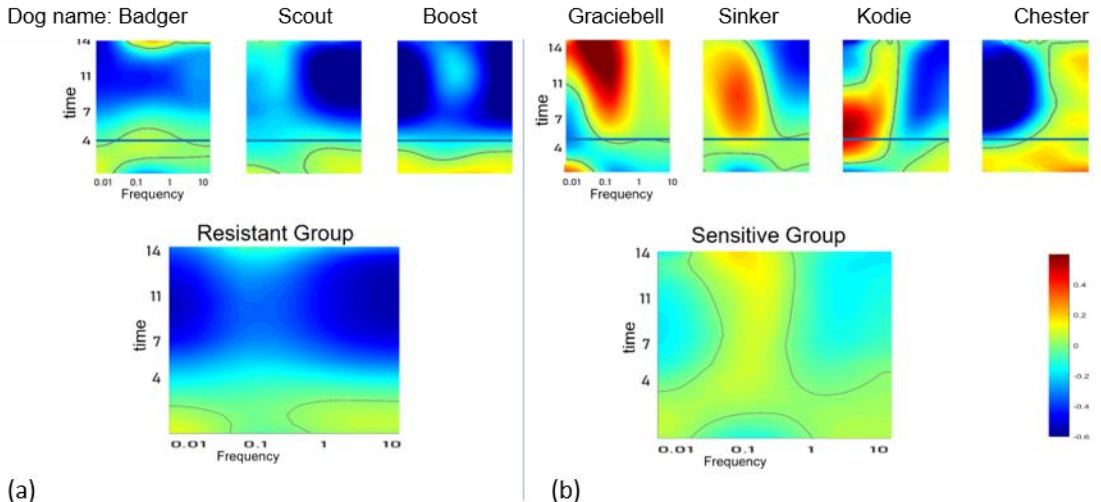


Figure 2-6 Clustering analysis. (a) Selected biomarkers which are most important features for distinguishing the two different cohorts. (b) Similarity Matrix for all dogs (1-7 represents resistant groups, 8-16 represents the sensitive groups). Each grid stands for the correlation coefficient of 32 biomarkers between the two corresponding dog samples. The matrix shows a weak block diagonal pattern with two main groups. (c) Similarity network for all dogs, blue dots are resistant ones, red dots are sensitive ones. Clique coefficient is defined as the accuracy of matching links.

These averages have a relatively large variance patient-to-patient, yet the thawed resistant cohort tends to share common behavior that is different from the thawed sensitive cohort when compared to the DMSO spectrograms of the corresponding fresh sample spectrograms. This is shown in Figure 2-7 for the seven dogs. The sensitive group shows more spectral enhancements relative to fresh than the resistant group. It is striking that the response of the tissues to growth medium is systematically different between the resistant/sensitive phenotypes.

Power Spectrogram of Dmso response based on freezing trauma*

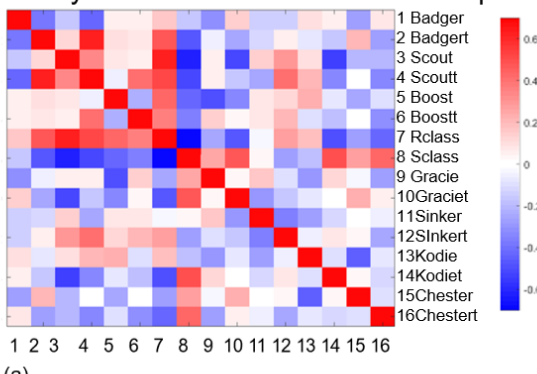


- I.e. power spectrogram of thawed dmso response subtract that of fresh dmso response

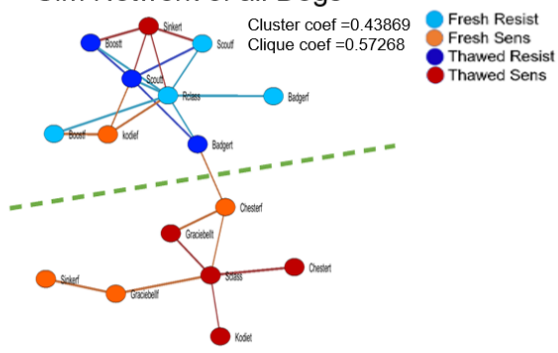
Figure 2-7 Individual spectrograms of DMSO (negative control) response for thawed samples. X-axis is Frequency, Y-axis is measurement time. DMSO has been applied after 4 hours. (a) Difference between spectrogram of dmso response for fresh and thawed resistant group (patient name Badger, Scout, Boost). (b) Difference between spectrogram of dmso response for fresh and thawed sensitive group (patient name Graciebell, Sinker, Kodie, Chester).

The thawed trauma can be eliminated by subtracting the averaged excess negative control response. Figure 2-8 shows the result of all fresh and thawed samples after the compensation. 12 out of 14 samples are classified correctly. These clustering results show a clearer distinction between the different chemotherapy response groups. It also shows that the compensation can remove the excess effect of the thawing damage.

Similarity Matrix for Fresh&Thawed samples*



Sim Network of all Dogs



- Each grid stands for the correlation coefficient of biomarkers between the two corresponding samples.

Figure 2-8 Similarity matrix after freezing trauma compensation. (a) Similarity Matrix for all dogs after compensation (1-7 stands for resistant groups, 8-16 stands for sensitive groups). Each color stands for the correlation coefficient among 32 biomarkers between the two corresponding dog samples. The matrix shows a weak block diagonal pattern with two main groups. (b) Similarity network for all dogs after compensation, blue dots are resistant ones, red dots are sensitive ones. Clique coefficient is defined as the accuracy of match lines.

2.5 Discussion

The challenge for many clinical drug studies is the time necessary (sometimes months to years) to follow patient response to determine effectiveness. The use of frozen banked tissue with known clinical outcome represents a possible source of material for testing, provided enough cells survive the freezing and thawing process, and they maintain their phenotype. The goal of this project was to determine if frozen cancer samples could be used to accurately assess drug response phenotype. Many cells in a frozen sample will be damaged due to ice crystal formation and will not survive the thaw process. However, some percentages do survive, and cells can be grown out from frozen tissues. In addition to the problem of cryo-damage to the cells, there is also the question of whether the surviving cells would maintain the drug response phenotype as noted in the pathology report.

2.6 Conclusion

The use of biodynamic profiling to study drug response in fresh tissues utilizes a 4-hour stabilization period in culture, followed by a 14-hour measurement period. The drugs used in this study have characteristic spectral signatures for resistant/responsive phenotypes that we have observed in fresh tissues. Sensitive phenotypes typically show a decrease of overall Doppler activity, whereas the resistant phenotypes often have increased intracellular activity.

This study demonstrates that sufficient viable cells exist in a thawed sample to assess drug-response phenotypes using biodynamic profiling. The relatively short culture time for biodynamic profiling analysis may be essential for this success. A significant advantage of biodynamic profiling is that the tissue can be monitored in the multiwell plate during the whole process relatively soon after thawing. A more prolonged processing and/or culture time would likely not provide similarly consistent data since degradative processes (apoptosis, necrosis) can be triggered by the freeze-thaw stress.

Similar to previous studies using fresh living 3D tissues, biodynamic profiling has been shown to be capable of accurately measuring drug response in revived frozen tumor tissue. This

is a valuable capability for retrospective studies and can also be used to match the drug response phenotype with genotypic data.

2.7 Reference

- [1] R. An, D. Merrill, L. Avramova, J. Sturgis, M. Tsiper, J. P. Robinson, J. Turek, and D. D. Nolte, "Phenotypic Profiling of Raf Inhibitors and Mitochondrial Toxicity in 3D Tissue Using Biodynamic Imaging," *Journal Of Biomolecular Screening*, vol. 19, no. 4, pp. 526-537, Apr (2014)
- [2] D. Merrill, H. Sun, J. Turek, D. Nolte, B. Yakubov, D. Matei, and R. An, "Intracellular Doppler Signatures of Platinum Sensitivity Captured by Biodynamic Profiling in Ovarian Xenografts," *Nature Scientific Reports*, vol. 6, p. 18821, Jan., 2016 (2016)
- [3] D. D. Nolte, R. An, J. Turek, and K. Jeong, "Holographic tissue dynamics spectroscopy," *Journal of Biomedical Optics*, vol. 16, no. 8, pp. 087004-13, Aug (2011), Art no. 087004
- [4] H. J. Burstein, P. B. Mangu, M. R. Somerfield, D. Schrag, D. Samson, L. Holt, D. Zelman, and J. A. Ajani, "American Society of Clinical Oncology Clinical Practice Guideline Update on the Use of Chemotherapy Sensitivity and Resistance Assays," *Journal Of Clinical Oncology*, vol. 29, no. 24, pp. 3328-3330, Aug 20 (2011)
- [5] D. Siolas and G. J. Hannon, "Patient-Derived Tumor Xenografts: Transforming Clinical Samples into Mouse Models," *Cancer Research*, vol. 73, no. 17, pp. 5315-5319, Sep (2013)
- [6] M. R. Custead, R. An, J. J. Turek, G. E. Moore, D. D. Nolte, and M. O. Childress, "Predictive value of ex vivo biodynamic imaging in determining response to chemotherapy in dogs with spontaneous non-Hodgkin's lymphomas: a preliminary study," *Convergent Science Physical Oncology*, vol. 1, no. 1, p. 015003, (2015)
- [7] H Choi, Z Li, H Sun, D Merrill, J Turek, M Childress and D Nolte, " Biodynamic digital holography of chemoresistance in a pre-clinical trial of canine B-cell lymphoma ", *Biomedical optics express*, 2018

- [8] O. Thouvenin, K. Grieve, P. Xiao, C. Apelian, and A. C. Boccara, "En face coherence microscopy Invited," *Biomedical Optics Express*, vol. 8, no. 2, pp. 622-639, Feb 1 (2017)
- [9] K. Jeong, J. J. Turek, and D. D. Nolte, "Speckle fluctuation spectroscopy of intracellular motion in living tissue using coherence-domain digital holography," *Journal of Biomedical Optics*, vol. 15, no. 3, p. 030514, May-Jun (2010)
- [10] Z. Li, H. Sun, J. Turek, S. Jalal, M. Childress, and D. D. Nolte, "Doppler fluctuation spectroscopy of intracellular dynamics in living tissue," *Journal of the Optical Society of America a-Optics Image Science and Vision*, vol. 36, no. 4, pp. 665-677, Apr (2019)
- [11] J. Lee, W. C. Wu, J. Y. Jiang, B. Zhu, and D. A. Boas, "Dynamic light scattering optical coherence tomography," *Optics Express*, vol. 20, no. 20, pp. 22262-22277, Sep (2012)
- [12] G. Farhat, A. Giles, M. C. Kolios, and G. J. Czarnota, "Optical coherence tomography spectral analysis for detecting apoptosis in vitro and in vivo," *Journal of biomedical optics*, vol. 20, no. 12, pp. 126001-126001, 2015-Dec (2015)
- [13] R. L. Blackmon, R. Sandhu, B. S. Chapman, P. Casbas-Hernandez, J. B. Tracy, M. A. Troester, and A. L. Oldenburg, "Imaging Extracellular Matrix Remodeling In Vitro by Diffusion-Sensitive Optical Coherence Tomography," *Biophysical Journal*, vol. 110, no. 8, pp. 1858-1868, Apr (2016)
- [14] D. Needleman and Z. Dogic, "Active matter at the interface between materials science and cell biology," *Nature Reviews Materials*, vol. 2, no. 9, Sep (2017), Art no. 17048
- [15] A. A. Gerencser and D. G. Nicholls, "Measurement of instantaneous velocity vectors of organelle transport: Mitochondrial transport and bioenergetics in hippocampal neurons," *Biophysical Journal*, vol. 95, no. 6, pp. 3079-3099, Sep 15 (2008)
- [16] R. An, D. Merrill, L. Avramova, J. Sturgis, M. Tsiper, J. P. Robinson, J. Turek, and D. D. Nolte, "Phenotypic Profiling of Raf Inhibitors and Mitochondrial Toxicity in 3D Tissue Using Biodynamic Imaging," *Journal Of Biomolecular Screening*, vol. 19, no. 4, pp. 526-537, Apr (2014)

- [17] D. D. Nolte, R. An, J. Turek, and K. Jeong, "Tissue dynamics spectroscopy for phenotypic profiling of drug effects in three-dimensional culture," *Biomedical Optics Express*, vol. 3, no. 11, pp. 2825-2841, Nov (2012)
- [18] H. Sun, D. Merrill, R. An, J. Turek, D. Matei, and D. D. Nolte, "Biodynamic imaging for phenotypic profiling of three-dimensional tissue culture," *Journal of Biomedical Optics*, vol. 22, no. 1, Jan (2017), Art no. 016007
- [19] Z. Li, R. An, W. M. Swetzig, M. Kanis, N. Nwani, J. Turek, D. Matei, and D. Nolte, "Intracellular optical doppler phenotypes of chemosensitivity in human epithelial ovarian cancer," *Scientific Reports*, vol. 10, no. 1, p. 17354, 2020/10/15 (2020)
- [20] H. Choi, Z. Li, H. Sun, D. Merrill, J. Turek, M. Childress, and D. Nolte, "Biodynamic digital holography of chemoresistance in a pre-clinical trial of canine B-cell lymphoma," *Biomedical Optics Express*, vol. 9, no. 5, pp. 2214-2228, 2018/05/01 (2018)
- [21] D. Merrill, H. Sun, J. Turek, D. Nolte, B. Yakubov, D. Matei, and R. An, "Intracellular Doppler Signatures of Platinum Sensitivity Captured by Biodynamic Profiling in Ovarian Xenografts," *Nature Scientific Reports*, vol. 6, p. 18821, Jan., 2016 (2016)
- [22] D. D. Nolte, R. An, J. Turek, and K. Jeong, "Holographic tissue dynamics spectroscopy," *Journal of Biomedical Optics*, vol. 16, no. 8, pp. 087004-13, Aug (2011), Art no. 087004
- [23] H. J. Burstein, P. B. Mangu, M. R. Somerfield, D. Schrag, D. Samson, L. Holt, D. Zelman, and J. A. Ajani, "American Society of Clinical Oncology Clinical Practice Guideline Update on the Use of Chemotherapy Sensitivity and Resistance Assays," *Journal Of Clinical Oncology*, vol. 29, no. 24, pp. 3328-3330, Aug 20 (2011)
- [24] D. Siolas and G. J. Hannon, "Patient-Derived Tumor Xenografts: Transforming Clinical Samples into Mouse Models," *Cancer Research*, vol. 73, no. 17, pp. 5315-5319, Sep (2013)
- [25] M. R. Custead, R. An, J. J. Turek, G. E. Moore, D. D. Nolte, and M. O. Childress, "Predictive value of ex vivo biodynamic imaging in determining response to chemotherapy in dogs with spontaneous non-Hodgkin's lymphomas: a preliminary study," *Convergent Science Physical Oncology*, vol. 1, no. 1, p. 015003, (2015)

- [26] H. Choi, Z. Li, Z. Hua, J.Zuponcic, E. Ximenes, J. Turek, M. Ladisch and D. Nolte, "Doppler imaging detects bacterial infection of living tissue", vol 4, p. 178-178 (2021)

CHAPTER 3. BIODYNAMIC PROFILING OF HUMAN ESOPHAGEAL CANCER HETEROGENEITY

Biodynamic profiling of living tissue is a form of dynamic-contrast optical coherence tomography (DC-OCT) that uses digital holography to measure changes in Doppler spectra caused by drug effects on intracellular transport. A previous clinical trial profiling human ovarian cancer biopsies compared averaged Doppler profiles to patient treatment outcomes, finding a correspondence between average biodynamic signatures and patient chemosensitivity [21]. However, averaging can remove important signatures among the varying well-to-well drug-responses due to spatial heterogeneity of the biopsy microenvironment. A recent human esophageal cancer pilot clinical trial of biodynamic profiling of platinum-based combination therapies displayed highly heterogeneous responses to the *in vitro* treatments. The drug responses for 28 esophageal cancer patients generated more than 600 biodynamic profiles on a per-well basis that were categorized into four biodynamic phenotypes, of which two were found to correlate with patient outcomes. One non-predictive phenotype showed a systemic red-shift of frequencies, indicating compromised health and low-responsivity. The Doppler spectrograms were used as the training set for a novel Siamese neural network autoencoder. The network optimization performs locality-sensitive hashing for dimensionality reduction and subsequent correlation with chemosensitivity. A statistically significant correspondence was observed between the biodynamic signatures and the likelihood of patient cancer remission.

3.1 Overview of Human Esophageal Cancer project

Esophageal cancer is the 6th leading cause of cancer death in men in the US and the 8th leading cause worldwide. Esophageal cancer is a gastrointestinal cancer that infiltrates trachea and local blood vessels and spreads readily through metastasis [1]. The majority of patients are diagnosed with locally advanced esophageal cancer and are treated with chemotherapy and radiation followed by surgical resection [2-6]. Complete responses with chemotherapy and

radiation are achieved in only 28% of patients with the majority of patients suffering from significant toxicities of chemotherapy and radiation without improvements in outcomes [7]. Development of a methodology that can predict response to chemotherapy would be useful for identifying patients most likely to achieve pathologic complete response (pCR). With such a predictive assay, patients who are least likely to achieve pCR could be directed to localized treatment options to avoid the morbidity associated with ineffective systemic chemotherapy. At the present time, such a predictive assay is not available. Treatment selection has been empirical and has not been individualized to tumor characteristics. Chemosensitivity assays for esophageal cancer include an ATP assay [8]. However in vitro chemo-sensitivity assays may suffer from low predictive value because they have limited ability to yield cells from clinical specimens, lacked predictive power for subsequent clinical applications [9-12], and relied solely on the epithelial tumor components. Significantly, tumors show heterogeneous genotypes and phenotypes [13-15] that pose challenges when quantifying patient response to treatment.

Biodynamic profiling of living biopsy samples fills this gap by retaining the tumor microenvironment with both spatial and genetic heterogeneity, including a hypoxic core in the small biopsy samples that recapitulate the natural oxygen levels in small avascular tumors. Biodynamic imaging is a form of *en face* (or full frame) optical coherence tomography [16] performed with off-axis digital holography as the coherence gate [17, 18]. The full-frame operation with broadly illuminated samples encourages the formation of high-contrast speckle. From living samples, the speckle is highly dynamic, incorporating the difference frequencies among a wide range of Doppler frequency shifts caused by intracellular and cellular motion in living tissue [19]. The frequency range of the Doppler spectrum spans from 10 mHz to 10 Hz corresponding to membrane rearrangements moving at speeds of nanometers per second, up to fast organelles and vesicle transport at speeds of microns per second, respectively. The light-scattering spectrum of living tissue is similar to the diffusive spectrum of Brownian motion obtained in dynamic light scattering, but the physical origins are different. Brownian motion is a Wiener process characterized by mean-square displacements with no associated velocities. In contrast, intracellular motions have characteristic short-term speeds and persistence lengths longer than a reduced wavelength inside the tissue (typically $\lambda/4\pi n = 50$ nm) that places living tissue in the Doppler light-scattering regime [19]. The motion in living tissue is a random walk actively driven by energetic molecules such as ATP and GTP, creating a diffusive spectrum that is far out of

equilibrium and characterized by an effective diffusion constant given by $D_{\text{eff}} = v\tau^2$, where v is the mean-squared speed of the dominant light-scattering component, and τ is the average persistence time for directed motion.

When drugs or other treatments are applied to living samples (*ex vivo*), the motions inside the living tissue are modified, producing changes in the Doppler spectrum. These changes can be specific to different types of biological processes, producing signatures (or spectral fingerprints) of the tissue response to the treatment [28]. One of the goals of biodynamic imaging is to identify patients who will not respond to their cancer treatments so that they can be steered away from ineffective and towards beneficial treatments. Strong correlation of biodynamic signatures of the biodynamic responses of biopsies have been observed in canine B-cell lymphoma [20] and in human epithelial ovarian cancer [21]. In the previous work, drug-responses were averaged over replicate wells. In this paper on a clinical pilot trial of human esophageal cancer under platinum-based combination therapies, the full well-to-well variability was retained and utilized by a novel Siamese neural network autoencoder to improve the predictive accuracy of the biodynamic assay.

3.2 Methods

This study used a form of dynamic-contrast optical coherence tomography (OCT) to generate biodynamic profiles of enrolled esophageal cancer patients. Tumor heterogeneity was recapitulated in the well-to-well variability of the biodynamic profiles which provide rich information content for a moderately-deep Siamese autoencoder neural network.

3.2.1 Experiment Set-Up

A diagram and explanation of the OCI system is found in Section 1.4.1 Biodynamic Profiling System. OCI frames of each tumor section were captured in cycles every 40-48 minutes on average. Each capture sequence consisted of 15-45 seconds travel time to allow the system to transition between tumors, followed by frame capture: 10 background frames captured at 10 frames per second (fps) with the reference beam not zero-path matched, then 50 frames at 0.5 fps and 500 frames at 25 fps with the reference beam zero-path matched. Tumor sections were observed for 6 cycles (4.8 hours) to allow the samples to stabilize. Then half of the growth medium

(~150 μ L) was removed from each well and replaced with a drug at twice the intended concentration to limit disturbing the sample. Tumors were then observed for a further 12 cycles (9.6 hours).

3.2.2 Sample preparation

Esophageal patient biopsies were obtained from Indiana University Hospital. Harvested tumors were placed in ice-cold media and were transported to Prof. Turek's laboratory within 2 hours and prepared for imaging. Half the biopsy was immediately prepared while the other half was maintained at 4 °C for up to 36 hours before testing. Biopsies were sectioned using a razor blade to cut the tumor into pieces of approximately 1 mm³ in volume. Pieces were affixed inside 96-well plates using a small drop of GLUture (Abbot Laboratories) and covered with agarose. Growth medium was added to each well. Experiments were performed immediately after plates were prepared.

Chemotherapy drugs including cisplatin, carboplatin, fluorouracil (5-FU), and paclitaxel (taxol) were obtained from Selleck Chemicals. Dimethyl sulfoxide (DMSO) was from Sigma-Aldrich. Drugs were prepared to twice the desired concentration to allow for later mixing inside the sample well. Drug concentrations were: 25 μ M for cisplatin, carboplatin, and 5-FU; and 10 μ M for taxol. 0.1% DMSO dissolved in growth medium was used as the negative control in all experiments. DMSO was selected since it is the carrier for the other drugs before being added to growth medium to improve solubility.

3.2.3 Clinical Trial Patient Enrollment for Esophageal Cancer

Patients with a diagnosis of esophageal adenocarcinoma who planned to undergo endoscopic ultrasound (EUS) for staging could be seen in the Thoracic Surgery clinic, Medical Oncology clinic or by Gastroenterology at the IU School of Medicine Hospital. As part of the clinic visit, a review of clinical information took place. Patients who appeared to be eligible for this trial underwent the Informed Consent Process during the clinic visit and were screened for eligibility prior to their endoscopy procedure (see **Appendix. B**). A signed consent and completed

eligibility checklist was provided to the Clinical Trials Office prior to registration. All patients were registered with the Indiana University Cancer Center Clinical Trials Office and assigned a unique subject identifier. Regulatory files were maintained by the Clinical Trials Office and applicable regulatory documents were completed and on file prior to registration of any patients.

Upon enrollment, patients were treated with physician-choice chemotherapy of either carboplatin+taxol (CT) or cisplatin+5fu (CF). They underwent re-staging and surgical resection as is standard. At the time of surgical resection, pathological response was analyzed as recommended by the following college of American Pathologists guidelines:

- No residual tumor (complete response, grade 0; 0% tumor)
- Marked response (grade 1, minimal residual cancer, 0 - <10% residual tumor)
- Moderate response (grade 2; 10-50% residual tumor)
- No definite response identified (grade 3, poor or no response; >50% residual tumor)

Patients with no residual tumor are considered complete responders. Patients with no definite response are considered as non-responders. Patients with either marked or moderate response were considered as partial responders to create a three-class outcome for the neural network training.

The patient treatments and outcomes are given in Table 6 of the Supplemental Information. The two main treatments were carboplatin + taxol and cisplatin + 5fu, although at least one patient received oxaliplatin + 5fu. The drug response of patient samples is primarily to platinum and hence all treatments in this trial are considered equivalent. The treatment regimens are described in Table 4. All drugs were solubilized in 0.1% dimethyl sulfate (dmso) which is also pipetted into selected wells as a negative control.

Table 4 *Ex Vivo* Treatments

Treatment	Concentration
dmso	0.1%
carboplatin	25 μ M
Taxol	10 μ M
carboplatin+ Taxol	25+10 μ M
cisplatin	25 μ M
5FU	25 μ M
cisplatin+ 5FU	25+25 μ M

3.2.4 Spectrogram Heterogeneity

Tissue dynamics spectroscopy (TDS) of a living biopsy sample measures the relative change in the Doppler fluctuation spectrum in response to an applied therapeutic or other perturbation of the biopsy. A single biopsy of approximately 50 mm^3 is separated using a scalpel into approximately 32 samples of 1 mm^3 volume each that are placed into a multiwell plate. Several of these samples receive replicate treatments. However, the TDS drug spectrograms across these subsets of a biopsy may display several different phenotypes related to the baseline conditions. While previous work has identified and characterized the average spectral response of the samples, most samples have a more complicated drug response structure. Therefore, in this chapter, the full well-to-well variability is retained for downstream analysis.

The inter-sample variability in the TDS signatures, originating from tumor heterogeneity, poses a challenge for the prediction of patient response to therapy. The drug-response spectrograms from a single patient (Esophageal patient 31) are shown in Figure 3-1 as an example of the heterogeneity of the multiple spectrograms. This patient sample was treated with DMSO (0.1%), carboplatin ($25\mu\text{M}$), taxol ($10\mu\text{M}$), 5FU fluorouracil ($25\mu\text{M}$), cisplatin ($25\mu\text{M}$) and the combo of carboplatin and taxol ($25\mu\text{M}+10\mu\text{M}$). The horizontal axis shows frequencies in the range from 10 mHz to 10 Hz. The vertical axis stands for drug response time. The solid blue line is when the treatment is applied. The axes are the same for all spectrograms.

Figure 3-1 (a) shows the averaged drug-response spectrograms, and Figure 3-1(b) shows the spectrogram collage for each well. The replicate number for each treatment is three or four. As an example of the well-to-well variability, the Carboplatin drug-response spectrograms under the same treatment show different spectrograms for each well. The first well shows a low-frequency suppression and a slight mid-frequency enhancement (less than 10% change of power density). The second and the third wells show a relatively stronger low-frequency and high-frequency suppression, and a mid-frequency enhancement. The fourth well shows a strong low-frequency enhancement and a deep mid and high frequency suppression. The wells for taxol treatment show similar variability. The heterogeneity of these spectrograms makes the averaged spectrograms of the replicate wells a compromise that neutralizes the different well-based phenotypes that contribute to the training of the neural network.

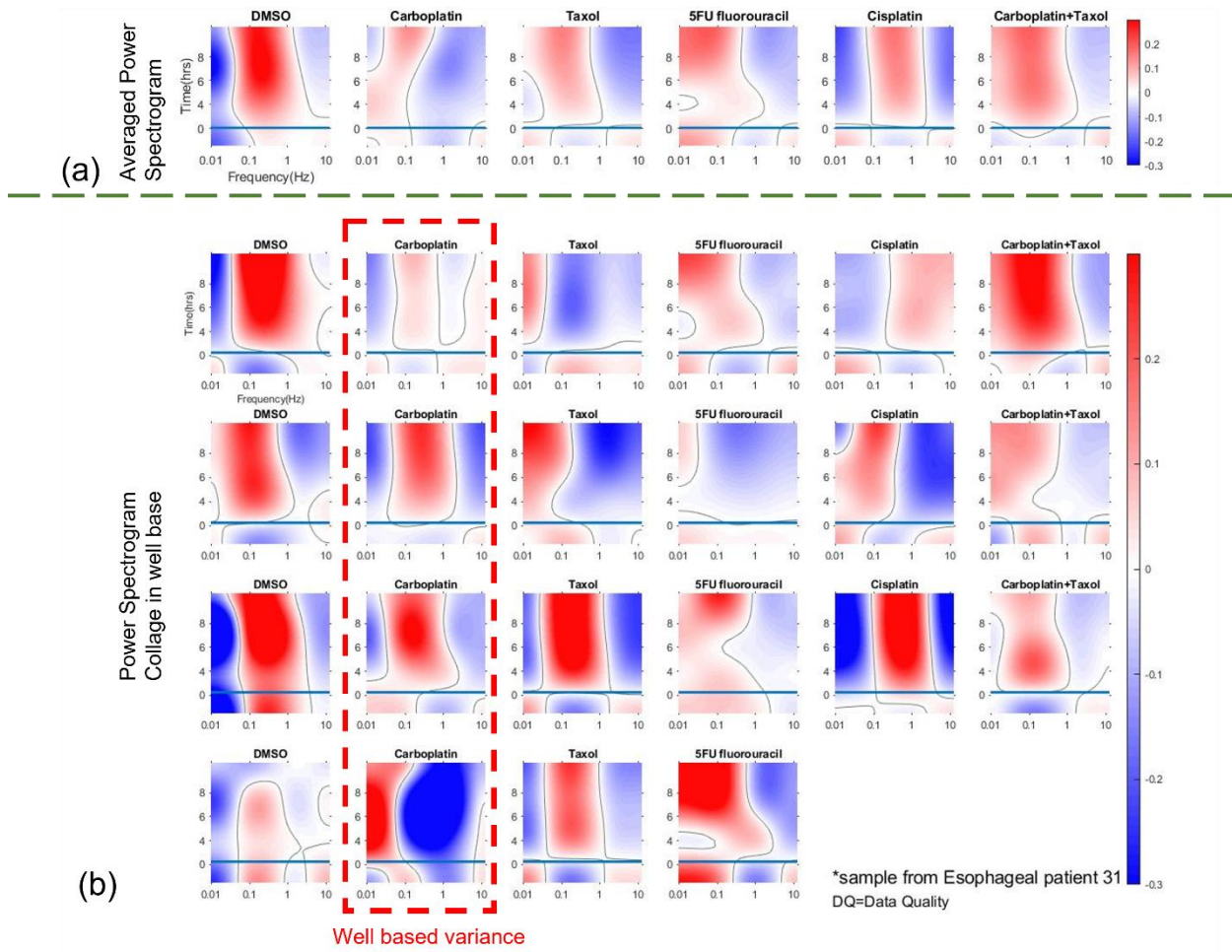


Figure 3-1 Drug-response spectrograms from a single patient treated with DMSO (0.1%), carboplatin ($25\mu\text{M}$), taxol ($10\mu\text{M}$), 5FU fluorouracil ($25\mu\text{M}$), cisplatin ($25\mu\text{M}$) and the combination therapies of carboplatin and taxol and cisplatin and 5FU. The horizontal axis shows frequencies in the range from 10 mHz to 10 Hz . The vertical axis is the experiment duration. The solid blue line is when the treatments were applied. The axes are the same for all spectrograms. (a) The averaged drug-response spectrograms from Esophageal patient 31. (b) The spectrogram collage from the same patient on a per well basis. The replicate number for each treatment is three or four.

3.2.5 Drug-Response Spectrograms

Although the individual well-based spectrograms were used to train the neural network, it is still valuable to construct average drug-response spectrograms by using different combinations of the well-based phenotypes. For instance, Figure 3-2a shows averages for patients with stable disease compared to patients with complete response using all well-based phenotypes (1, 2, 3 and 4). The bottom row is the difference of the resistant relative to the sensitive spectrograms. The patients with partial response for their clinical outcomes are not included in these averages. Alternatively,

averages can be constructed using only the phenotypes (1 and 4) that have high-frequency enhancements. From the neural network analysis, these phenotypes correlate most strongly with patient clinical outcomes. These restricted spectrogram averages are shown in Figure 3-2b. The removal of phenotypes 2 and 3 in the averages creates an overall blue shift for the average spectrograms. However, the differences for resistant relative to sensitive patients remain similar whether phenotypes (1, 2, 3, 4) or (1, 4) were included. This indicates that the sensitive and resistant patients had roughly equal numbers of red-shifted wells independent of the chemo resistivity of the patients, further supporting the emphasis of well-phenotypes 1 and 4 as the spectrograms that correlate best with patient outcomes.

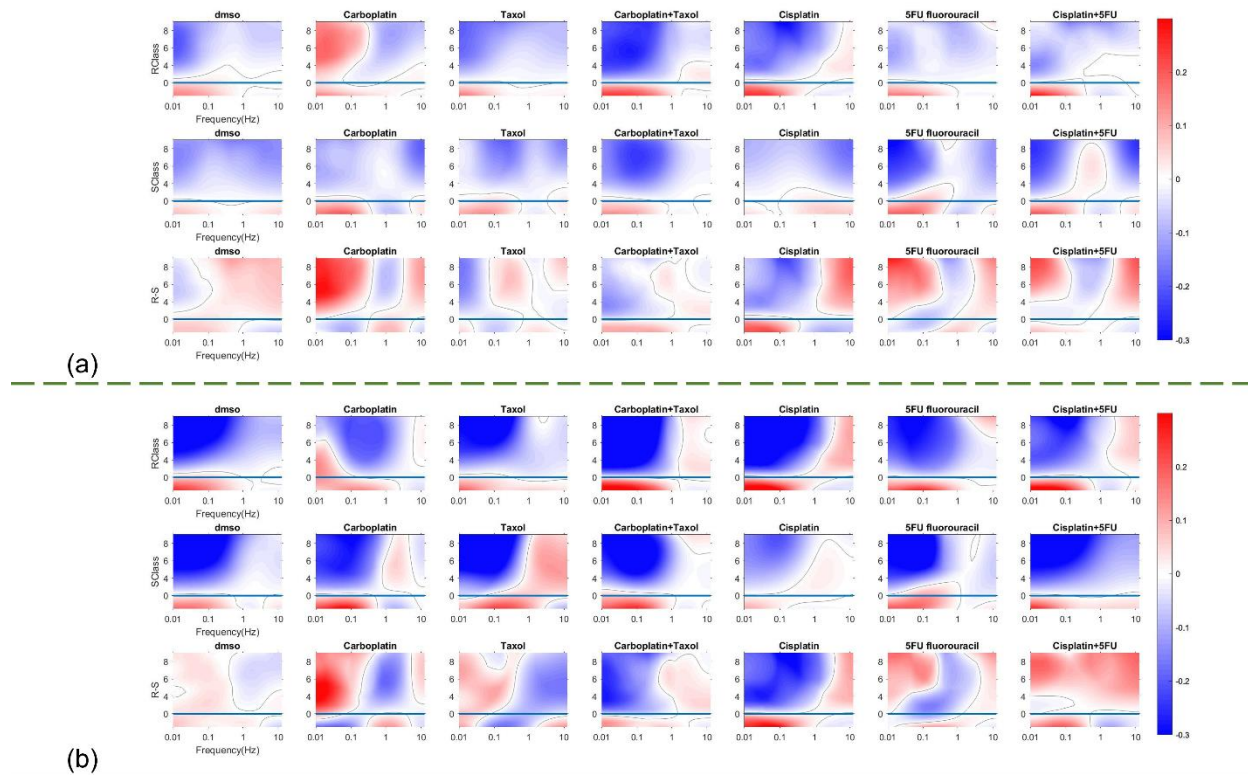


Figure 3-2 Resistant versus sensitive phenotypes. Top rows have average spectrograms of patients with stable disease. Middle rows are for patients with complete response. Bottom rows are the difference of resistant relative to sensitive. a) Spectrogram averages with all well-based phenotypes (1, 2, 3, and 4) included. b) Spectrogram averages with only high-frequency enhanced phenotypes (1 and 4) included.

3.2.6 Siamese Auto Encoder

The machine learning approach is based on dimensionality reduction that is achieved using a Siamese neural network combined with an autoencoder. A Siamese neural network is a deep neural net comparator that uses two identical deep networks with identical weights that are exposed to two data inputs. The output layer of the network has a small number of neurons, representing an information funnel to a low-dimensional latent space. A loss function is defined for pairs of inputs that seeks to minimize distance in latent space when the inputs are from the same class, and to maximize the distance when the inputs are from different classes. This type of minimization is known as locality-sensitive hashing [22, 23]. For data analysis problems with small signals in the presence of high backgrounds, this twin network approach can learn to disregard the background and to recognize the signal [24, 25]

The Siamese network is an encoder from a high-dimensional input space to a low-dimensional latent space. A decoder follows the Siamese encoder to reconstruct differences between the inputs. If the inputs are from the same class, the loss-function seeks to reconstruct a zero, whereas if the inputs are from different classes, the loss-function seeks to reconstruct the difference. When the latent dimensionality is D_{latent} , then the input to the decoder has $2 \times D_{\text{latent}}$ input neurons. Combining the locality-sensitive hashing of the Siamese neural network with the decoder and constructing the loss function to minimize both locality and reconstruction helps the network to find the most relevant information buried within the well-to-well variability.

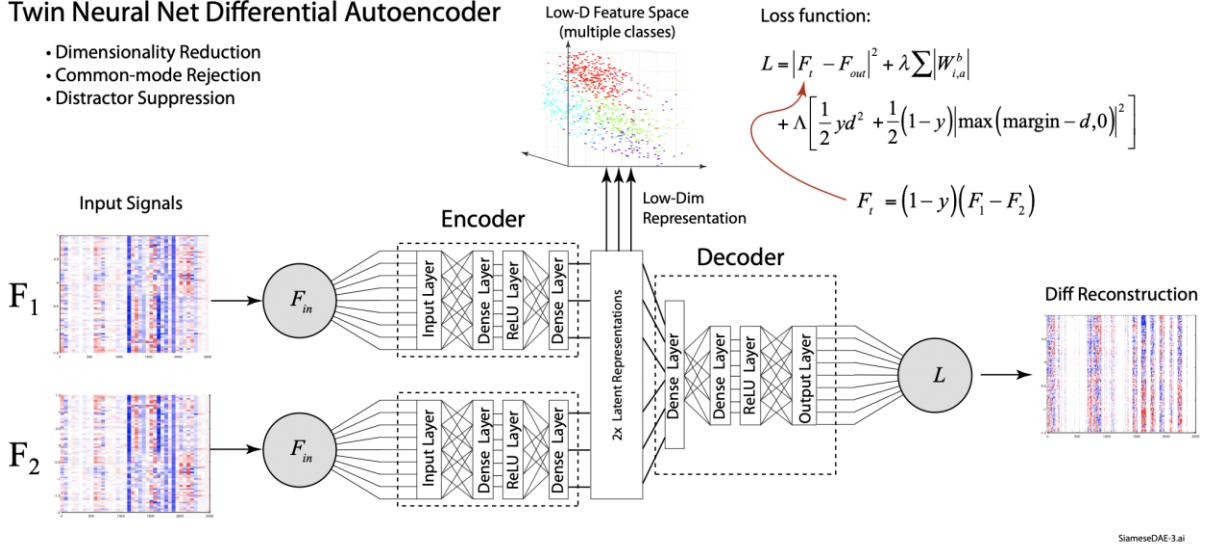


Figure 3-3 The “twin” network for dimensionality reduction consists of a single network that receives two inputs. Data structures are applied in pairs, then the contrastive loss is used to update the parameters. The network in this figure has two layers of fully-connected ReLUs that are fully connected to the output neurons.

The collective contrastive loss for the neural network training is defined as

$$\text{loss} = \frac{1}{2} yd^2 + \frac{1}{2} (1-y) |\max(\text{margin} - d, 0)|^2 + \text{I}_{\text{decode}} |F_{diff} - F_{recon}|^2 + \text{I}_1 \sum_{a,b} |W_{i,a}^b| \quad (3.1)$$

where the first two terms are the Siamese locality sensitive hashing, the third term is the mean-square error on the decoder reconstruction and the fourth term is the L1 regularization on the input weights. In the Siamese loss contribution, y is the class-agreement label ($y=1$ for similar and $y=0$ for dissimilar), and d is the Euclidean distance between the two output features of the two subnetworks

$$d = \|F_1 - F_2\|_2 \quad (3.2)$$

The *margin* parameter is used for constraint: if two images in a pair are dissimilar, then their distance should be at least equal to the margin, or a loss will be incurred. Only one of these two terms in the loss function is active for a given pair. If they are similar ($y=1$) then the algorithm minimizes their distance d . If they are dissimilar, then the algorithm causes their distance d to be

at a distance *margin* away from each other. For the decoder training, the difference function F_{diff} is simply

$$F_{\text{diff}} = (1 - y)(F_1 - F_2) \quad (3.3)$$

where F_1 and F_2 are the input feature vector pair. If the similarity index $y = 1$, then the decoder is seeking to reconstruct a zero-vector. This creates a stronger constraint than only reconstructing the difference between the inputs, because the difference between two feature vectors of the same class may be dominated by noise or distractors which should not be reconstructed as being significant. The differences among a set of input pairs and the reconstructed differences after the decoder are shown in the **Appendix. B**. The final contribution to the loss function is an L1 regularization loss on the input weights that down-weights unimportant input channels. After training, the input weights can be histogrammed to find the most relevant features in the biodynamic feature vectors. An example of a sorted set of significant features identified by the L1 regularization is shown in the **Appendix. B**.

After dimensionality reduction at the end of training, a single trained network is used to construct the latent representation of a biodynamic feature vector. These latent representations are then used as low-dimensional inputs to a multi-class classifier. In our implementation with MATLAB, the multi-class classifier is an Error Correcting Output Code (ECOC) which is a multi-class SVM. The performance of the trained ECOC model is comparable to training a softmax classifier on the latent representations.

3.3 Results

The clinical trial enrolled 28 patients who presented with esophageal adenocarcinoma at the IU School of Medicine Hospital between April 2015 and January 2020. A pinch biopsy was performed for normal diagnostic purposes of which a small volume of between 30 to 70 mm³ was placed in growth medium to maintain tissue health for up to 8 hours. The biopsy was cut into approximately 1 mm³ volume sections to yield between 16 to 32 samples that were immobilized

using poly-L lysine in a multi-well plate. Each well received carboplatin+taxol (CT) or cisplatin+5fu (CF) combination therapies, as well as their single-agent components, and the biodynamic response was monitored for up to 18 hours after application of the drug. Of the enrolled patients, 22 datasets displayed high-quality biodynamic profiles and consistent responses to treatment. The remaining 6 patients had non-representative features either due to lower data quality or to rare phenotypes (see Methods below). During subsequent data analysis, the 22 patients were used to train the Siamese neural network autoencoder using patient clinical outcomes that were obtained after chemoradiation therapy.

More than 600 well-based drug-response spectrograms were generated by the trial. These spectrograms were separated into four groups, called well-based phenotypes, that are: red-shifted, blue-shifted, mid-frequency-enhanced, and mid-frequency suppressed, depending on the dominant spectral response. The red-shifted well-based phenotype indicated biopsy samples in which the average intracellular transport slows down over the 10-hour period after the drug was applied. This decrease can reflect a decreasing metabolism and is likely to relate to a decrease in the cellular activity, and possibly sample health. Figure 3-4 (a) shows the four spectrogram phenotypes, and (b) is the similarity matrix, using a correlation metric, for the approximately 600 feature vectors in each well, grouped according to phenotype.

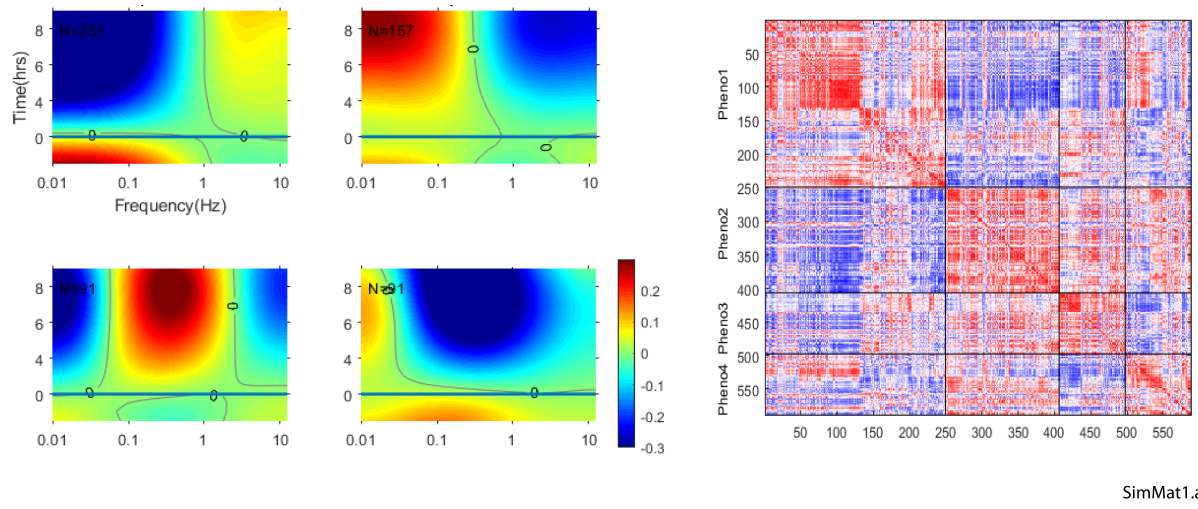


Figure 3-4 Drug-response biodynamic spectrograms for the esophageal cancer clinical trial. a) Four spectrogram phenotypes from esophageal biopsies. In this nomenclature, phenotype-1 is blue shifted, phenotype-2 is redshifted, phenotype-3 is mid-frequency enhanced, and phenotype-4 is mid-frequency suppressed. b) Similarity matrix of the feature vectors from all wells ordered by phenotype.

A key result of this work is the identification of the red-shifted phenotype (Phenotype-2) as non-indicative of patient response to treatment. When these data wells are excluded from the training set, improved correspondence of the biodynamic signatures with patient clinical outcomes is achieved. Overall network accuracies are shown in Figure 3-5a) for different phenotype subsets. In this nomenclature, phenotype-1 is blue shifted, phenotype-2 is redshifted, phenotype-3 is mid-frequency enhanced, and phenotype-4 is mid-frequency suppressed. When the two phenotypes with enhanced high frequencies (phenotypes 1 and 4) are selected, the network classification accuracy is highest. Conversely, when the two phenotypes with enhanced low-frequencies (phenotypes 2 and 3) are selected, the network accuracy is lowest. When all phenotypes (1, 2, 3 and 4) are used, the accuracy falls between the two extremes

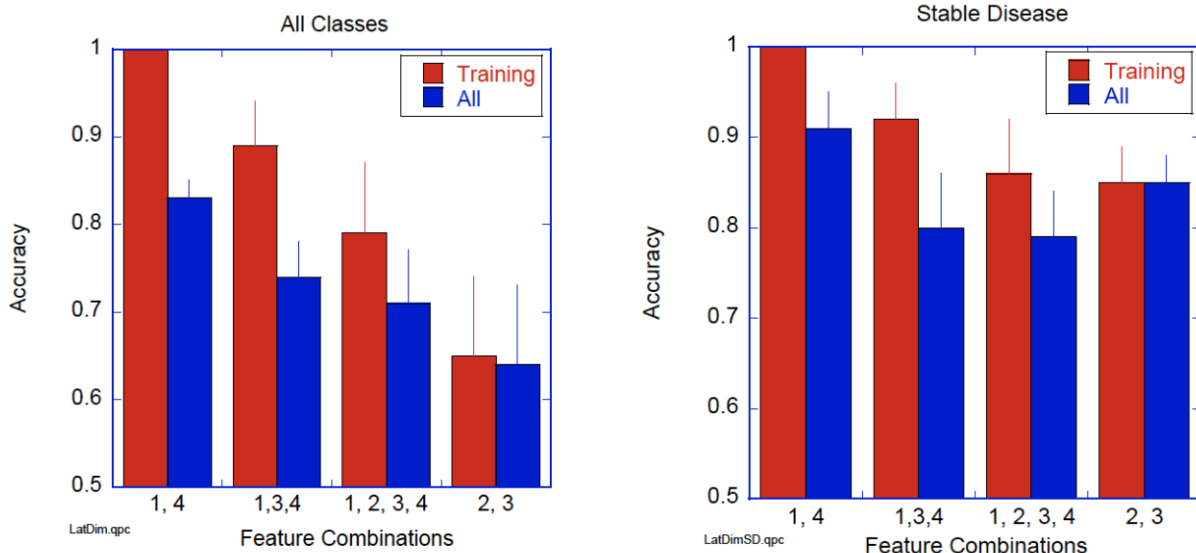


Figure 3-5 Classification accuracies for training patients and for all patients as a function of feature combinations used in the Siamese autoencoder. a) All classes. b) Stable disease versus other classes. Latent dimensionality is equal to 3.

An example of the clustering in latent space is shown in Figure 3-6. The neuron output states are shown in a) for the 22 training patients and represented in the three-dimensional latent space in b) after network training. These state vectors generate the patient clusters shown as a network in c) for the 22 cross-validated patients. Each subcluster is a complete graph with no connections to the other subclusters, showing perfect classification and similarities among the three classes of patient response. The one-hold-out cross validation of the 22 training patients as well as the 6 atypical patients is shown in d). In this single network analysis, four of the atypical

patients failed to classify correctly. Therefore, the overall accuracy of the Siamese autoencoder for this 28-patient trial predicting patient response to therapy was $24/28 = 86\%$. The positive likelihood ratio (plr) for predicting patient chemoresistance to therapy is $\text{plr} = 8 \cdot 19/9 = 17$ to 1. The negative likelihood ratio (nlr) for incorrectly predicting patient chemoresistance to therapy is $\text{nlr} = 19/(18 \cdot 9) = 1$ in 9.

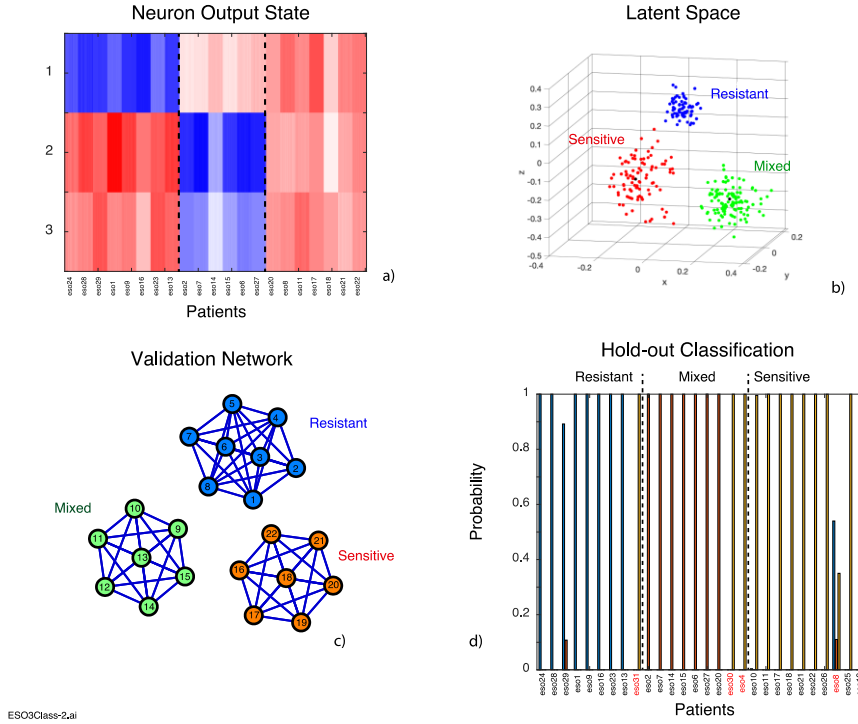


Figure 3-6 Neural network low-dimensionality latent space. a) The output states of the Twin neural network. b) Three-dimensional representation of a batch of Patient Charts plot showing strong clustering into 3 classes. c) Network graph generated from the latent-space representation. d) One-hold-out patient classification for the 22 training patients plus 6 atypical patients. The four mis-classified patient IDs are shown in red and all were from the atypical patient group.

The resulting classifier was evaluated using one-hold-out cross-validation on the training set and ensemble averaged over five independently trained networks. The 6 atypical patients were also classified by the network. The patient outcomes were scored using conventional RECIST into four conditions: stable disease (SD), moderate response, marked response, and pathological complete response (pCR). A three-class classifier combined the moderate and marked response patients into a single condition of partial response. The classification accuracies for the validation set as well as for the full trial set of patients were $100\% \pm 0\%$ and $83\% \pm 2\%$, respectively, for the three-class classifier. When identifying patients who are not likely to benefit from chemotherapy,

the partial and complete response patients are pooled. The accuracies for the validation set and the full trial in this case was $100\% \pm 0\%$ and $91\% \pm 4\%$, respectively. In the neoadjuvant setting of esophageal cancer treatment, resistant patients would go directly to surgery for surgical removal of the cancer. These results suggest that, in a prospective setting using biodynamic profiling to direct chemo-resistant patients directly to surgery, the rate of positive response (defined as partial response, full response or direct surgery) would increase from $19/28 = 68\%$ without biodynamic guidance to $25/28 = 91\%$ with biodynamic guidance in this chemo-radiation neoadjuvant setting.

3.4 Discussion

Tumor heterogeneity, both spatial and genetic, produces highly variable biodynamic data on a well-to-well basis even from a single patient. This high data diversity presents a challenge for conventional multi-variate analysis and machine learning, especially because the data can have strong nonlinearities when features are conditionally dependent on other features. This situation favors the use of deep neural networks where multiple hidden layers in a neural network learn nonlinear relationships among the input variables. Our previous work on tissue dynamics of cancer biopsies [21] used averaging approaches which suppressed the conditional dependencies. In this current work, we retain the full well-to-well variability and apply a semi-deep Siamese neural network autoencoder.

As part of data conditioning prior to input to the neural network, there was a selection of well-based phenotypes that have enhanced high frequencies (blue shifts), and the exclusion of the wells that had low-frequency enhancements (red shifts). Because tissue-dynamics spectroscopy is based on Doppler light scattering, there is an immediate interpretation of the red shift of the non-representative samples. The red shift signifies that the average intracellular activity is decreasing throughout the duration of the 10-hour assays. Lower activity is indicative of reduced metabolic efficiency that can be interpreted as an overall reduction in sample health. Conversely, blue shifts suggest that tissue is increasing its metabolic health through the duration of the assay. In simple terms, this means that the excluded wells with red-shifted samples contained samples whose overall health was declining. The subsequent analysis confirmed that the response of these tissues to the exogenous challenge of the chemotherapy drugs was not well correlated with the patient outcome. Thus, using biodynamic profiles of biopsy response to treatment with a well-based

phenotyping approach combined with deep learning improves the accuracy to assess the chemo-resistance of esophageal patients and could improve clinical outcomes in a prospective setting.

3.5 Reference

1. Ekman, S., et al., *Esophageal cancer: current and emerging therapy modalities*. Expert Review of Anticancer Therapy, 2008. **8**(9): p. 1433-1448.
2. Herskovic, A., et al., *COMBINED CHEMOTHERAPY AND RADIOTHERAPY COMPARED WITH RADIOTHERAPY ALONE IN PATIENTS WITH CANCER OF THE ESOPHAGUS*. New England Journal of Medicine, 1992. **326**(24): p. 1593-1598.
3. Shapiro, J., et al., *Neoadjuvant chemoradiotherapy plus surgery versus surgery alone for oesophageal or junctional cancer (CROSS): long-term results of a randomised controlled trial*. Lancet Oncology, 2015. **16**(9): p. 1090-1098.
4. Mamdani, H., K. Kesler, and S. Jalal, *Advances and Controversies in the Management of Locally Advanced Gastro-esophageal Adenocarcinoma*. J Clin Gastroenterol Treat, 2016. **2**(1): p. 010.
5. Napier, K.J., M. Scheerer, and S. Misra, *Esophageal cancer: A Review of epidemiology, pathogenesis, staging workup and treatment modalities*. World Journal of Gastrointestinal Oncology, 2014. **6**(5): p. 112-120.
6. Le Bras, G.F., et al., *Esophageal cancer: The latest on chemoprevention and state of the art therapies*. Pharmacological Research, 2016. **113**: p. 236-244.
7. Meguid, R.A., et al., *Recurrence after neoadjuvant chemoradiation and surgery for esophageal cancer: Does the pattern of recurrence differ for patients with complete response and those with partial or no response?* Journal of Thoracic and Cardiovascular Surgery, 2009. **138**(6): p. 1309-1317.
8. Ling, Z.Q., et al., *Heterogeneity of chemosensitivity in esophageal cancer using ATP-tumor chemosensitivity assay*. Acta Pharmacologica Sinica, 2012. **33**(3): p. 401-406.

9. Cree, I.A., *Chemosensitivity and chemoresistance testing in ovarian cancer*. Current opinion in obstetrics & gynecology, 2009. **21**(1): p. 39-43.
10. Neubauer, H., et al., *Predicting resistance to platinum-containing chemotherapy with the ATP tumor chemosensitivity assay in primary ovarian cancer*. Anticancer research, 2008. **28**(2A): p. 949-55.
11. Herzog, T.J., et al., *Chemosensitivity testing with ChemoFx and overall survival in primary ovarian cancer*. American journal of obstetrics and gynecology, 2010. **203**(1): p. 68 e1-6.
12. Markman, M., *Counterpoint: chemosensitivity assays for recurrent ovarian cancer*. Journal of the National Comprehensive Cancer Network : JNCCN, 2011. **9**(1): p. 121-4.
13. Watkins, J.M., et al., *Toxicity, Response Rates and Survival Outcomes of Induction Cisplatin and Irinotecan Followed by Concurrent Cisplatin, Irinotecan and Radiotherapy for Locally Advanced Esophageal Cancer*. Japanese Journal of Clinical Oncology, 2011. **41**(3): p. 334-342.
14. Marusyk, A. and K. Polyak, *Tumor heterogeneity: Causes and consequences*. Biochimica Et Biophysica Acta-Reviews on Cancer, 2010. **1805**(1): p. 105-117.
15. Ma, Y., et al., *An integrative genomic and proteomic approach to chemosensitivity prediction*. International Journal of Oncology, 2009. **34**(1): p. 107-115.
16. Yu, P., et al., *Imaging of tumor necroses using full-frame optical coherence imaging*. Coherence Domain Optical Methods and Optical Coherence Tomography in Biomedicine Vii, 2003. **4956**: p. 34-41.
17. Yamaguchi, I. and T. Zhang, *Phase-shifting digital holography*. Optics Letters, 1997. **22**(16): p. 1268-1270.
18. Cuche, E., F. Bevilacqua, and C. Depeursinge, *Digital holography for quantitative phase-contrast imaging*. Optics Letters, 1999. **24**(5): p. 291-293.

19. Li, Z., et al., *Doppler fluctuation spectroscopy of intracellular dynamics in living tissue*. Journal of the Optical Society of America a-Optics Image Science and Vision, 2019. **36**(4): p. 665-677.
20. Choi, H., et al., *Biodynamic digital holography of chemoresistance in a pre-clinical trial of canine B-cell lymphoma*. Biomedical Optics Express, 2018. **9**(5): p. 2214-2228.
21. Li, Z., et al., *Intracellular optical doppler phenotypes of chemosensitivity in human epithelial ovarian cancer*. Scientific Reports, 2020. **10**(1): p. 17354.
22. Hu, W.M., et al., *Deep Constrained Siamese Hash Coding Network and Load-Balanced Locality-Sensitive Hashing for Near Duplicate Image Detection*. Ieee Transactions on Image Processing, 2018. **27**(9): p. 4452-4464.
23. Zhao, K., et al. *Locality Preserving Hashing*. in *28th AAAI Conference on Artificial Intelligence*. 2014. Quebec City, CANADA.
24. Zheng, L.L., et al., *Siamese multi-layer perceptrons for dimensionality reduction and face identification*. Multimedia Tools and Applications, 2016. **75**(9): p. 5055-5073.
25. He, H.Q., et al., *Matching of Remote Sensing Images with Complex Background Variations via Siamese Convolutional Neural Network*. Remote Sensing, 2018. **10**(2).
26. Metzler, R. and J. Klafter, *The random walk's guide to anomalous diffusion: a fractional dynamics approach*. Physics Reports-Review Section Of Physics Letters, 2000. **339**(1): p. 1-77.
27. Choi, H., et al., *Phase-Sensitive Intracellular Doppler Fluctuation Spectroscopy*. Physical Review Applied, 2021. **15**(2).

CHAPTER 4. BIODYNAMIC MONITORING OF BACTERIAL INVASION OF LIVING TISSUE

Bacterial infection involves internalization of pathogenic bacteria into host cells. There are various internalization mechanisms, and it can vary within the same species for different strains. The goal of this project is to infect tumor spheroids of DLD-1 colon cancer cell lines with a range of bacteria. The Doppler power spectrum of DLD-1 is stable, and DLD-1 can be used as a standard specimen for an assay with different challenges. In the data format, we use a 4-loop baseline measurement and a 22-loop post-dose measurement after adding a bacteria-containing medium into a DLD-1 well.

4.1 Introduction

4.1.1 Introduction to Bacteria

Bacteria are the simplest lifeform on Earth. Their biological features are well known and have been actively studied. However, their physical aspects such as swarming or chemotaxis mechanisms are not as clearly understood. Current methods to measure bacterial motility use soft agar assays and optical imaging. Soft agar assays usually require many cell cycles to measure a meaningful colony diameter to estimate bacterial motility which limits measurements of real-time motility. Also, optical imaging may have a limited field of view (FOV), and the data acquisition on bacterial motility would be localized. The advantages of BDI compared to conventional motility measurement methods are: i) coherence-gating and large beam diameter enable the collection of signal from a large number of specimens (several millions of bacteria), ii) quasi-real time measurement by a short data acquisition time, and iii) controlling chemical composition of liquid medium during measurement. The measurements previously conducted by BDI tested nutrient-shock and antibiotic-driven motility using high-cell-density bacterial pellets [1].

Bacteria have flagella which have a dominant role on bacteria motility. A flagella's protein composition and motility generation mechanism vary between different species, but bacteria generally use flagella for propulsion.

Rapid environmental changes can cause swarming migration within a short time. The purpose of migration is the search for nutrients for proliferation or to avoid toxicity. During bacterial migration, prominent Doppler shifts can occur in a light-scatter power spectrum. A single measurement takes 2 minutes which is about 1/10 of bacterial cell cycle. Therefore, the motility effect on the power spectra represent motilities by cellular migrations not by motilities induced by replication.

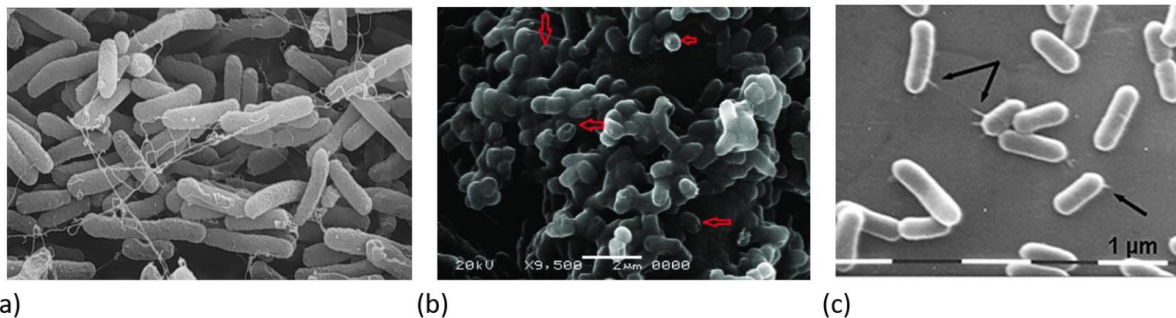


Figure 4-1 SEM pictures of (a) *E. coli* [2](b) *S. enterica* [3]and (c) *L. monocytogenes* [4].

The dynamic and physical characteristics are shown in the table below.

Table 5 Bacterial strains and corresponding physical characteristics

Strain	<i>E. coli</i>	<i>L. monocytogenes</i>	<i>S. enterica</i>
Speed ($\mu\text{m/s}$)	$20^{[13]}$	$6^{[14]}$	$20^{[15]}$
Width (μm)	$0.25^{[16]}$	$0.7\sim1.5^{[17]}$	$0.4\sim0.5^{[18]}$
Length (μm)	1~2	2.0~5.0	1~2

4.1.2 Infection Assay of Pathogenic Bacteria within a Cell Line

Immortalized cancer cell lines are a common and versatile resource as three-dimensional tissue surrogates to study intracellular dynamics in microenvironments that simulate natural living tissues [1-4]. These tissue constructs have characteristic biodynamic spectra that span three orders of magnitude in Doppler frequencies and tend to have characteristic frequencies, known as knee frequencies, that encompass a single broad spectral feature. Different cell lines can display different knee frequencies depending on how cohesive the tissue is [13]. To investigate infection

phenotypes, DLD-1 (adenocarcinoma cancer cell line) were used. All bacterial strains in this study are foodborne pathogens and they actively engage epithelial cells. DLD-1 is a cluster of epithelial cells and has a 3D structure that is expected to represent practical infection processes.

Bacterial infection of living tissue occurs through several different mechanisms. For instance, *L. monocytogenes* actively penetrate the cell membrane [5], while *S. enterica* hijack the actin processes of the cellular membrane to allow them to be internalized [6]. *E. coli*, in contrast, adheres to the exterior of the cell [7]. These different mechanisms may be expected to alter the underlying cellular dynamics of the tissue in different ways that may be related to the characteristics of the bacteria. DLD-1 was inoculated by various strains and the infection phenotypes of the bacterial strains were studied.

4.2 Sample preparation and Experiment Set-Up

4.2.1 Common-path System

The common-path interferometric configuration was developed for reflection mode operation as shown in Figure 4-2. A long-coherence LaserMax red laser with a center wavelength at 690 nm is used as the light source. The probe beam illuminates the target at an oblique angle of 34 degrees relative to the backscatter direction. Intracellular transport is isotropic relative to the direction of the incoming wave vector, and the average Doppler frequency shift is zero. The knee frequency of the fluctuation spectrum represents the root-mean-squared Doppler frequency shift within the ensemble of scatterers, and the maximum fluctuation bandwidth is at the backscattering angle of 180 deg. We use the slight angled illumination on the sample to eliminate a beam splitter and increase the intensity of the collected light. A 10 \times microscope objective lens with a long working distance of 30.5 mm and a numerical aperture of 0.26 is employed to collect the light scattered from the target. After relaying the light by lenses L1 and L2 at a magnification of 3:2, a holographic transmission grating (G) at the first Fourier plane (FP1) splits the light into identical +1 and -1 diffraction orders. The phase grating (HOLO/OR LTD) has a 73% transmission efficiency (with a partially quenched zero-order) and a beam separation angle of 2.01 deg. The light is transformed by lens L3 to a second image plane (IP2) where only the first orders pass through the spatial filter (SF). The other diffraction orders are blocked by the SF which consists of a small reference aperture of 0.6 mm diameter and a large object aperture of 3.0 mm in diameter.

The two apertures are separated laterally by 5.3 mm. The +1 diffractive order passing through the large aperture is the object wave, whereas the -1 diffraction order passing through the small aperture produces the reference wave. An optical Fourier transform is performed by the Fourier lens L4, and the reference and object waves share the same path to create stable interference fringes at the second Fourier plane (FP2). The hologram with a size of 800 by 800 pixels is recorded by a CMOS camera (Basler acA1920-155um) with 12-bit depth at 25 frames per second and an exposure time of 10ms. Direct images are captured at the image plane (IP) and IP2. The reconstruction image is compared with direct images from the image planes.

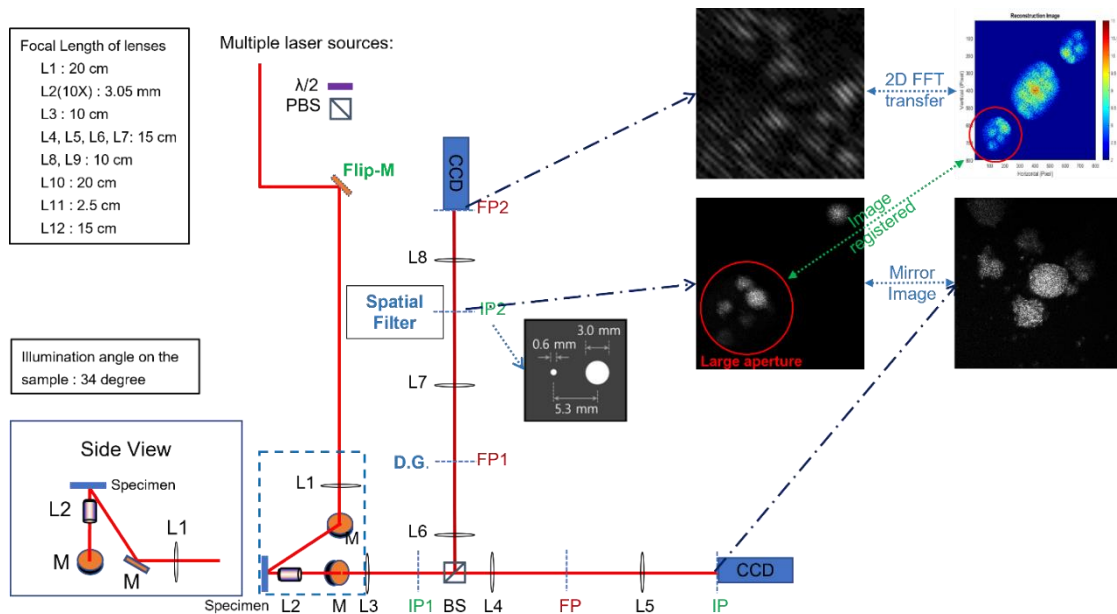


Figure 4-2 Common-path System. The probe beam illuminates the target at an oblique angle of 34 degrees relative to the backscatter direction. There is a spatial filter with a big aperture and a small aperture in IP2. Digital holograms are captured by the camera in FP2. Direct images are captured in IP and IP2. The reconstruction image is compared with direct images from the image planes.

The scattered wave field magnified by the microscope objective and the lens L3 is denoted as $U(x_1, y_1)$ at the image plane IP1. For an ideal binary phase grating with a duty cycle of 0.5 and a π -phase depth, the transmission function of the grating is given by

$$g(x'_1, y'_1) = \sum_{m=-\infty}^{+\infty} \frac{\sin(m\pi/2)}{m\pi/2} \exp\left[j \frac{2\pi mx'_1}{\Lambda}\right] \quad (4.1)$$

where m is the diffraction order and Λ is the period of the grating. The diffraction efficiency vanishes for all even values of m , and has a maximum of about 40.5% for each of the +1 and -1

orders. In the 4f imaging system of the lenses L6 and L7, the wave $U_a(x_2, y_2)$ after the spatial filter at IP2 is given by

$$U_a(x_2, y_2) \approx U(-x_2 + x_0, -y_2) \text{circ}[r'_+/R_o] + U(-x_2 - x_0, -y_2) \text{circ}[r'_-/R_r] \quad (4.2)$$

where $x_0 = \lambda f_2 / \Lambda$, λ is the wavelength, $r'_+ = \sqrt{(x_2 - x_0)^2 + y_2^2}$, $r'_- = \sqrt{(x_2 + x_0)^2 + y_2^2}$, and R_o and R_r are the radii of the object and reference aperture which are centered at $+x_0$ and $-x_0$ in the x-direction from the center, respectively.

Lens L8 performs the Fourier transform, and the reference wave $U_r(x'_2, y'_2)$ and object wave $U_o(x'_2, y'_2)$ at the camera plane FP2 can be expressed as

$$U_o(x'_2, y'_2) \approx \exp\left(j \frac{2\pi x_0 x'_2}{\lambda f_1}\right) FT[U] \otimes J_{inc}\left(\frac{R_o \rho'}{\lambda f_1}\right), \quad (4.3)$$

$$U_r(x'_2, y'_2) \approx \exp\left(-j \frac{2\pi x_0 x'_2}{\lambda f_1}\right) FT[U] \otimes J_{inc}\left(\frac{R_r \rho'}{\lambda f_1}\right), \quad (4.4)$$

where $FT[U]$ is the Fourier transform of U , $J_{inc}(x) = J_1(x)/x$ in which $J_1(x)$ is a Bessel function of the first kind, \otimes denotes convolution, and $\rho' = \sqrt{(x'_2)^2 + (y'_2)^2}$. The reconstruction of the hologram is performed by an inverse Fourier transform and consists of a zero-order term and two conjugate diffraction terms. One diffraction term is reconstructed at $(2x_0, 0)$ as

$$\begin{aligned} & FT^{-1} \left\langle \exp\left(j \frac{4\pi x_0 x'_2}{\lambda f_1}\right) \left\{ FT \left[U \left(\frac{-x'_2}{\lambda f_1}, \frac{-y'_2}{\lambda f_1} \right) \right] \otimes J_{inc}\left(\frac{R_r \rho'}{\lambda f_1}\right) \right\}^* \right. \\ & \quad \left. \left\{ FT \left[U \left(\frac{-x'_2}{\lambda f_1}, \frac{-y'_2}{\lambda f_1} \right) \right] \otimes J_{inc}\left(\frac{R_o \rho'}{\lambda f_1}\right) \right\} \right\rangle. \end{aligned} \quad (4.5)$$

4.2.2 Specimen Preparation

The DLD-1 cell stock was purchased from American Type Culture Collection (ATCC, Manassas VA) and cells were grown in RPMI-1640 medium containing 25 mm HEPES buffer (Gibco) supplemented with 10% fetal bovine serum (Atlanta Biologicals) and 100 U penicillin/ml-100 µg/ml streptomycin (Gibco). DLD-1 cell growth is highly reproducible and can generate large replicate numbers for multi-well plate assays.

Three types of bacteria are used for this study: *Escherichia coli*, *Salmonella enterica* serovar Enteritidis phage type (PT) 21 and *Listeria monocytogenes*. The *E. coli* strain used in this study is the genetically engineered O157:H7 strain for which the Shiga toxin gene has been removed, and green fluorescent protein (GFP) and ampicillin resistance genes have been added [1]. The *S. enterica* and *L. monocytogenes* strains are natural phenotypes, which can infect mammalian cells and proliferate.

E. coli and *S. enterica* were cultured in LB (Lysogeny-broth) medium for 24 hours at 37°C in the incubator shaker with the speed of 150 revolutions per minute. *L. monocytogenes* were cultured in BHI (Brain Heart infusion broth) medium for 24-30 hours at 37°C in the incubator shaker with the speed of 150 revolutions per minute. LB medium is a solution of 1% tryptone, 0.5% bacto-yeast extract, 1% sodium chloride and 0.1% glucose. BHI medium is a solution of 5g/L beef heart (infusion from 250g), 12.5 g/L calf brains (infusion from 200g), 2.5 g/L disodium hydrogen phosphate, 2 g/L D (+)- glucose, 10 g/L peptone and 5 g/L sodium chloride. After 24-30 hours, bacterial concentrations reach 10^8 CFU/ml.

Sixteen samples from DLD-1 micro-clusters were placed in a 96-well plate for each experiment. There are two different experimental designs in this study: bacteria concentration design and static control design. For the first kind, there are four or five treatments applied to DLD-1 micro clusters: negative control medium (PBS buffer), bacteria medium with concentration of 10^3 CFU/ml, 10^4 CFU/ml, 10^5 CFU/ml, and 10^6 CFU/ml depending on the needs of study; As for the second type of design, static control stands for pretreating with 10% neutral buffered formalin (NBF) before BDI experiment to deactivate the cells. So, there are four different groups: static negative control group (NBF+ PBS), static bacterial group (NBF+ bacteria), living negative control (PBS), living bacterial group (bacteria).

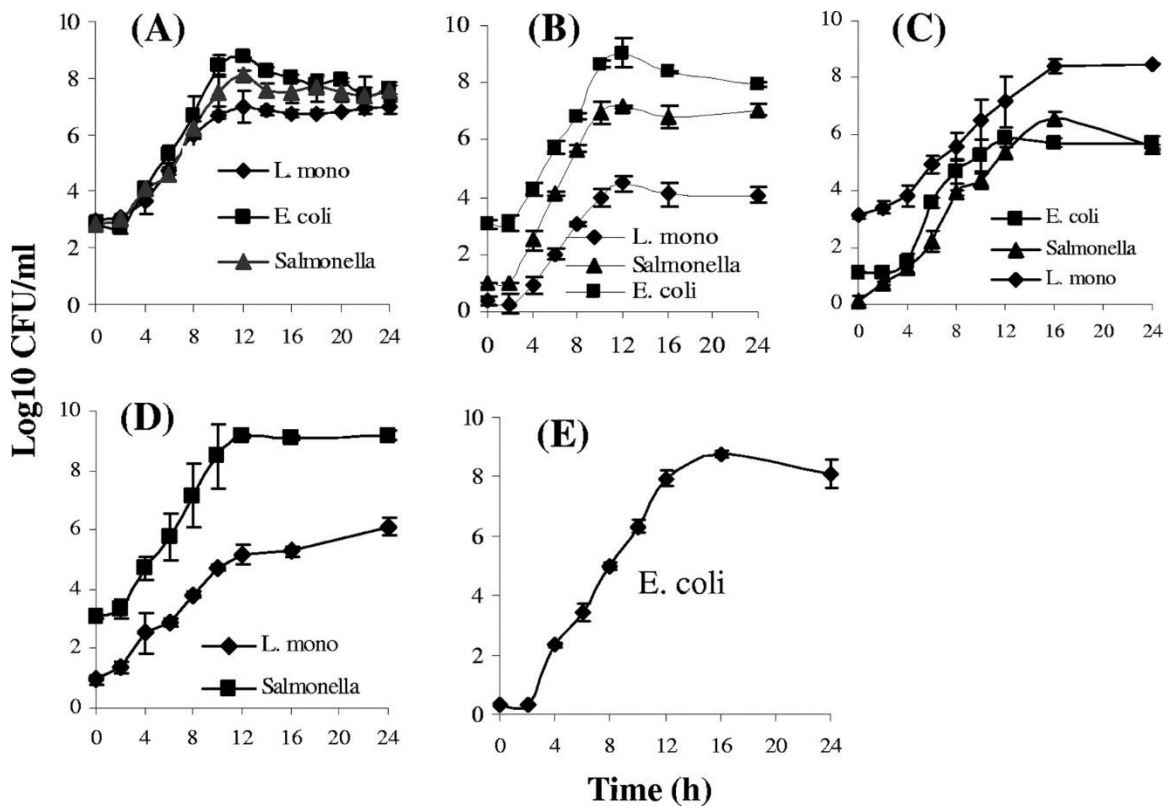


Figure 4-3 (A to D) Growth curves for the three pathogens *Salmonella* serovar Enteritidis, *E. coli* O157:H7, and *L. monocytogenes* (*L. mono*) mixed at various ratios in SEL: *Salmonella* CFU/*E. coli* CFU/*L. monocytogenes* culture ratios, 1:1:1 (A), 10:1,000:1 (B), and 1:10:1,000 (C), and *Salmonella* monocyte-genes culture ratio, 1,000:10 (D) [14].

Experiments consisted of 16-well measurements on a 96-well plate. Each well contained a single DLD-1 spheroid and was filled with 250 μ l RPMI 1640 growth medium. DLD-1 spheroids were immobilized on the bottom of the wells. To infect the spheroids, the DLD-1 samples were exposed to the diluted bacteria medium allowing the bacteria to interact with the cells directly. Before applying bacteria, 4 baseline measurements were made over 2 hours. After the baseline measurement, 100 μ l of the diluted bacterial medium was pipetted into the wells. Each well was monitored repeatedly by BDI for more than 22 hours to detect interactions between bacteria and DLD-1 cells. We also grow the treatment culture into a LB agar plate before and after BDI experiment to confirm the initial and final concentration of bacteria inside each well. The bacteria inside the culture plate usually become visible after 24 hours (48 hours for *L. monocytogenes*). The workflow of preparations for the specimens is shown in Figure 4-4.

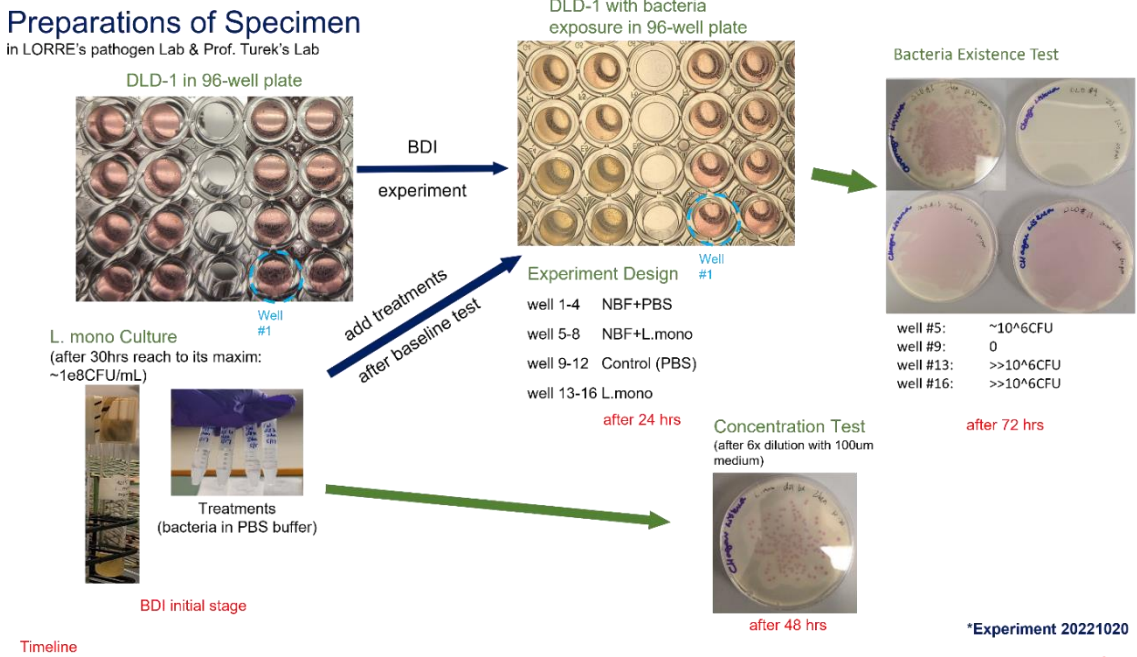


Figure 4-4 Workflow for specimen preparations. Before applying bacteria, 4 baseline measurements were made over 2 hours. After the baseline measurement, 100 μ l of the diluted bacterial medium was pipetted into the wells. Each well was monitored repeatedly by BDI for more than 22 hours to detect interactions between bacteria and DLD-1 cells. We also grow the treatment culture into a LB agar plate before and after the BDI experiment to confirm the initial and final concentrations of bacteria inside each well. The bacteria inside the culture plate usually become visible after 24 hours (48 hours for *L. monocytogenes*).

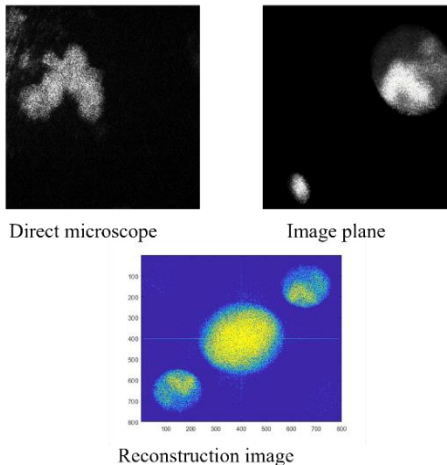
4.3 BDI Results and Analysis

4.3.1 OCI results and data quality control

Figure 4-5 shows a OCI experimental collage for bacterial infected DLD-1 cells. This data is collected from well #6 of experiment 22020517 (*S. enterica* infection experiment). There is a significant intensity increase in the late measurements caused by the cell infection from bacteria. Figure 4-6 gives a contrasting OCI experimental collage for non-bacterial infected DLD-1 cells. This data is collected from well #4 of experiment 22020517 (*S. enterica* infection experiment). There is no significant intensity change detected in the late-loop measurements, which indicates the cell is healthy during the whole monitoring period giving high confidence on the OCI base.

BDI Experiments (Bacteria group) in Physics Lab

One sample from *S. enterica* group
(BIC: 1e3CFU/ml)



*BIC: bacteria initial concentration

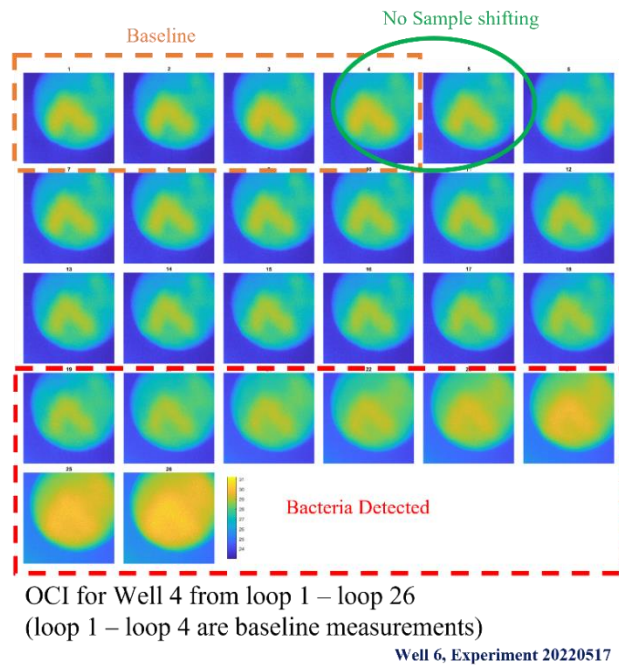


Figure 4-5 OCI experimental collage for bacterial infected DLD-1 cells. These data are collected from well #4 of experiment 22020517 *S. enterica* infection. There is a significant intensity increase in the late-loop measurements, which indicates the cell infection from bacteria.

BDI Experiments (Control group) in Physics Lab

One sample from control group (PBS buffer)

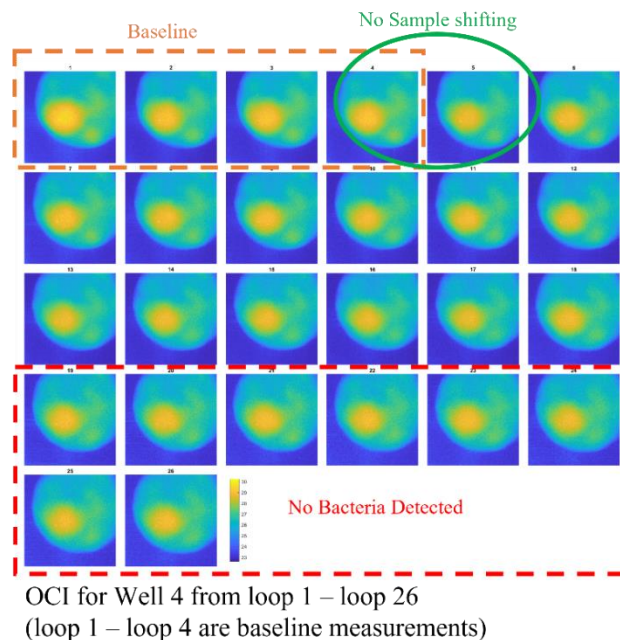
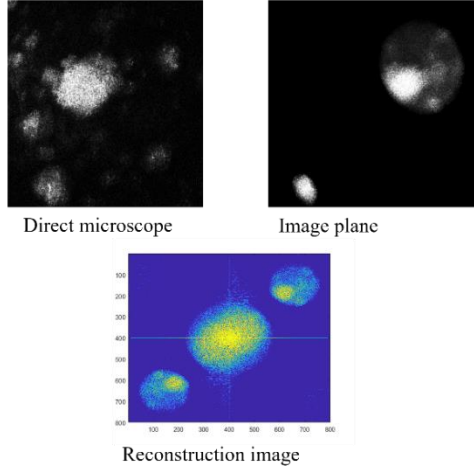


Figure 4-6 OCI experiment collage for non-bacterial infected DLD-1 cells. These data are collected from well #4 of experiment 20220517 *S. enterica* infection. There is no significant intensity change detected in the late-loop measurements, which indicates the cell is healthy during the entire monitoring period.

4.3.2 Fingerprints of Processes from Bacterial Invasion of Living Tissue

The fingerprints generated by TDS have two main formats: power spectra and power spectrograms. We can evaluate the quality of one BDI experiment by looking at the shape of the power spectrum since it provides the spectrum-related precondition biomarkers such as knee frequency, mid-frequency slope and Nyquist floor. Those biomarkers are from curve fitting of a Lorentzian function. On the other hand, a power spectrogram captures the map of power density change in frequency-time format. Red stands for enhancement of power density while blue stands for suppression of power density.

Figure 4-7 shows the fingerprints of the process from *E. coli* invading DLD-1 micro-clusters. There are seven groups in this series of experiment: negative control group (PBS buffer), *E. coli* with concentration of 10 CFU/ml, *E. coli* with concentration of 10^2 CFU/ml, *E. coli* with concentration of 10^3 CFU/ml, *E. coli* with concentration of 10^4 CFU/ml, *E. coli* with concentration of 10^5 CFU/ml, and *E. coli* with concentration of 10^6 CFU/ml. For the negative control group,

which applies only PBS buffer after the baseline measurement, the spectrogram is quite stable, and no significant effect has been detected by BDI. However, a significant power density change is observed for *E. coli* growing to a certain concentration, in this case roughly close to 10^6 CFU/ml. In the high frequency domain, power density is enhanced by more than 200%, while there is deep suppression in the mid frequency domain. Recall that the mechanism of *E. coli* invading cells is by attaching to the surface of cells to compete with the cells for nutrients instead of penetrating inside. So this significant change is possibly caused by the multiple scattering of the large amount of *E. coli*.

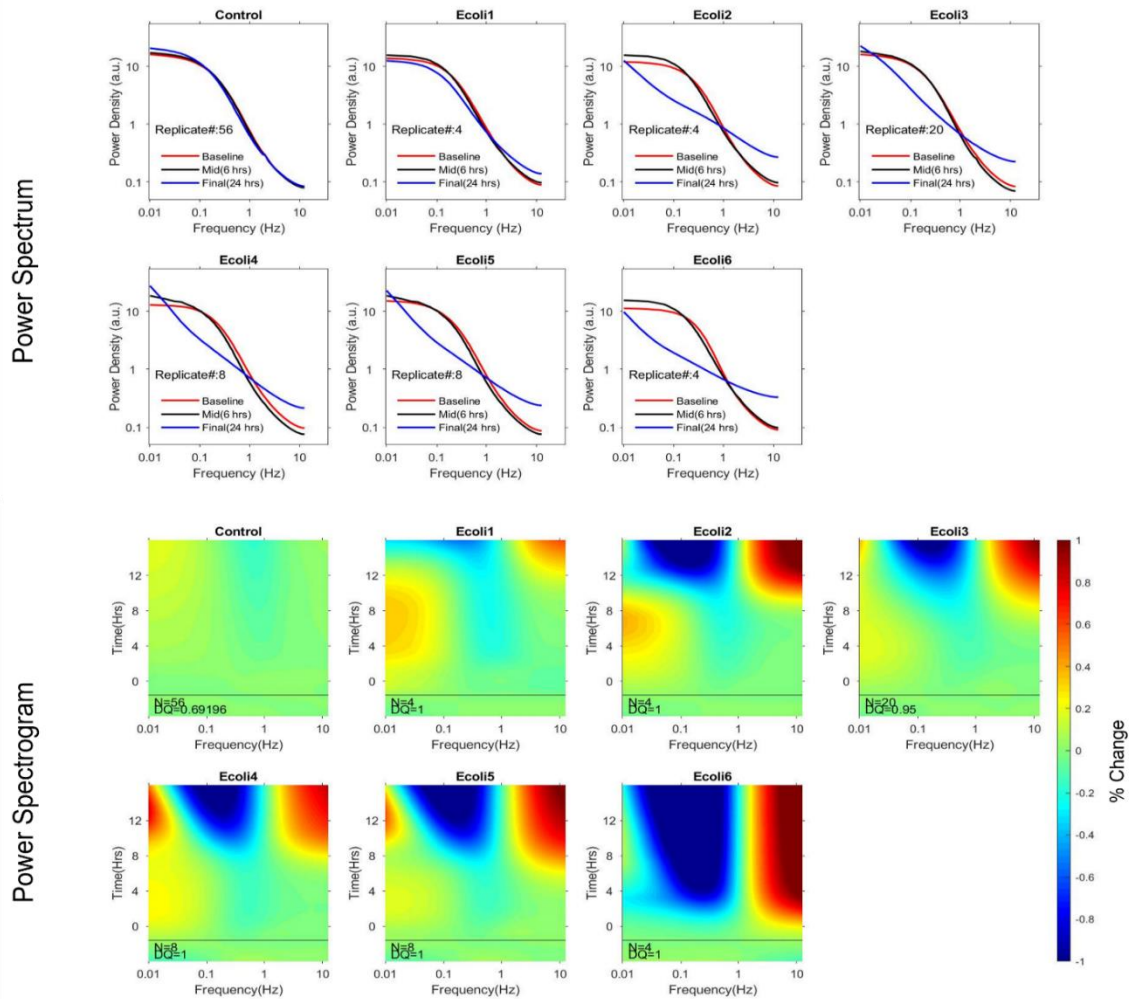


Figure 4-7 BDI fingerprints for *E. coli* invasion of living tissue. There are seven groups in this series of experiment: negative control group (PBS buffer), *E. coli* with concentration of 10 CFU/ml, *E. coli* with concentration of 10^2 CFU/ml, *E. coli* with concentration of 10^3 CFU/ml, *E. coli* with concentration of 10^4 CFU/ml, *E. coli* with concentration of 10^5 CFU/ml, and *E. coli* with concentration of 10^6 CFU/ml.

Figure 4-8 gives the BDI fingerprints for *S. enterica* invasion of living tissue. There are four groups in this series of experiment: negative control group (PBS buffer), *S. enterica* with concentration of 10^3 CFU/ml, *S. enterica* with concentration of 10^4 CFU/ml, *S. enterica* with concentration of 10^5 CFU/ml. The negative control group is also stable as the previous study of *E. coli*. Large effects have also been detected after *S. enterica* grows to a certain concentration, in this case roughly close to 10^6 CFU/ml. But there is a difference between the *S. enterica* series of BDI experiment and the *E. coli* series. A peak of power density change is observed in both mid frequency and high frequency for *S. enterica* series of BDI experiment while no peak occurred in *E. coli* series of BDI experiment. This will be discussed later (in Chapter 4.3.3) with a better view of the format.

Power Spectrum

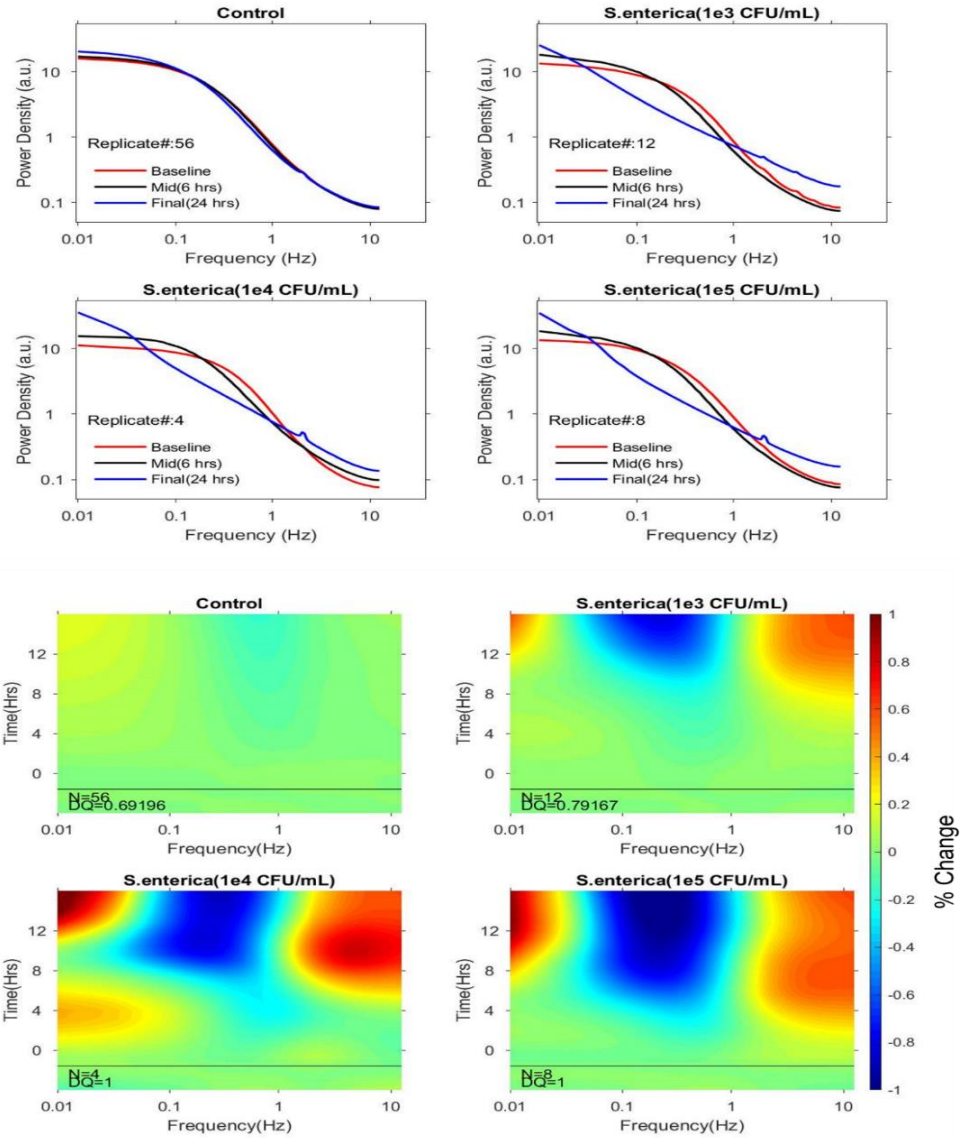


Figure 4-8 BDI fingerprints for *S. enterica* invasion of living tissue. There are four groups in this series of experiment: negative control group (PBS buffer), *S. enterica* with concentration of 10^3 CFU/ml, *S. enterica* with concentration of 10^4 CFU/ml, and *S. enterica* with concentration of 10^5 CFU/ml.

4.3.3 Doppler Spectral Shift (DSS)

Doppler spectral shift analysis is a novel analysis in the TDS technique, which tracks the change of Doppler power spectral density at a certain frequency. In this study, we divided our

frequency area into three domains: low frequency domain (less than 0.01Hz), mid frequency domain (around 0.1 Hz) and high frequency domain (higher than 1 Hz).

Figure 4-9 Doppler Spectral Shift for *E. coli* (a-c) and *S. enterica* (d-f) invasion of living tissue at low (0.01Hz), mid (0.1Hz), high frequency(>1Hz).shows the Doppler spectral shift for both *E. coli* (a-c) and *S. enterica* (d-f) invasion of living tissue at low (0.01Hz), mid (0.1Hz), high frequency(>1Hz). The low frequency-domain is primarily membrane motion. It can also be affected by mechanical vibration of the experiment and the temperature control. In short, it is hard to interpret the biological process in the low-frequency domain.

In the mid-frequency and high-frequency domain, the Doppler spectral density shift is mainly affected by organelle transport, vesicle movement and bacterial swarming. At this frequency, a difference between *E. coli* and *S. enterica* invasion of living tissue is observed. Figure 4-9 Doppler Spectral Shift for *E. coli* (a-c) and *S. enterica* (d-f) invasion of living tissue at low (0.01Hz), mid (0.1Hz), high frequency(>1Hz).shows the Doppler spectral shift for *E. coli* (a-c) and *S. enterica* (d-f) invasion of living tissue at low (0.01Hz), mid (0.1Hz), high frequency(>1Hz). Parts b) and c) show the DSS of *E. coli* series of invasion in the mid-frequency and high frequency domain. Both depend on concentration. All curves would finally reach to their maximum value after the bacteria grows into a saturation condition ($\sim 10^8$ CFU/ml). Figure 4-9 Doppler Spectral Shift for *E. coli* (a-c) and *S. enterica* (d-f) invasion of living tissue at low (0.01Hz), mid (0.1Hz), high frequency(>1Hz).e) and f) shows the DSS of *S. enterica* series of invasion in the mid-frequency and high frequency domain. Surprisingly, the DSS curves from *S. enterica* series are not like the DSS curves from *E. coli* series. A turning point occurs during the middle of the test period in the mid-frequency domain and a peak is observed in

the high-frequency domain, which strongly suggests that there are different dominant processes happening during the bacterial infection.

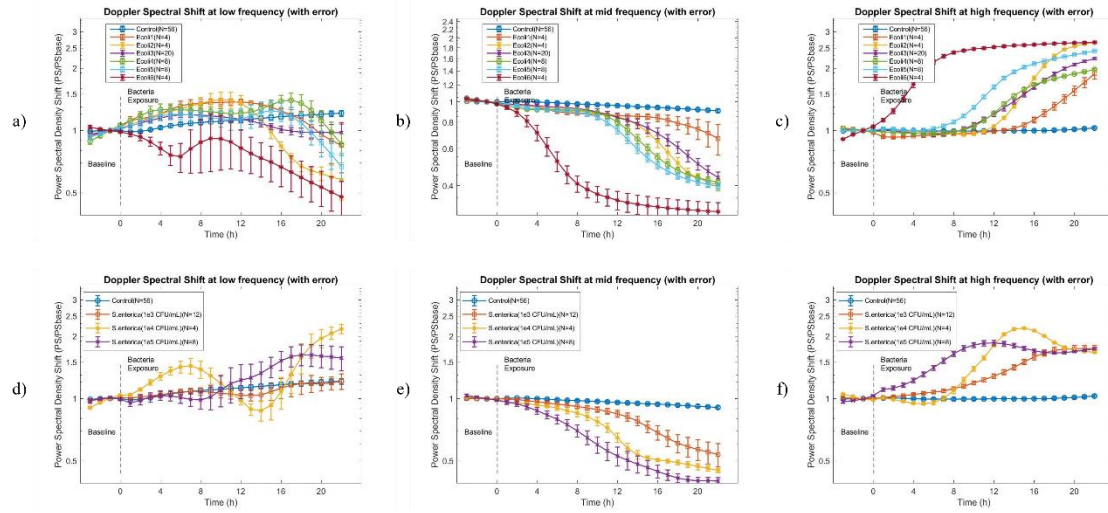


Figure 4-9 Doppler Spectral Shift for *E. coli* (a-c) and *S. enterica* (d-f) invasion of living tissue at low (0.01Hz), mid (0.1Hz), high frequency(>1Hz).

4.3.4 Doppler Knee Frequency, Mid Frequency Slope Parameter and Nyquist Floor Analysis

This section investigates biomarkers including knee frequency, mid-frequency slope and Nyquist floor generated by curve fitting of a Lorentzian function based on our power spectrum. They also help to clarify the different processes happening during different types of bacterial infection of living tissue.

Figure 4-10 shows the Doppler knee frequency shift among a) *E. coli* invasion, b) *S. enterica* invasion and c) *L. monocytogenes* invasion. The typical knee frequency for a healthy DLD-1 cell is around 0.3 Hz. When the Knee Frequency drops to zero, it reflects the unhealthy condition for DLD-1 cells. Only at later times, the knee frequency drop is observed in *E. coli* series invasion cases compared with *S. enterica* and *L. monocytogenes* invasion under the same initial bacterial infection concentration, which helps to explain that *E. coli* is competing with the living cells instead of infecting them.

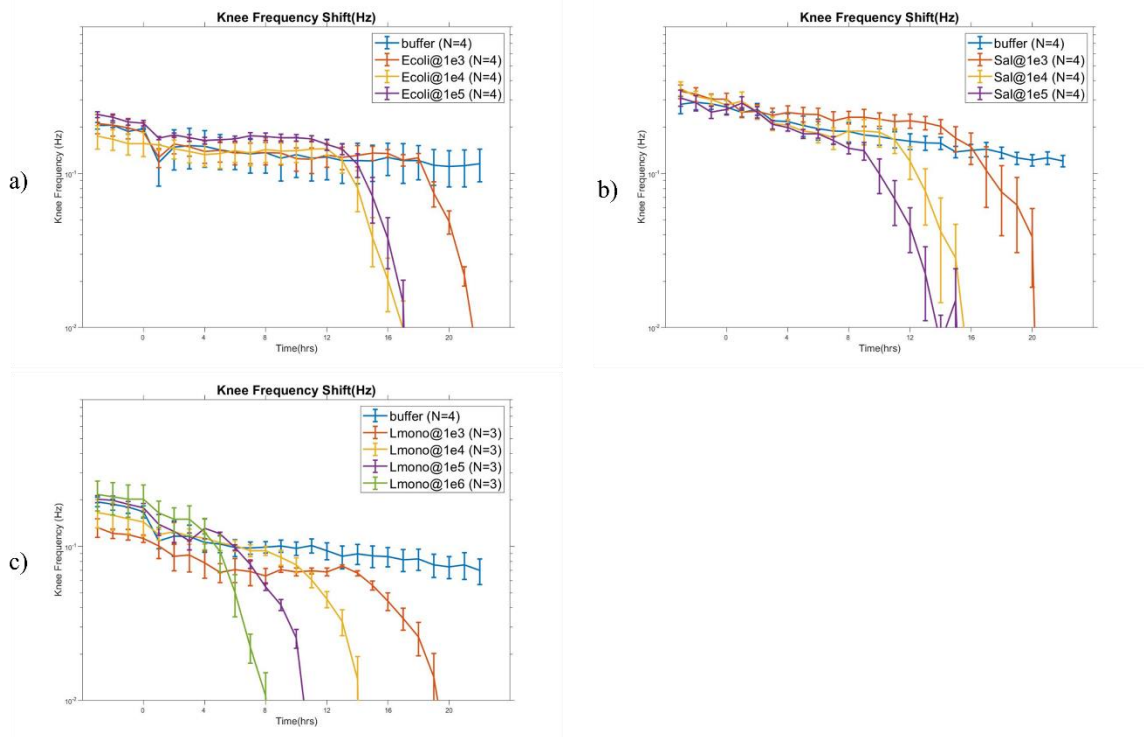


Figure 4-10 Doppler knee frequency shift among a) *E. coli* invasion, b) *S. enterica* invasion and c) *L. monocytogenes* invasion

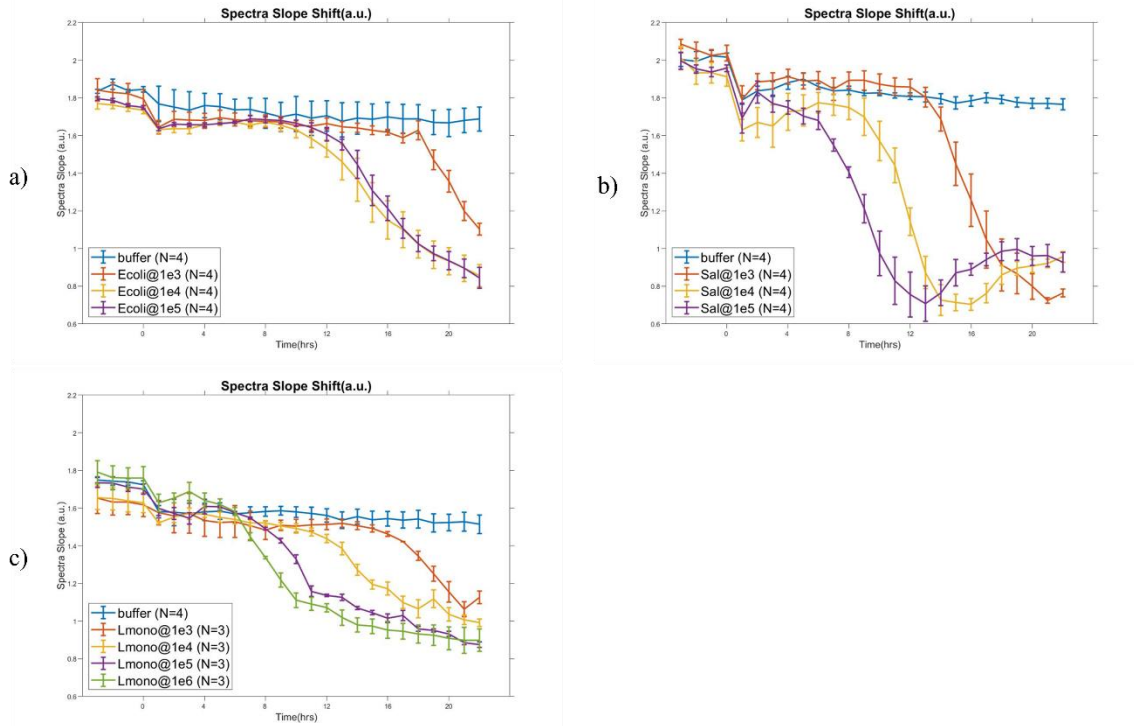


Figure 4-11 Doppler midfrequency slope parameter shift among a) *E. coli* invasion, b) *S. enterica* invasion and c) *L. monocytogenes* invasion

Figure 4-11 shows Doppler midfrequency slope parameter shift among a) *E. coli* invasion, b) *S. enterica* invasion and c) *L. monocytogenes* invasion. The typical parameter for the mid-frequency slope is around 1.5-1.7. The late mid-frequency slope drop in *E. coli* cases compared with *S. enterica* and *L. monocytogenes* cases also helps to explain that *E. coli* is competing with the living cells instead of infecting them. In addition, a two-process curve in the mid-frequency slope for *S. enterica* is detected, which again confirms that there are different dominant processes occurring in *S. enterica* invasion cases.

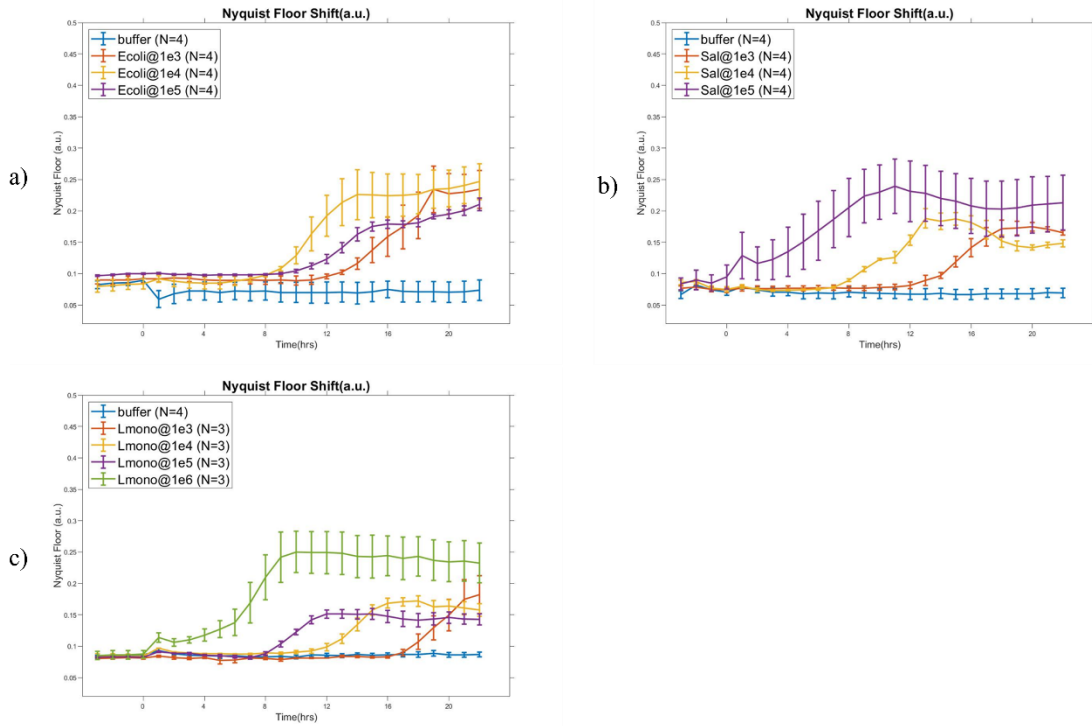


Figure 4-12 Doppler spectral Nyquist floor shift among a) *E. coli* invasion, b) *S. enterica* invasion and c) *L. monocytogenes* invasion

4.4 Discussion and Conclusion

Light scattered from living tissue displays a broad range of Doppler frequency shifts related to complex cellular processes and their associated dynamic motion. The Doppler fingerprint of living tissue is extremely sensitive to subtle changes in intracellular dynamics, and BDI provides a powerful new technique for monitoring the response of 3D living tissue to xenobiotic challenges. In this section, we described the development and improvement of BDI to monitor the infection of 3D living tissue by bacteria. Bacteria affect many of the dynamic processes within the living host, allowing the cellular response to perform the role of a living sentinel, reporting on the effects of the bacterial infection as well as monitoring the efficacy of antibiotic treatments. To illustrate the infection induced power spectral responses, tumor spheroids of the DLD-1 colon adenocarcinoma cell lines were used to highlight different characteristics caused by infection by different bacterial strains. We developed a novel BDI system to successfully capture intracellular movement in a more stable condition and with a higher resolution. We also developed a more reliable data quality control system by performing image plane control and registration of reconstructed image with raw picture in image plane. The Doppler spectral shift in pathogenic

bacterial invasions (*S. enterica* and *L. monocytogenes* invasion) is dramatically different than for non-pathogenic bacterial invasions (*E. coli* invasion) in the mid-frequency and high-frequency domain. Three biomarkers (knee frequency, mid-frequency slope and Nyquist floor) generated from Doppler power spectra also show the difference between the pathogenic bacterial invasions and non-pathogenic bacterial invasions. This work demonstrates the potential to translate BDI to the clinic to test for antibiotic-resistant infections. The future work of this project is to observe the free bacterial movement to quantify the background effects.

4.5 References

- [1] H Choi, Z Li, Z Hua, "Doppler imaging detects bacterial infection of living tissue", Communications Biology (2021).
- [2] S. Owens, "E. coli SEM image," Center for Electron Optics, MSU (1996).
- [3] S. Rabea, M. Salem-Bekhet, F. Alanazi, A. Yassin, N. Moneib, A. Elgawad, and M. Hashem, "A novel protocol for bacterial ghosts' preparation using tween 80," Saudi Pharmaceutical Journal (2017).
- [4] S. Renier, M. Hébraud, and M. Desvaux, "Molecular biology of surface colonization by *Listeria monocytogenes*: An additional facet of an opportunistic Gram-positive foodborne pathogen," Environmental microbiology 13, 835-850 (2010).
- [5] C. Unger, N. Kramer, A. Walzl, M. Scherzer, M. Hengstschlager, and H. Dolznig, "Modeling human carcinomas: physiologically relevant 3D models to improve anti-cancer drug development," Adv Drug Deliv Rev 79-80, 50-67 (2014).
- [6] B. Weigelt, C. M. Ghajar, and M. J. Bissell, "The need for complex 3D culture models to unravel novel pathways and identify accurate biomarkers in breast cancer," Adv Drug Deliv Rev 69-70, 42-51 (2014).
- [7] B. M. Baker and C. S. Chen, "Deconstructing the third dimension – how 3D culture microenvironments alter cellular cues," Journal of Cell Science 125, 3015 (2012).
- [8] K. Jeong, J. J. Turek, and D. D. Nolte, "Volumetric motility-contrast imaging of tissue response to cytoskeletal anti-cancer drugs," Opt Express 15, 14057-14064 (2007).

- [9] M. Hamon, H. Bierne, and P. Cossart, "Listeria monocytogenes: a multifaceted model," *Nat Rev Microbiol* 4, 423-434 (2006).
- [10] S. Hannemann, B. Gao, and J. E. Galán, "Salmonella modulation of host cell gene expression promotes its intracellular growth," *PLoS Pathog* 9, e1003668-e1003668 (2013).
- [11] S. P. Riley, K. C. Goh, T. M. Hermanas, M. M. Cardwell, Y. G. Chan, and J. J. Martinez, "The Rickettsia conorii autotransporter protein Sca1 promotes adherence to nonphagocytic mammalian cells," *Infect Immun* 78, 1895-1904 (2010).
- [12] Z. Li, H. Sun, J. Turek, S. Jalal, M. Childress, and D. D. Nolte, "Doppler fluctuation spectroscopy of intracellular dynamics in living tissue," *J Opt Soc Am A Opt Image Sci Vis* 36, 665-677 (2019).
- [13] D. Merrill, R. An, H. Sun, B. Yakubov, D. Matei, J. Turek, D. Nolte, "Intracellular Doppler Signatures of Platinum Sensitivity Captured by Biodynamic Profiling in Ovarian Xenografts," *Scientific Reports* (2016).
- [14] H. Kim and A.K.Bhunia, "SEL, a Selective Enrichment Broth for Simultaneous Growth of *Salmonella enterica*, *Escherichia coli* O157:H7, and *Listeria monocytogenes*", *Applied and Environmental Microbiology* (2008)

APPENDIX A. TISSUE DYNAMIC SPECTROSCOPY NORMALIZATION

Previous measurements on biological samples have not had significant BSB enhancement. However, BSB enhancements by bacterial inoculation are physical phenomena that may be caused by bacterial proliferation and increased cellular heterogeneity. Increasing BSB enhances power spectral density and different spectrogram normalizations would result in different analyses. Conventionally, spectral densities were normalized by the sum of spectral components including the DC component ($\omega = 0$). However, a sudden increase in BSB also increases the DC component and makes interpretations of spectrograms confusing. To compensate for the effect and to focus on spectral shifts, four different normalization methods are defined.

$$S_{nrm}(\omega, t) = S_{raw}(\omega, t) \quad (\text{A.1})$$

$$S_{nrm}(\omega, t) = \frac{S_{raw}(\omega, t)}{I^2} \quad (\text{A.2})$$

$$S_{nrm}(\omega, t) = \frac{S_{raw}(\omega, t)}{\int_{0.01}^{12.5} \frac{S_{raw}(\log\omega, t)}{\omega} d\omega} \quad (\text{A.3})$$

$$S_{nrm}(\omega, t) = \frac{S_{raw}(\omega, t)}{S_{raw}(\omega_{mean}, t)} \quad (\text{A.4})$$

The first normalization is simply the averaged raw baseline spectral density. The result includes the shift of optical power, and the method is not appropriate for analyzing bacterial infection. The second method is normalizing power spectral density by the intensity square. As the total sum of spectral density is the optical intensity square, this normalization method represents the relative dynamic density and excludes the optical power shift. The method assumes the spectral density beyond 12.5 Hz contributes to the Nyquist floor by the stroboscopic effect. The third method is similar to the second method, but the normalization only considers the limited bandwidth (0.01 Hz ~ 12.5 Hz) which deals with the power spectral density from the

perspective of probability. The last method is what our matlab programing uses currently. It's normalized by its own mean power density in its mean frequency ω_{mean} . The methods are called "Raw spectrum", "intensity normalization", "zero-sum normalization" and "onekey normalization", respectively. For instance, 4 different spectrograms of *S. enterica* infection (10^7 CFU/well) with different normalization methods are shown in Figure A.1.

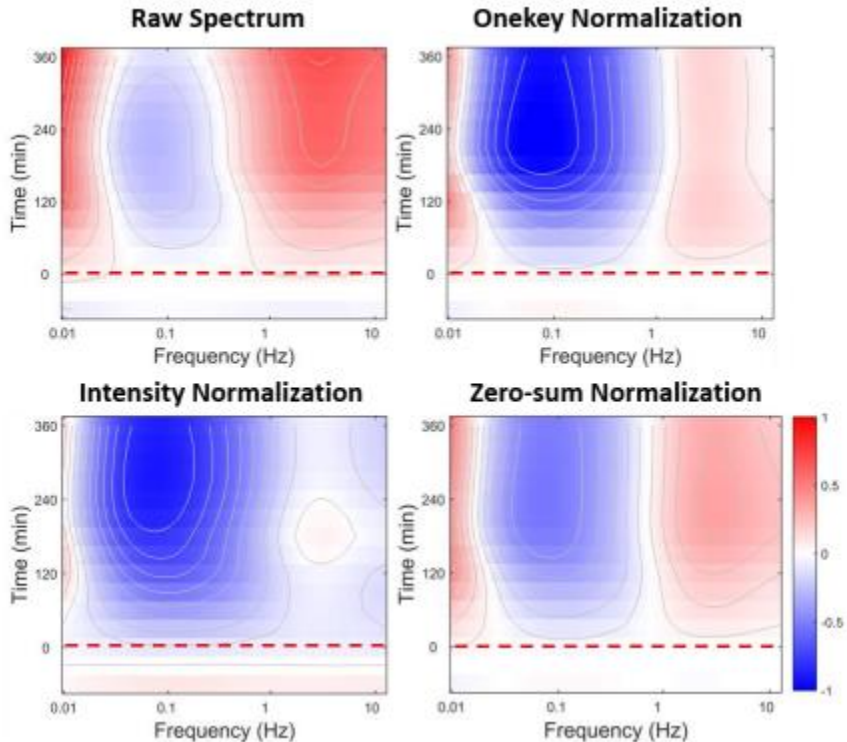


Figure A.1 Spectrograms obtained from different normalization methods. *S. enterica* infection of DLD-1 (10^7 CFU/well)

The spectrogram derived from raw spectra shows strong enhancement at the low and high-frequency region. The conventional Onekey normalization partially compensates the optical power shift effect, but the spectral enhancement still contains the BSB enhancement effect. Intensity normalization shows the temporal relative dynamic density changes after inoculation while the overall power spectral density is suppressed. Zero-sum normalization shows the probabilistic dynamic density after inoculation.

APPENDIX B. BIODYNAMIC PROFILING OF HUMAN ESOPHAGEAL CANCER HETEROGENEITY USING A DEEP TWIN AUTOENCODER

1. Analysis Programs and Methods

WBFeatdriver.m

BagAverages.m

BagWBClass.m

ESO_SiaMgenSetUp.m

PatIDFV.m

PatBagPrecon.m

SiaMTrialProperties.m

SyntheticBag.m

Welloutlier.m

bagFV.m

modelGradientsinit.m

sensitivity.m

setTrialName.m

siamaecompare.m

siamaecomparevalinit.m

siamfvcompare.m

subselectFV.m

retSiamWB.m

2. Enrollment

We opened enrollment for a pilot trial in human esophageal cancer. The eligibility criteria for enrolled patients were:

1. Patient with locally advanced esophageal cancer.
2. Patients must be candidates for chemotherapy, radiation and surgical resection.
3. Patients must sign an IRB-approved informed consent.
4. Patients must be willing to undergo a pinch biopsy at the time of endoscopic ultrasound evaluation performed for staging.

3. Enrolled Patients

Table 6 Patient Treatment[#] and Outcomes*

Patient	Treatment	Clinical Outcome
Eso1	carbo+tax	SD, no path.
Eso2	carbo+tax	PR, minimal path.
Eso9	carbo+tax	SD, no path.
Eso16	carbo+tax	SD, no path.
Eso7	carbo+tax	PR (mod)
Eso23	carbo+tax	SD, no path.
Eso24	carbo+tax	SD, no path.
Eso28	carbo+tax	SD, no path.
Eso29	cisp+5fu	SD, no path.
Eso31	carbo+tax	SD, no path.
Eso13	oxaliplatin+5fu	PR (mod)
Eso14	cisp+5fu	PR (mod)
Eso15	carbo+tax	PR, no path.
Eso20	carbo+tax	PR
Eso30	cisp+5fu	PR (marked)
Eso4	cisp+5fu	PR (marked)
Eso6	carbo+tax	PR (marked)
Eso27	cisp+5fu	PR (marked)
Eso8	cisp+5fu	CR
Eso10	carbo+tax	CR
Eso11	cisp+5fu	CR
Eso17	cisp+5fu	CR
Eso18	carbo+tax	CR
Eso21	carbo+tax	CR
Eso22	carbo+tax	CR
Eso25	carbo+tax	CR
Eso26	carbo+tax	CR

Eso19	FF	CR
-------	----	----

All patients received radiation therapy in addition to the chemotherapy.

* If no pathology, then RECIST is used.

4. Data Structure and Data Flow for Machine Learning

The clinical trial of the 28 patients with esophageal cancer produced a total of 664 interrogated wells. To analyze the correspondence between the drug-response TDS spectrograms and the patient outcomes, we established a workflow starting upstream with the 664 spectra as the input data structure and moving through to the final classification of each patient of the trial.

The first stage of the data workflow is the feature generation that converts a time-dependent spectrum and other ancillary measurements into 40 values that constitute a feature vector. Part of this process filters a drug-response spectrogram using local and global filters to generate values that all relate to the spectral changes caused by an applied treatment. To these values are added preconditions and changes in the preconditions caused by the applied treatments. The details of these feature values can be found in Ref [Section 3, 21]. At the end of the feature selection, there is a single 40-element feature vector associated with each of the 664 wells in the trial. Some of the 40 features are known to be codependent or to be unstable. Therefore, 33 selected features are retained for downstream analysis. Because there are many cofactors involved in the response of the tissue, such as percentage of stromal tissue and relative health of a sample, that may interact nonlinearly to determine the spectrogram properties, the new approach taken in this paper is to eliminate the average drug response and use all well responses, incorporating the full patient drug-response heterogeneity. This is in contrast to our previous work where all samples for a given drug were averaged [Section 3, 21]. The strength of a neural network analysis is the ability to rely on nonlinear co-dependences among the well-to-well variability to aid in the classification accuracy.

For a given patient, there are typically 32 wells measured, generating a 32-by-33 matrix that is called the Patient Wellset shown in Figure B.1. There are typically 4 replicates of each of the 7 treatments (6 drugs plus DMSO carrier) applied to the patient samples. From the Wellset data structure, we use bootstrap aggregating (known as bagging) to construct the primary data format called a Chart that is a single instance of the full trial protocol for a single patient. The

Chart consists of 7 rows that are sampled with replacement from the Wellset to generate a 7-by-33 matrix, shown in Figure B.2. Multiple Charts are generated into a batch. Typical values for the batch size is around 40 Charts out of a total of $74 = 2401$ possible permutations of 7 drugs with 4 replicates. An example of a Chart generation is shown in Figure B.2. The Wellset is sampled to construct seven 33-element feature vectors that comprise a single chart. In the example, one possible set of sampled wells is shown.

Patient WellSet Data Structure

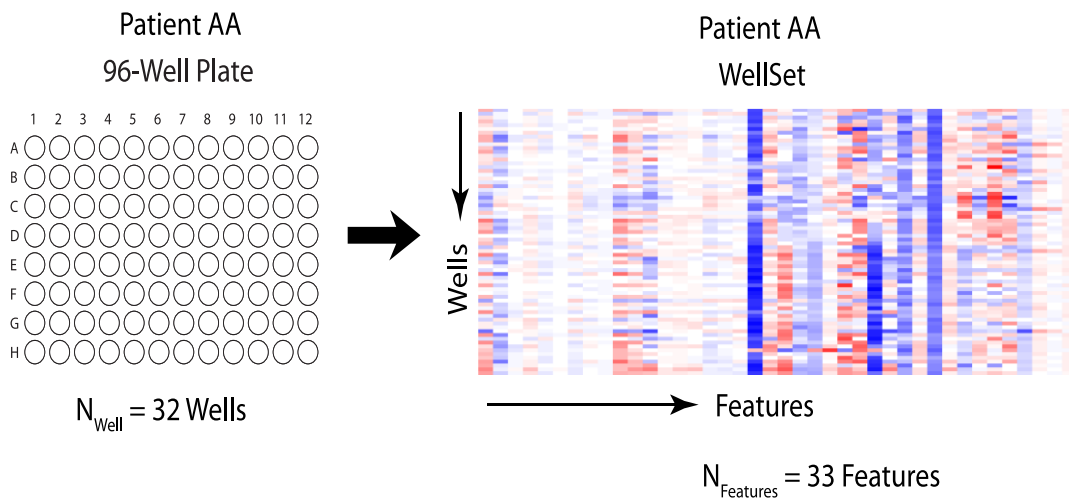


Figure B.1 Each well contains an approximately 1 mm³ biopsy sample from a patient. A single well measurement generates a 33-element feature vector. Seven treatments (drugs or DMSO) with approximately 4 replicates are measured to yield 32 feature vectors. The 32-by-33 matrix is called the Patient Wellset.

Bootstrap Aggregating (Bagging)

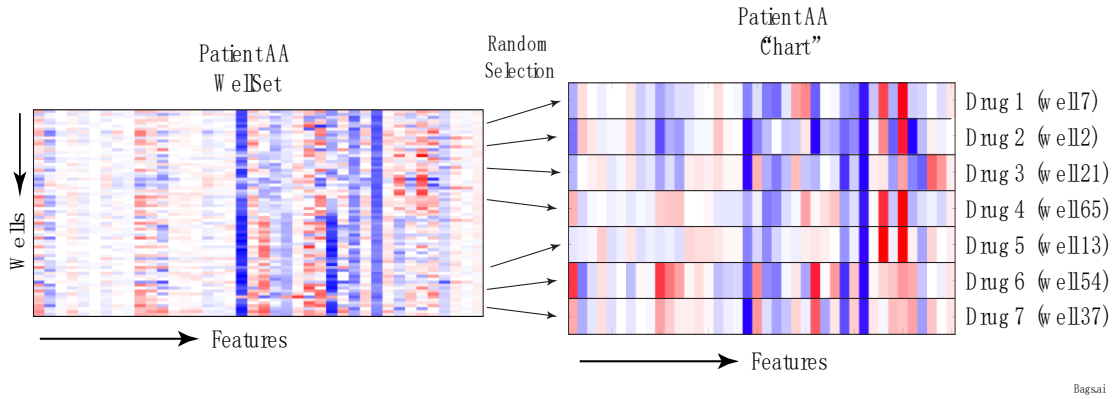


Figure B.2 Generation of a Patient Chart from the Patient Wellset. The Wellset is sampled for each of the seven treatments (drugs plus DMSO) to generate the 7x33 element Chart matrix. There are typically 40 Charts per batch used for training and testing of the neural network.

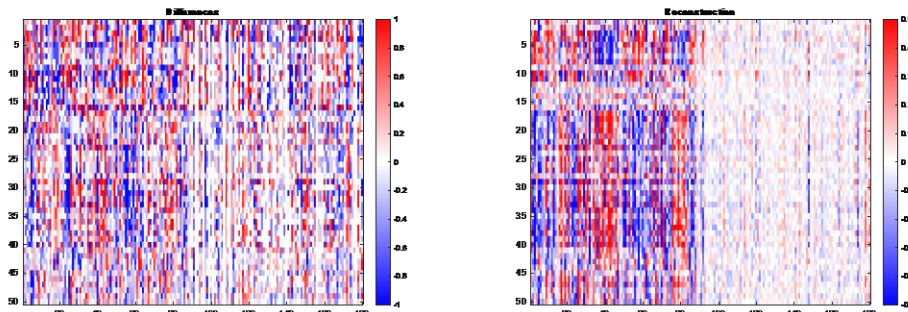


Figure B.3 Autoencoder Reconstruction: 1500 iterations

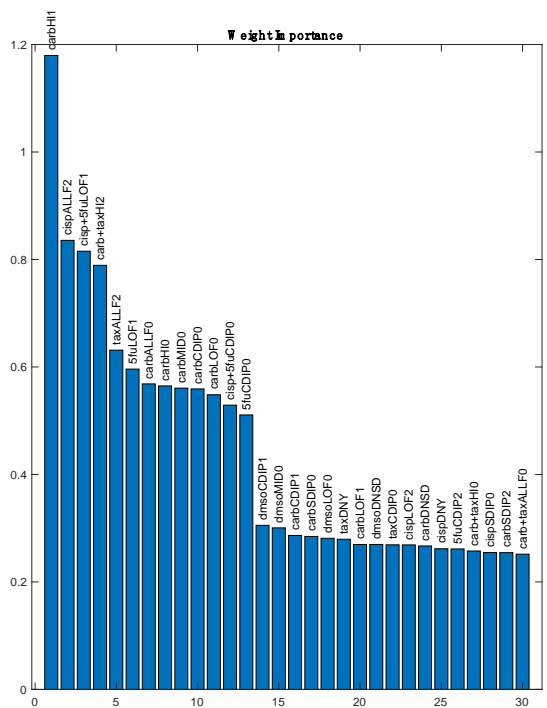


Figure B.4 Regularized Features

PUBLICATIONS

- [1] Z Hua, Z Li, J Turek, M Childress, D Nolte, *Doppler Spectroscopy of Intracellular Motion in Revived Flash-Frozen Cancer Tissues*. APS March Meeting Abstracts 2019, R64. 004 (2019)
- [2] Z Hua, J Turek, M Childress, D Nolte, *Doppler Spectroscopy of Intracellular Dynamics During Chemotherapy in Tumor Biopsies*. Bulletin of the American Physical Society 65 (2020)
- [3] H Choi, Z Li, Z Hua, J Zuponcic, E Ximenes, JJ Turek, MR Ladisch, D.Nolte, *Doppler imaging detects bacterial infection of living tissue*, Communications biology 4 (1), 1-10 (2021)
- [4] Z Hua, J Turek, D Nolte, *Phenotyping drug response of living tissue based on tissue-dynamics spectroscopy*, Proc. of SPIE Vol 11959, 1195906-1 (2022)
- [5] Z Hua, J. Turek, M, Childress, D. Nolte, *Chemosensitivity Testing of Revived Fresh-Frozen Biopsies using Digital Speckle Holography* submitted to Asian Journal of Physics (2022)